HIGH POWER ALL-FIBER LASER-AMPLIFIER SYSTEMS FOR MATERIALS PROCESSING

A DISSERTATION SUBMITTED TO

THE INSTITUTE OF MATERIALS SCIENCE AND NANOTECHNOLOGY

AND THE GRADUATE SCHOOL OF ENGINEERING AND SCIENCE

OF BILKENT UNIVERSITY

IN PARTIAL FULFILLMENT OF THE REQUIREMENTS

FOR THE DEGREE OF

DOCTOR OF PHILOSOPHY

By

Kıvanç Özgören

October, 2011

I certify that I have read this thesis and that in my opinion it is fully adequate, in scope and in quality, as a dissertation for the degree of doctor of philosophy.

Asst. Prof. Dr. F. Ömer İlday

I certify that I have read this thesis and that in my opinion it is fully adequate, in scope and in quality, as a dissertation for the degree of doctor of philosophy.

Prof. Dr. Ergin Atalar

I certify that I have read this thesis and that in my opinion it is fully adequate, in scope and in quality, as a dissertation for the degree of doctor of philosophy.

Assoc. Prof. Dr. Hilmi Volkan Demir

I certify that I have read this thesis and that in my opinion it is fully adequate, in scope and in quality, as a dissertation for the degree of doctor of philosophy.

Asst. Prof. Dr. Ali Kemal Okyay

I certify that I have read this thesis and that in my opinion it is fully adequate, in scope and in quality, as a dissertation for the degree of doctor of philosophy.

Asst. Prof. Dr. Hakan Altan

Approved for the Graduate School of Engineering and Science:

Prof. Dr. Levent Onural
Director of the Graduate School

ABSTRACT

HIGH POWER ALL-FIBER LASER-AMPLIFIER SYSTEMS FOR MATERIALS PROCESSING

Kıvanç Özgören
PhD in Materials Science and Nanotechnology
Supervisor: Asst. Prof. Dr. F. Ömer Ilday
October, 2011

When the fiber lasers first appeared in 1970s, their average powers and pulse energies were so low that they remained as a laboratory curiosity for a long time. The scientific interest in fiber lasers continued due to their inherited practical advantages over the established solid state lasers. First of all, in single-mode operation, fiber lasers deliver diffraction-limited beam quality since light is always guided in the fiber by total internal reflection. Beam qualities of other type of lasers deteriorate with increasing power due to thermal effects like thermal lensing. Second, their structures are well suited to power-scaling due to their enormous surface area to volume ratio. In theory, output power level of a fiber laser should be able to go up to the 1-10 kW range without serious thermal problems. Third, the small signal gain and optical efficiency are very high compared to other types of lasers because of the intense interaction with the active ions over long lengths. Efficiency of an ytterbium fiber laser can reach 80%, depending on the design parameters. Therefore, single-pass amplification is practical, whereas most other gain media do not have enough gain for single-pass amplification. Consequently, the vast majority of high-power fiber lasers are based on master-oscillator power-amplifier (MOPA) structure, where the signal is first created in an oscillator and then amplified in an (single or multi stage) amplifier. Fourth,

beam propagation through all the optical elements comprising a fiber laser can be guided propagation and, in theory, this enables misalignment-free operation. Fiber lasers are increasingly used outside the basic laser research laboratory in material (particularly metal) processing, medical, metrology, defense applications, as well as scientific research. For many of these applications, flexibility and misalignment-free operation is important. However, there are still many systems in use, including many reported in the academic literature, where the pump light is coupled into the fiber through free space optics, and components such as isolators, grating stretchers are frequently employed in bulk optics form.

In this thesis, we mainly focus on all-fiber designs, with the specific aim of developing high-power, robust, fiber-integrated systems delivering high technical performance without compromising on the practical aspects. The laser systems developed in this thesis are also applied to material processing. This allows us to gain first-hand experience in the actual utility of the lasers that we develop in real-world applications, generate valuable feedback for our laser development efforts and produce laser systems, which are ready for industrial implementation.

The thesis begins with introductory chapters on the basic physics and technology of high-power fiber lasers, including a brief discussion of the material processing applications. In Chapter 1, we focus on optical fiber itself, where the manufacturing and structure are explained briefly, followed by some theoretical information on guidance of light, dispersion and nonlinear effects in fibers. In Chapter 2, we focus on the theory of fiber lasers. Firstly, propagation of ultrashort pulses in fibers is explained and nonlinear Schrödinger equation (NLSE) is introduced. Then gain in rare-earth doped fibers, mode-

locking mechanism, and different mode-locking regimes are described. Following a survey on current situation of fiber lasers in world market, we introduce the current fiber architectures, discuss the main limitations encountered in high power fiber laser design, nonlinear effects, fiber damage and excessive thermal loads. Then, the possible application areas of these lasers in materials processing are described. Chapter 3 reports on the development of a high-power and high-energy all-fiber-integrated amplifier. In Chapter 4, we introduce a new and low-cost technique that allows the construction of all-fiber-integrated lasers operating in the all-normal dispersion regime. In Chapter 5, an all-fiber-integrated laser system delivering 1-ns-long pulses with an average power of 83 W at a repetition rate of 3 MHz is introduced that combines the positive aspects of micromachining with ultrashort pulses in terms of precision and long nanosecond pulses in terms of ablation speed. In Chapter 6, we report on the development of an all-fiber continuous-wave fiber laser producing more than 110 W of average power. Chapter 7 is on the use of these laser systems in systematic material processing experiments, where we compare the influence of three different laser systems, producing approximately 100 ps, 1 ns and 100 ns pulses. The final chapter provides the concluding remarks.

Keywords: Fiber laser, oscillator, amplifier, all-fiber structure, high power lasers, materials processing.

ÖZET

MALZEME İŞLEMEYE YÖNELİK YÜKSEK GÜÇLÜ BÜTÜNLEŞİK FİBER LAZER YÜKSELTEÇ SİSTEMLERİ

Kıvanç Özgören
Malzeme Bilimi ve Nanoteknoloji, Doktora
Tez Yöneticisi: Yrd. Doç. Dr. F. Ömer İlday
Ekim, 2011

1970'li yıllarda ortaya çıktıklarında, ortalama güçleri ve atım enerjileri oldukça düşük olan fiber lazerler uzunca bir süre boyunca laboratuvarlarla sınırlı kaldı. Bu süre boyunca fiber lazerlere gösterilen sürekli bilimsel ilginin kaynağı katı-hal lazerleri gibi rakiplerine göre sahip oldukları yapısal avantajlardır. Birinci olarak, özellikle tek-modlu fiber lazerlerin ışın kalitesi, ışığın devamlı olarak fiber içinde kılavuzlanarak ilerlemesi sayesinde oldukça iyidir. Diğer çeşit lazerlerin ışın kalitesinde yüksek güçlerde ortaya çıkan ısısal merceklenme tarzı etkiler nedeniyle düşüş yaşanmaktadır. İkinci olarak, fiberlerin yapısı çok yüksek alan/hacim oranları sayesinde yüksek güçlere ulaşılmaya uygundur. Teorik olarak fiber lazerlerin her hangi bir ısısal problemle karşılaşılmadan 1-10 kW civarı güç seviyesine ulaşabilmesi olasıdır. Üçüncü olarak, fiber lazerlerin sinyal kazancı ve optik verimi, aktif iyonlarla olan uzun mesafeli yoğun etkileşim sayesinde diğer lazer çeşitlerine göre oldukça yüksektir. Tasarım parametrelerine bağlı olarak ytterbiyum katkılı fiber lazerlerin verimi %80'e varmaktadır. Bu aynı zamanda tek geçişli yükselteç sistemlerine olanak verir ki, bu diğer tip lazerlerdeki düşük kazanç seviyesi nedeniyle çok zordur. Dolayısıyla, günümüzde çoğu yüksek güçlü fiber lazer ana-salıngaç güç-yükselteci (MOPA) yapısını kullanmaktadır. Burada sinyal öncelikle ana salıngaçta yaratılmakta

ardından (bir veya daha çok aşamalı) yükselteçte güçlendirilmektedir. Dördüncü olarak, fiber lazerler, ışığın devamlı kılavuzlanarak ilerlemesine olanak verdiğinden, neredeyse hiç ince ayar gerektirmemektedir. Fiber lazerler giderek artan miktarlarda laboratuvar dışında, malzeme işleme, tıp, metroloji, savunma gibi alanlarda kullanılmaya başlanmıştır. Bu alanların pek çoğu için esneklik ve ince ayar gerektirmezlik önem taşımaktadır. Ancak, özellikle akademik literatüre bakıldığında, hala pompa ışığının fiberin içine fiber dışı optik yöntemlerle sokulmakta olduğu, fiber dışı yalıtıcıların ve kırınım ağlarının kullanıldığı sistemler görülmektedir.

Bu tezde, genel olarak yüksek güçlü, dış etkenlere dayanıklı, tamamen fiberde bütünleşik lazer sistemleri üzerinde durulmaktadır. Geliştirilen lazerler malzeme işlemekte de kullanılmıştır. Bu bize birinci elden lazerlerimizin gerçek uygulamalardaki başarısını göstermekte ve lazer geliştirme çalışmalarımıza önemli bir geridönüş sağlamaktadır.

Tezin giriş bölümlerinde yüksek güçlü fiber lazerlerin fizik ve teknolojisi anlatılmakta ve kısaca malzeme işleme uygulamalarından bahsedilmektedir. 1. Bölüm'de optik fiberlere odaklanılmakta, yapıları ve üretim teknikleri hakkında kısa bir bilgi verilmektedir. Daha sonra fiber içindeki ışığın kılavuzlanması, saçılım ve doğrusal olmayan etkiler anlatılmaktadır. 2. Bölüm'de fiber lazer sistemlerine odaklanılmaktadır. Ultra kısa atımların fiber içinde ilerlemesinin teorisi ve doğrusal olmayan Schrödinger denklemi (NLSE) ortaya konduktan sonra, seyrek toprak elementi katkılı fiberlerdeki kazanç, kip-kilitleme, ve değişik kip-kilitli fiber lazer tipleri anlatılmaktadır. Fiber lazerlerin dünya pazarındaki yerinin ve güncel fiber yapılarının tanıtılmasının ardından, doğrusal olmayan etkiler, fiberde ortaya çıkabilecek hasar çeşitleri, ısısal yükler gibi yüksek güçlü fiber lazerleri sınırlayan faktörler anlatılmaktadır. Daha sonra bu lazerlerin malzeme işlemeye yönelik

olası uygulama alanlarından bahsedilmektedir. 3. Bölüm'de yüksek güç ve enerjili, fiberde bütünleşik bir yükselteç sisteminin geliştirilmesi anlatılmaktadır. 4. Bölüm'de normal-saçılımlı lazer salıngaçları üretmek için yeni ve ucuz bir teknik anlatılmaktadır. 5. Bölüm'de 83 W gücünde, 3 MHz tekrar frekansında çalışan, 1 ns uzunluğunda atımlar üreten, tamamen fiberde bütünleşik, ultra kısa atımların hassasiyetiyle uzun atımların malzeme işleme hızını birleştiren bir sistem tanıtılmaktadır. 6. Bölüm'de 110 W üzerinde güç üreten sürekli-modda çalışan bir fiber lazer sisteminden bahsedilmektedir. 7. bölümde bu lazerlerin malzeme işleme deneylerinde kullanıldığı ve 100 ps, 1 ns ve 100 ns uzunluğundaki atımların karşılaştırıldığı bir çalışma yer almaktadır. Son bölüm ise sonuçlardan oluşmaktadır.

Anahtar kelimeler: Fiber lazer, salıngaç, yükselteç, bütünleşik fiber yapı, yüksek güçlü lazerler, malzeme işleme.

Acknowledgement

In the first place, I would like to thank my advisor F. Ömer İlday for his invaluable support and guidance during my study. I am impressed by the great job that he has done in building our laboratory from the grounds.

I am indebted to Bülent Öktem, Hamit Kalaycıoğlu, Pranab Mukhopathyay and Sinem Yılmaz for their close collaboration at various stages of my thesis.

Technical discussions with Levent Budunoğlu and Coşkun Ülgüdür were very fruitful.

I am grateful to Alper Bayrı, Seydi Yavaş, Mutlu Erdoğan, Çağrı Şenel, Kutan Gürel, Ebru Düldergil, Emrah İlbey, Önder Akçaalan, Punya Paltani, Parviz Elahi, Ihor Pavlov and the rest of the members of Ultrafast Optics & Lasers Group for their support and friendship.

Koray Eken, Ece Pasin and Mesut Tasalı from FiberLAST made important contributions especially on the development of the industrial aspects of our lasers.

I would like to thank my committee members Asst. Prof. Dr. F. Ömer İlday, Prof. Dr. Ergin Atalar, Assoc. Prof. Dr. Hilmi Volkan Demir, Asst. Prof. Dr. Ali Kemal Okyay and Asst. Prof. Dr. Hakan Altan for their constructive suggestions while reviewing my thesis.

This work was supported by TÜBİTAK under grants 106G089, and 209T058, SAN-TEZ under grant 00255.STZ.2008-1, EU Marie Curie IRG FiberLaser, FP7 Bilkent University Research Funds, and by the Distinguished Young Scientist Award of the TÜBA.

Table of Contents

List of Figures

Chapter 1

Introduction to Optical Fibers

1.1. Brief History of Optical Fiber Technology

The first optical fibers based on total internal reflection principle were fabricated as early as 1920s [1-3]. However, these were unclad glass fibers and ineffective in guiding light. This is mainly because of the sensitivity of the glass-air interface to environmental effects such as scattering by dust particles, etc. The field of fiber optics was really born after two major improvements: First is the development of the cladded fibers in 1950s [4-7], which vastly improved the guidance of light in the core of the fiber by surrounding it with also a silica cladding, so that their interface is immune to environmental effects. Second is the production of low loss silica fibers with high level of purity in 1979 [8], where Rayleigh scattering imposes a fundamental lower limit to loss. Fig. 1.1.1 shows the variation of loss of silica with respect to wavelength [9]. The minimum loss (0.2 dB/km) is reached at a wavelength of ~1.55 μm, which is the main reason why the modern telecommunication is based on this wavelength.

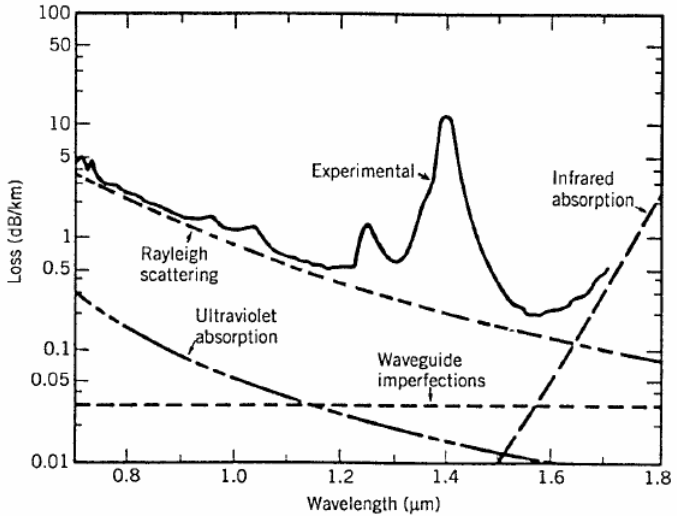

Fig 1.1.1. Variation of optical loss of highly pure silica with respect to wavelength [9].

While these improvements revolutionized the telecommunication industry, the nonlinear phenomena began to show itself as the intense light was forced to travel in the small core region of the fibers for long distances. Hence, in the 1970s, Raman and Brillouin scattering were investigated [10-12], followed by optically induced birefringence, parametric four-wave mixing and self-phase modulation [13-17]. Soliton-like pulses supported by optical fibers as a result of interplay between the nonlinearity and dispersion were first suggested in 1973 [18] and observed experimentally in 1980 [19]. Availability of rare-earth doped (especially Erbium doped) fibers triggered the invention of the first fiber laser oscillators. Soliton-like mode-locked fiber lasers [20, 21] were followed by several other mode-locking regimes; stretched-pulse (dispersion-managed soliton) [22], similariton [23, 24], all-normal-dispersion (dissipative soliton) [25] and most recently soliton-similariton [26].

On the other hand, fiber laser amplifiers mainly based on master-oscillator-power-amplifier design started to emerge after 1980s. The main factor holding back the high power amplifiers was the limited brightness of solid state diodes, which made it hard to couple more than ~1 W of pump power into the core of a fiber to amplify the signal. Solving this

problem by using the double clad design [27] where the pump propagates through the cladding led high power pump coupling into the fiber. Today fiber lasers can go up to 10 kW and their power level increases by a factor of ~1.7 each year [28]. Robustness, beam quality and efficiency are the main reasons why fiber lasers are replacing other types of lasers in many areas of industry.

1.2. Geometry and Manufacturing

Although there are lots of other fiber designs, the simplest one is seen in Fig. 1.2.1, which is called as the step-index fiber and composed of a fused silica glass core with an refractive index of n_1 surrounded by also a glass cladding with a slightly lower index of n_2.

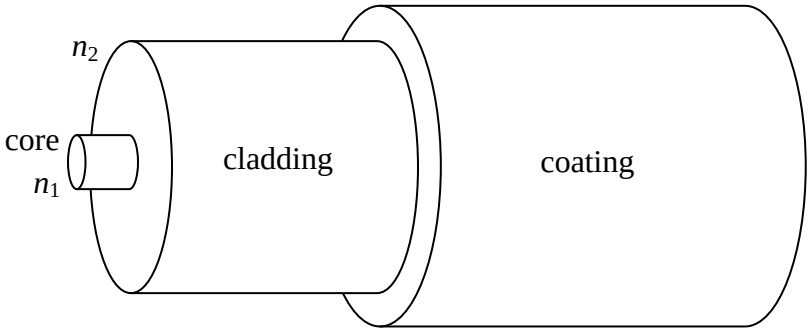

Fig.1.2.1. Schematic of a step-index fiber that is the simplest form of an optical fiber.

Light is guided in the core by total internal reflection at the core/cladding interface. Two basic parameters of this structure are the index difference, which determines the numerical aperture (NA) of the fiber as

$$NA = (n_1^2 - n_2^2)^{1/2}, \tag{1.2.1}$$

and the core radius a, which determines the normalized frequency (V-parameter) of the fiber together with the numerical aperture and the wavenumber $k_0 = \omega/c = 2\pi/\lambda$ as

$$V = k_0 a NA. \tag{1.2.2}$$

V-parameter is particularly important since it is related with the number of modes that an optical fiber can support. For single-mode operation, it should be less than 2.405. For a typical single-mode fiber, $NA = 0.14$, $a = 2$ μm, and $V = 1.76$ at 1 μm wavelength. The cladding radius b is not so important as long as the evanescent field of the light stays within the cladding. The most common value for cladding radius is 62.5 μm.

The fabrication of such a thin fiber, not an easy task at all, is a two-stage process as shown in Fig. 1.2.2. First stage is to prepare a preform, which is ~1 m long with a radius of ~1 cm. There are several methods to produce a preform [29], which are generally based on vapor deposition technique with slight differences.

Modified chemical vapor deposition (MCVD) is the most common technique for preform manufacturing. As shown in Fig. 1.2.2, gaseous form of silicon tetrachloride ($SiCl_4$) is mixed with oxygen and passed through a rotating silica glass tube, which is heated up to 1600 °C with a burner that continuously moves back and forth. Here, Si reacts with oxygen and form fine soot of silica, which coats the inner surface of the glass tube near the burner and is sintered into a clear glass layer. Other dopants can be included to the process for changing the index (Ge, P, B, F) or creating an active lasing medium (Rare-earths like Yb, Er, etc.). Finally, the tube is collapsed by heating it up to 2000 °C.

Outside vapor deposition (OVD) is a process where the silica soot is deposited on the surface of some target rod (e.g. a glass mandrel), rather than inside of a tube as with MCVD.

Vapor phase axial deposition (VAD) is similar to OVD, but uses a modified geometry, where the deposition occurs at the end of the target rod so long performs can be made.

Plasma chemical vapor deposition (PCVD) uses deposition inside a tube, similar to MCVD. However, instead of a burner, microwaves are used for heating the deposition region. The deposition is slow, but very precise.

There are alternative ways to dope silica such as direct nanoparticle deposition (DND) technology developed by Liekki [30] where nanometer sized dopant particles are directly deposited into the preform. This allows high rare-earth doping concentrations with low level of photodarkening, which is one of the main concerns in high power laser design.

Second stage of fiber production is the drawing of fiber from the preform. A fiber-drawing tower (Fig. 1.2.2) is typically several meters high. One end of the preform is heated close to the melting point by a furnace so that a thin fiber can be pulled out. During this process, pulling speed is adjusted such that the fiber diameter is kept constant by monitoring its value by a micrometer. The relative core-cladding dimensions are preserved in this process. It is also customary to coat the fiber before winding it up. Typical coating materials are acrylate, silicone and polyimide.

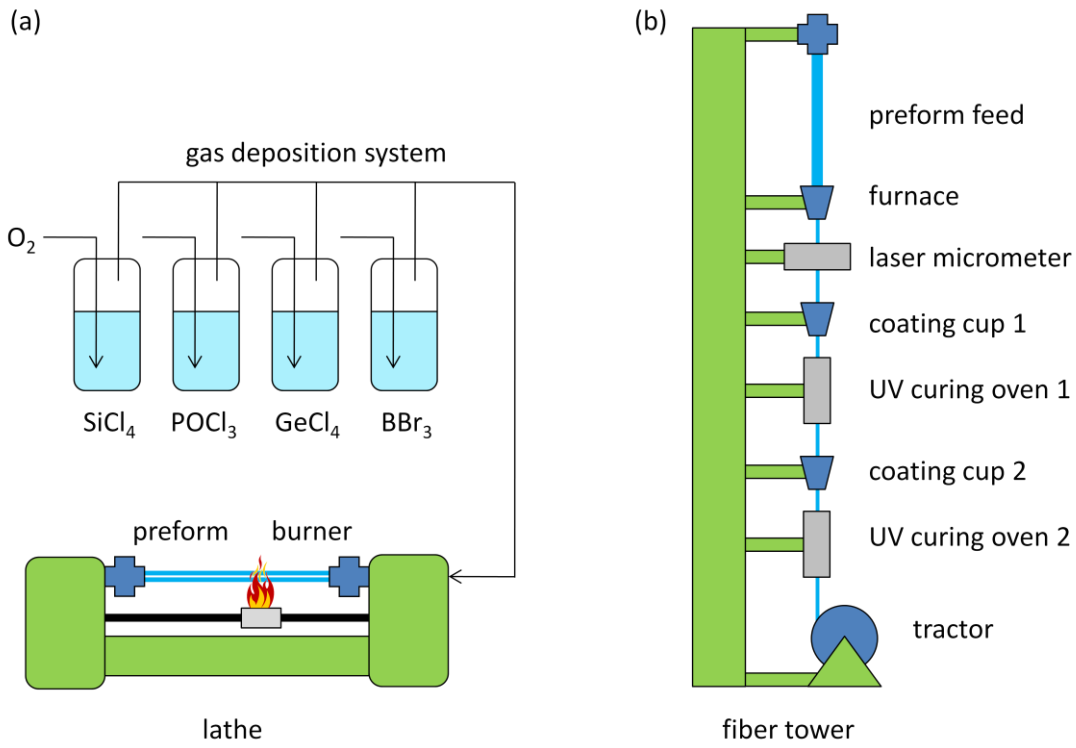

Fig.1.2.2. (a) Preform manufacturing and (b) fiber drawing processes.

1.3. Guidance of Light

In order to understand how the light is guided in an optical fiber, let's start with the Maxwell's equations in their most general form:

$$\nabla . \boldsymbol{D} = \rho, \tag{1.3.1}$$

$$\nabla . \boldsymbol{B} = 0, \tag{1.3.2}$$

$$\nabla \times \boldsymbol{E} = -\frac{\partial \boldsymbol{B}}{\partial t}, \tag{1.3.3}$$

$$\nabla \times \boldsymbol{H} = \boldsymbol{J} + \frac{\partial \boldsymbol{D}}{\partial t}, \tag{1.3.4}$$

where $\boldsymbol{B}$ and $\boldsymbol{D}$ are magnetic and electric flux densities, $\boldsymbol{H}$ and $\boldsymbol{E}$ are the corresponding magnetic and electric field vectors, ρ and $\boldsymbol{J}$ are the charge and current densities. These are related to each other by

$$\boldsymbol{D} = \varepsilon_0 \boldsymbol{E} + \boldsymbol{P}, \tag{1.3.5}$$

$$\boldsymbol{B} = \mu_0 \boldsymbol{H} + \mu_0 \boldsymbol{M}, \tag{1.3.6}$$

where $\boldsymbol{P}$ and $\boldsymbol{M}$ are induced electric and magnetic polarizations, ε_0 is the vacuum permittivity, μ_0 is the vacuum permeability such that $\mu_0 \varepsilon_0 = 1/c^2$. Free charge density ρ and current density $\boldsymbol{J}$ is zero in a silica fiber. Also $\boldsymbol{M} = 0$ in a nonmagnetic medium and $\nabla . \boldsymbol{E} = 0$ in a homogenous medium. After these simplifications we have the wave equation

$$\nabla^2 \boldsymbol{E}(\boldsymbol{r}, t) - \frac{1}{c^2} \frac{\partial^2 \boldsymbol{E}(\boldsymbol{r}, t)}{\partial t^2} = \mu_0 \frac{\partial^2 \boldsymbol{P}(\boldsymbol{r}, t)}{\partial t^2}. \tag{1.3.7}$$

Since the fiber has a cylindrical structure, it is natural to express the electric field in cylindrical coordinates

$$\boldsymbol{E}(\boldsymbol{r}, t) = E_\rho(\boldsymbol{r}, t)\boldsymbol{\rho} + E_\phi(\boldsymbol{r}, t)\boldsymbol{\phi} + E_z(\boldsymbol{r}, t)\boldsymbol{z}. \tag{1.3.8}$$

However, for cylindrical coordinates E_ρ and E_ϕ are coupled to each other so it is easier to solve Eq. 1.3.7 for E_z and similarly for H_z, then find E_ρ, E_ϕ, H_ρ, H_ϕ by using Maxwell relations. For simplicity, we will denote $E_z(\boldsymbol{r}, t)$ with $E(\boldsymbol{r}, t)$ in the following calculations.

The nonlinear part of the polarization is small and ignored for now. Later, we will add this part as a small perturbation, which will cause a slight modification on the solution. Hence, using a linear form of polarization as $\boldsymbol{P}_L(\boldsymbol{r},t) = \varepsilon_0\chi^{(1)}\boldsymbol{E}(\boldsymbol{r},t)$ where $\chi^{(1)}$ is the first order susceptibility and taking Fourier transformation of Eq. 1.3.7, we have

$$\nabla^2 E(\boldsymbol{r},\omega) + \varepsilon_r(\omega)\frac{\omega^2}{c^2}E(\boldsymbol{r},\omega) = 0, \tag{1.3.9}$$

where $\varepsilon_r(\omega) = 1 + \chi^{(1)}(\omega)$ is the relative permittivity, which is also called the dielectric constant. (There is an ambiguity here; sometimes $\varepsilon_r(0)$ is called the dielectric constant.) It is related to refractive index $n(\omega)$ and absorption coefficient $\alpha(\omega)$ by the following definition

$$\varepsilon_r(\omega) = \left(n(\omega) + \frac{ic}{2\omega}\alpha(\omega)\right)^2. \tag{1.3.10}$$

Assuming the losses are small in a fiber, $\varepsilon_r(\omega) \cong n^2(\omega)$ and we may write the wave equation as

$$\nabla^2 E(\boldsymbol{r},\omega) + k^2(\omega)E(\boldsymbol{r},\omega) = 0, \tag{1.3.11}$$

where $k(\omega) = n(\omega)k_0 = n(\omega)\,\omega/c$. In its explicit form

$$\frac{\partial^2 E(\boldsymbol{r},\omega)}{\partial\rho^2} + \frac{1}{\rho^2}\frac{\partial^2 E(\boldsymbol{r},\omega)}{\partial\phi^2} + \frac{\partial^2 E(\boldsymbol{r},\omega)}{\partial z^2} + \frac{1}{\rho}\frac{\partial E(\boldsymbol{r},\omega)}{\partial\rho} + k^2(\omega)E(\boldsymbol{r},\omega) = 0. \tag{1.3.12}$$

This equation can be solved with separation of variables method by substituting the following assumed solution into it

$$E(\boldsymbol{r},\omega) = A(\omega)F(\rho)\exp(im\phi)\exp(i\beta z), \tag{1.3.13}$$

where m is an integer since ϕ is a cyclic coordinate, β is the propagation constant, and $A(\omega)$ is a normalization constant. Then we have

$$\frac{\partial^2 F(\rho)}{\partial \rho^2} + \frac{1}{\rho}\frac{\partial F(\rho)}{\partial \rho} + \left(n^2 k_0^2 - \beta^2 - \frac{m^2}{\rho^2}\right)F(\rho) = 0. \tag{1.3.14}$$

Here $n = n_1$ for $\rho \leq a$ and $n = n_2$ for $\rho \geq a$, which are the core and cladding indexes respectively. The solution of this equation is given as

$$F(\rho) = J_m(\kappa\rho) \qquad \rho \leq a \tag{1.3.15}$$

$$F(\rho) = K_m(\gamma\rho) \qquad \rho \geq a, \tag{1.3.16}$$

where J_m is the Bessel and K_m is the modified Bessel function with $\kappa = (n_1^2 k_0^2 - \beta^2)^{1/2}$ and $\gamma = (\beta^2 - n_2^2 k_0^2)^{1/2}$. This defines the transverse modal distribution. Note that, the shape of the fundamental mode is very similar to a Gaussian so in practice it is generally approximated by a Gaussian function in the form of

$$F(\rho) = A\exp[-\rho^2/w^2]. \tag{1.3.17}$$

In order to determine the propagation constant β, the above procedure is also applied for obtaining H_z. Then Maxwell equations are used to find E_ρ, E_ϕ, H_ρ, H_ϕ. After applying the boundary conditions, β can be calculated from the eigenvalue equation obtained as [31]

$$\left[\frac{J_m{}'(\kappa a)}{\kappa J_m(\kappa a)} + \frac{K_m{}'(\gamma a)}{\gamma K_m(\gamma a)}\right]\left[\frac{J_m{}'(\kappa a)}{\kappa J_m(\kappa a)} + \frac{n_2^2}{n_1^2}\frac{K_m{}'(\gamma a)}{\gamma K_m(\gamma a)}\right] = \left[\frac{m\beta k_0(n_1^2 - n_2^2)}{a n_1 \kappa^2 \gamma^2}\right]^2, \tag{1.3.18}$$

where $J_m'(\kappa a) = \mathrm{d}J_m(\kappa a)/\mathrm{d}(\kappa a)$ and $K_m'(\gamma a) = \mathrm{d}K_m(\gamma a)/\mathrm{d}(\gamma a)$.

Note that, always $n_1 k_0 > \beta > n_2 k_0$ for a guided mode. So we can define the effective index $n_{eff} = \beta c/\omega$ of a fiber such that $n_1 > n_{eff} > n_2$. This definition will be useful in the following discussions.

1.4. Dispersion

Dispersion can be defined as the propagation of different frequency components with different velocities. Mainly there are three types of dispersion; material, waveguide and modal dispersions. The most dominant one is the material dispersion (or chromatic dispersion), which arises from the dependency of refractive index $n(\omega)$ on frequency. This is related to the characteristic resonant absorption frequencies of the medium. The Sellmeier equation gives a very successful approximation of the refractive index for frequencies far from these resonances;

$$n^2(\omega) = 1 + \sum_{j=1}^{m} \frac{B_j \omega_j^2}{\omega_j^2 - \omega^2}, \tag{1.4.1}$$

where ω_j is the resonance frequency and B_j is its strength. The resonant wavelengths of silica are given as 0.0684 μm, 0.116 μm, 9.896 μm with strengths of 0.696, 0.408, 0.897, respectively [31]. Naturally, there are no resonances in the wavelength range where the silica fibers are commonly used (0.3−2.0 μm).

Waveguide dispersion occurs since the different frequency components in a waveguide have different propagation constants along the propagation direction. Modal dispersion is

also similar; different modes in a waveguide have different propagation constants. In general the effect of modal dispersion is larger than the waveguide dispersion. However, it does not exist for a single-mode fiber.

Although dispersion is important in fiber optics in general, it is particularly important for short pulse propagation, as it is very effective in broadening the pulse. After defining the dispersion causes for the propagation constant $\beta(\omega)$, we can now write its Taylor expansion about ω_0 where the pulse spectrum is centered:

$$\beta(\omega) = n(\omega)\frac{\omega}{c} = \beta_0 + \beta_1(\omega - \omega_0) + \frac{1}{2!}\beta_2(\omega - \omega_0)^2 + \cdots \tag{1.4.2}$$

where $n(\omega) = n_{eff}(\omega)$ is the effective index of the fiber and $\beta_m = \mathrm{d}^m\beta(\omega)/\mathrm{d}\,\omega^m$ evaluated at $\omega = \omega_0$. We can write few terms of this expansion, which are of physical significance:

$$\beta_0 = \frac{1}{c}n(\omega_0)\omega_0 \tag{1.4.3}$$

$$\beta_1 = \frac{1}{c}\left(n(\omega) + \omega\frac{\mathrm{d}n(\omega)}{\mathrm{d}\omega}\right)_{\omega_0} = \frac{n_g}{c} = \frac{1}{v_g} \tag{1.4.4}$$

$$\beta_2 = \frac{1}{c}\left(2\frac{\mathrm{d}n(\omega)}{\mathrm{d}\omega} + \omega\frac{\mathrm{d}^2n(\omega)}{\mathrm{d}\omega^2}\right)_{\omega_0}, \tag{1.4.5}$$

where n_g is the group index and v_g is the group velocity. Physically, the envelope of a pulse propagates with the group velocity β_1^{-1} while β_2 represents the dispersion of group velocity responsible for broadening of the pulse. So β_2 is known as the group velocity

dispersion (GVD) parameter. Sometimes the dispersion parameter D is used in place of β_2, which are related with each other by the following equation

$$D = \frac{\mathrm{d}\beta_1}{\mathrm{d}\lambda} = -\frac{2\pi c}{\lambda^2}\beta_2 \cong \frac{\lambda}{c}\frac{\mathrm{d}^2 n(\lambda)}{\mathrm{d}\lambda^2}, \tag{1.4.6}$$

where $\lambda = 2\pi c/\omega$ is the wavelength corresponding to the frequency ω.

1.5. Nonlinear Effects

It is important to realize that the optical response of a material changes in the presence of intense light. The polarization plays a key role here. Previously, we considered only the linear polarization term $P_L(\boldsymbol{r},t) = \varepsilon_0\chi^{(1)}E(\boldsymbol{r},t)$ and in that case we were able to embed this term inside the second term of the following wave equation

$$\nabla^2 E(\boldsymbol{r},t) - \varepsilon_r\frac{1}{c^2}\frac{\partial^2 E(\boldsymbol{r},t)}{\partial t^2} = 0 \tag{1.5.1}$$

by using $\varepsilon_r = 1 + \chi^{(1)}$. Now we will consider nonlinear polarization terms, which are originated from the inharmonic motion of charged particles. Substituting

$$P_{NL}(\boldsymbol{r},t) = \varepsilon_0\left(\chi^{(2)}E^2(\boldsymbol{r},t) + \chi^{(3)}E^3(\boldsymbol{r},t) + \cdots\right) \tag{1.5.2}$$

into the wave equation results in

$$\nabla^2 E(\boldsymbol{r},t) + \varepsilon_r\frac{1}{c^2}\frac{\partial^2 E(\boldsymbol{r},t)}{\partial t^2} = \mu_0\frac{\partial^2 P_{NL}(\boldsymbol{r},t)}{\partial t^2}. \tag{1.5.3}$$

Here, the second-order susceptibility $\chi^{(2)}$ is responsible for the nonlinear effects like second-harmonic generation, sum-frequency generation, etc. whereas the third-order susceptibility $\chi^{(3)}$ is responsible for the third-harmonic generation, the Kerr nonlinearity, etc. However, $\chi^{(2)} = 0$ for a medium that has inversion symmetry like liquids, gases, amorphous solids including silica. Nevertheless, for the sake of completeness we will mention the second-order nonlinearities as well as the third-order ones.

As it was stated before, these nonlinear effects can only be seen for very intense electric fields approaching to the electric field in an atom. Using the Bohr model, we can estimate that this electric field should be on the order of 10^{12} V/m. Since the value of $\chi^{(1)}$ is around unity, we may estimate the value of $\chi^{(2)}$ and $\chi^{(3)}$ as 10^{-12} m/V and 10^{-24} m^2/V^2 respectively. This is why we may safely ignore the higher-order terms after $\chi^{(3)}$ in the scope of this thesis.

Let's suppose we have an intense electric field simply given by

$$E(t) = E_1 \exp(-i\omega_1 t) + E_2 \exp(-i\omega_2 t) + c.c. \tag{1.5.4}$$

Then the induced second-order polarization will be

$$P^{(2)}(t) = \varepsilon_0 \chi^{(2)} [E_1^2 \exp(-i2\omega_1 t) + E_2^2 \exp(-i2\omega_2 t) + 2E_1 E_2 \exp(-i(\omega_1 + \omega_2)t)$$

$$+ 2E_1 E_2^* \exp(-i(\omega_1 - \omega_2)t) + c.c + 2E_1 E_1^* + 2E_2 E_2^*]. \tag{1.5.5}$$

The last two terms have no frequency dependence and just create a static electric field in the medium. Examining the other terms, we can describe the second-order nonlinear effects [32].

Second-harmonic generation (SHG) is one of the most widely utilized nonlinear processes in laser community. Here, two photons at the same frequency ω are united to create a photon at the frequency 2ω in a single quantum mechanical process. This is illustrated in Fig. 1.5.1(a). In Fig. 1.5.1(b), the solid line is the ground state and the dashed lines are the virtual levels. The first two terms on the right side of Eq. 1.5.5 both represents this process.

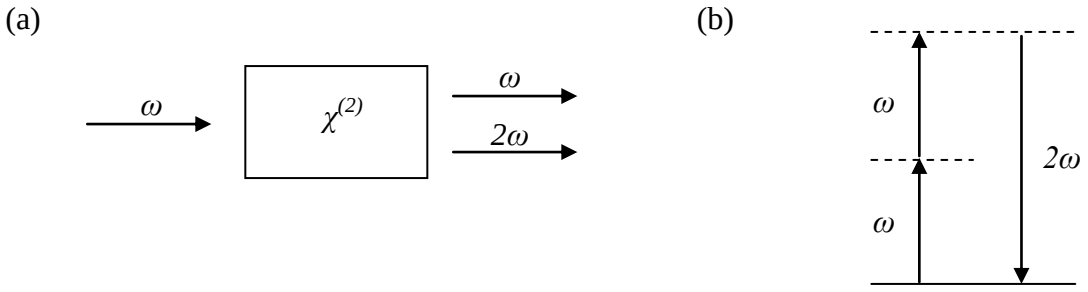

Figure 1.5.1. (a) Illustration and (b) energy-level diagram of SHG.

Sum-frequency generation (SFG) is analogous to SHG, except that here the two input frequencies are different (Fig. 1.5.2). The third term on the right side of Eq. 1.5.5 represents this process.

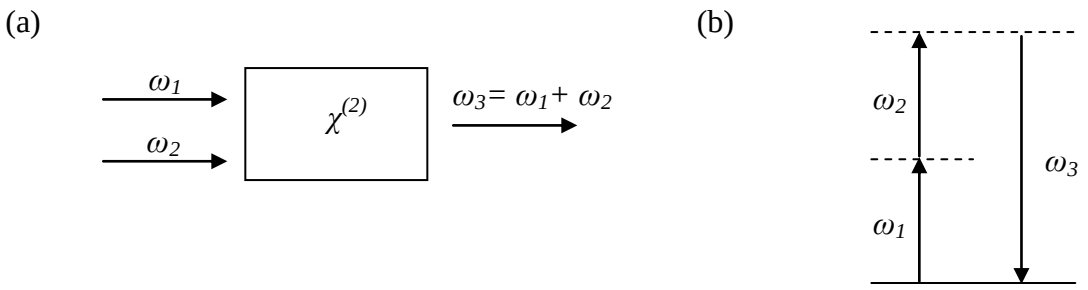

Figure 1.5.2. (a) Illustration and (b) energy-level diagram of SFG.

Difference-Frequency Generation (DFG) is similar to the SFG, this time a photon with a frequency of ω_1- ω_2 is created (Fig. 1.5.3). The fourth term on the right side of Eq. 1.5.5 represents this process.

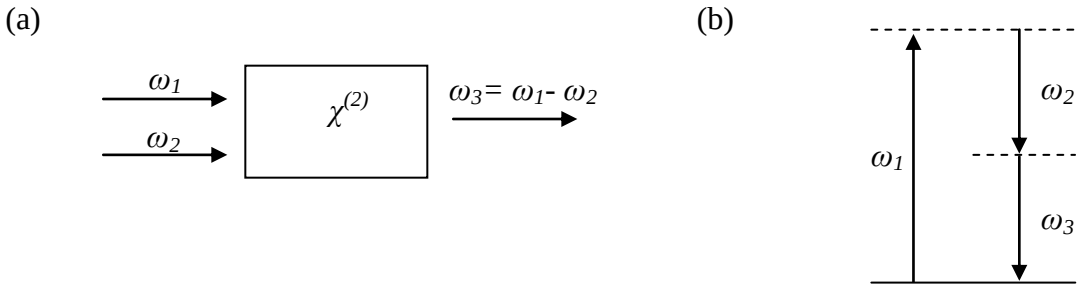

Figure 1.5.3. (a) Illustration and (b) energy-level diagram of DFG.

Note that only one of these frequency components will be present with any appreciable intensity in the radiation generated by the nonlinear optical medium. The reason is that these processes require phase-matching condition, which can be satisfied for one of them at a time.

For the third-order polarization effects, an applied electric field consisting of three frequency components have to be considered for a full understanding;

$$E(t) = E_1\exp(-i\omega_1 t) + E_2\exp(-i\omega_2 t) + E_3\exp(-i\omega_3 t) + c.c. \qquad (1.5.6)$$

In this case calculated $P^{(3)}(t)$ contains 44 different frequency components corresponding to distinct mixing processes and it is a very complicated expression. For the purpose of simplicity and sufficiency, the simplest case in which the applied field with a single frequency will be considered;

$$E(t) = E\cos\omega t. \qquad (1.5.7)$$

Through the use of a trigonometric identity, the third-order nonlinear polarization can be found as;

$$P^{(3)}(t) = \varepsilon_0 \chi^{(3)} \left[\frac{1}{4} E^3 \cos 3\omega t + \frac{3}{4} E^3 \cos \omega t\right]. \tag{1.5.8}$$

In Eq. 1.5.8, each term corresponds to a different nonlinear process, which will be briefly introduced below.

Third-harmonic generation (THG) is a nonlinear response at a frequency of 3ω created by an applied field at a frequency of ω, which is described by the first term on the right side of Eq. 1.5.8 and illustrated in Fig. 1.5.4. In this process three photons at frequency ω are used to create one photon at frequency 3ω in a single quantum mechanical process.

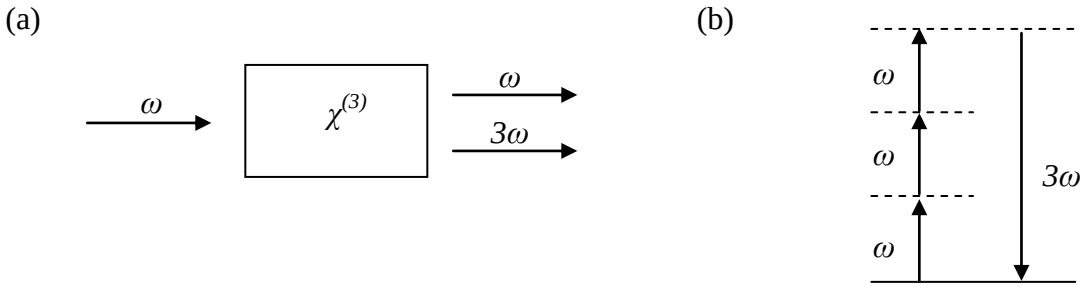

Figure 1.5.4. (a) Illustration and (b) energy-level diagram of THG.

Kerr nonlinearity, which plays an important role in fiber lasers, is described by the second term in Eq. 1.5.8. It is a nonlinear contribution at the same frequency of the incident field. Hence, it leads to a nonlinear contribution to the refractive index experienced by the incident field at frequency ω. The nonlinear refractive index can be represented as

$$n = n_0 + \Delta n_{NL} = n_0 + n_2 I, \tag{1.5.9}$$

where n_0 is the linear refractive index, n_2 is a constant that determines the strength of the optical nonlinearity and I is the intensity of the incident field, which are given by

$$n_2 = \frac{3}{8n_0}\chi^{(3)}, \tag{1.5.10}$$

$$I = \frac{1}{2}n_0\varepsilon_0 c|E|^2. \tag{1.5.11}$$

For silica fibers, the nonlinearity coefficient is around 2.3×10^{-20} m^2/W.

All the described processes above are parametric processes in which initial and final quantum mechanical states of the system are identical. However, for nonparametric processes this is not the case; there is a population transfer between two real states. This means that the energy will not be conserved and these processes should be explained by a complex susceptibility. The followings are some examples of nonparametric (inelastic) processes.

Saturable absorption refers to a decrease of absorption with increasing intensity, which is common for many materials that respond to light similar to a two-level system. It is an important factor in mode-locking of fiber lasers as it enables, together with gain, creation of an effective nonlinear gain. The dependence of the measured absorption coefficient α on the intensity I of the incident field is given by

$$\alpha = \frac{\alpha_0}{1 + I/I_{sat}}, \tag{1.5.12}$$

where α_0 is the low-intensity absorption coefficient and I_{sat} is the saturation intensity. Saturable absorption need not arise from actual absorption by a material; there are also

nonlinear optical schemes such as nonlinear polarization rotation or nonlinear loop mirrors that result in artificial saturable absorption.

Two-photon absorption, which is illustrated in Fig. 1.5.5, is a process where two photons are simultaneously absorbed by an atom and a transition occurs between a lower and a high state, which are both real atomic energy levels. In contrast with linear optics, the two-photon absorption coefficient $\sigma = \sigma^{(2)} I$ increases linearly with the intensity, which means that the atomic transition rate R is proportional to the square of the intensity as

$$R = \frac{\sigma I}{\hbar\omega} = \frac{\sigma^{(2)} I^2}{\hbar\omega}. \tag{1.5.13}$$

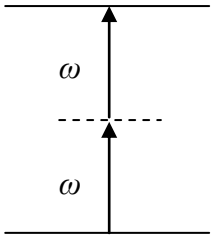

Figure 1.5.5. Energy-level diagram of two-photon absorption.

Stimulated Raman scattering (SRS) illustrated in Fig. 1.5.6 and *stimulated Brillouin scattering (SBS)* are similar to each other. In these processes, the incident photon at frequency ω is annihilated and a photon at the Stokes frequency $\omega_s = \omega - \omega_v$ is created, leaving the atom (molecule) in an (vibrational) excited state with energy $\hbar\omega_v$ after the scattering, which corresponds to either an optical (SRS) or an acoustic phonon (SBS). Due to the very limited gain bandwidth of the SBS process, it is not effective and can be safely

ignored for the broadband optical spectra as required for ultrashort pulse propagation. However, SRS can be a significant contributor for ultrashort pulses and must, in general, be taken into account.

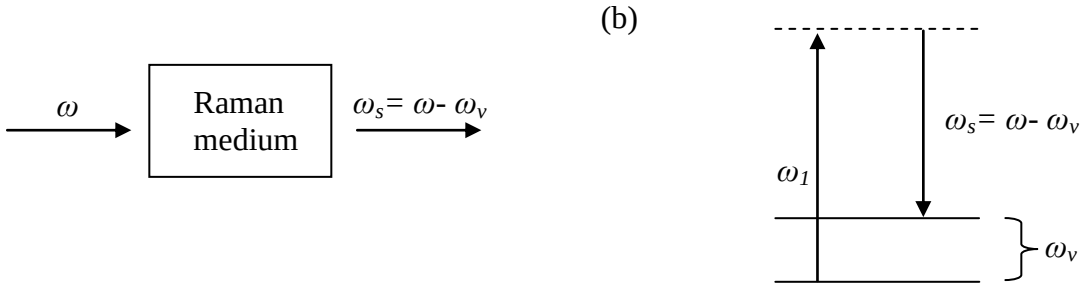

Figure 1.5.6. (a) Illustration and (b) energy-level diagram of stimulated Raman scattering.

Chapter 2

Fiber Lasers and Amplifiers

2.1. Pulse Propagation

Recall that a nonmagnetic, homogenous medium with no free charges is governed by the following wave equation

$$\nabla^2 \boldsymbol{E}(\boldsymbol{r},t) - \frac{1}{c^2}\frac{\partial^2 \boldsymbol{E}(\boldsymbol{r},t)}{\partial t^2} = \mu_0 \frac{\partial^2 \boldsymbol{P}(\boldsymbol{r},t)}{\partial t^2}. \tag{2.1.1}$$

While solving this equation for the fiber modes, we assumed that the nonlinear part of the polarization is small and ignorable. This is acceptable for calculating the fiber modes but for short pulse propagation we have to include the nonlinear part since the intensity at the peak of an ultrashort pulse can be extremely high. When only the linear polarization $\boldsymbol{P}_L(\boldsymbol{r},t) = \varepsilon_0 \chi^{(1)} \boldsymbol{E}(\boldsymbol{r},t)$ is considered, it is straight forward to take the Fourier transform of the wave equation and write it in frequency domain as in Eq. 1.3.9. However, if the nonlinear part is included, this is not an easy task. In general, polarization can be written in terms of the powers of $\boldsymbol{E}(\boldsymbol{r},t)$ as

$$\boldsymbol{P}(\boldsymbol{r},t) = \varepsilon_0\left(\chi^{(1)}\boldsymbol{E}(\boldsymbol{r},t) + \chi^{(2)}\boldsymbol{E}^2(\boldsymbol{r},t) + \chi^{(3)}\boldsymbol{E}^3(\boldsymbol{r},t) \ldots\right) = \boldsymbol{P}_L + \boldsymbol{P}_{NL}. \tag{2.1.2}$$

Actually, we are able to write this expression by assuming that the polarization response of the medium is instantaneous. This is a good assumption for the electronic response since the reconfiguration time of an electron cloud is ≤ 1 fs. However, the vibrational response can be quite slow (~60 fs for Raman scattering) and will be included later in this section.

In Eq. 2.1.2, the effect of each term is significantly weaker than its successor. Also, for a medium with inversion symmetry, $\chi^{(2)} = 0$ and the next nonzero term is $\chi^{(3)}$. For the scope of this thesis, only terms up to third-order will be considered. In this case, the nonlinear part of the polarization is simply

$$\boldsymbol{P}_{NL}(\boldsymbol{r}, t) = \varepsilon_0 \chi^{(3)} \boldsymbol{E}^3(\boldsymbol{r}, t). \tag{2.1.3}$$

In order to be able to transform the wave equation into the frequency domain, we will assume the nonlinear part can be approximated by

$$\boldsymbol{P}_{NL}(\boldsymbol{r}, t) \cong \varepsilon_{NL} \varepsilon_0 \boldsymbol{E}(\boldsymbol{r}, t), \tag{2.1.4}$$

where ε_{NL} is the nonlinear part of the dielectric constant. Since the envelope of $\boldsymbol{E}(\boldsymbol{r}, t)$ is a slowly varying function, ε_{NL} is assumed to be locally constant with a value of

$$\varepsilon_{NL} = \frac{3}{4} \chi^{(3)} |E(\boldsymbol{r}, t)|^2, \tag{2.1.5}$$

where the constant in the front comes from Eq. 1.5.8. In this case, we can again write the wave equation in the form of Eq. 1.3.9 as

$$\nabla^2 E(\boldsymbol{r}, \omega) + \varepsilon_r(\omega) \frac{\omega^2}{c^2} E(\boldsymbol{r}, \omega) = \nabla^2 E(\boldsymbol{r}, \omega) + \beta(\omega) E(\boldsymbol{r}, \omega) = 0, \tag{2.1.6}$$

with a difference that the total dielectric constant is now given by

$$\varepsilon_r(\omega) = 1 + \varepsilon_L + \varepsilon_{NL} = 1 + \chi^{(1)}(\omega) + \frac{3}{4}\chi^{(3)}(\omega)|E(\boldsymbol{r},t)|^2, \tag{2.1.7}$$

which takes into account the nonlinear contribution as well as the linear contribution of the polarization.

On the other hand, the electric field has a time structure that has a rapidly and slowly varying component. The slow timescale is the width of the pulse, which is typically on the order of 100 fs or larger. The fast timescale is the optical cycle, which is on the order of $\lambda/c \approx 3$ fs. Hence it is useful to separate these time scales by writing the electric field as a product of a slowly varying amplitude and a plane wave;

$$E(\boldsymbol{r},t) = A(\boldsymbol{r},t)\exp(i\beta_0 z - i\omega_0 t) + c.c. \tag{2.1.8}$$

Here, ω_0 is the central frequency of the spectrum (carrier frequency), β_0 is the corresponding propagation constant to be determined and $A(\boldsymbol{r},t)$ is the slowly varying envelope, which can further be separated into (ρ,ϕ) dependency that defines the modal pattern and (z,t) dependency that defines the propagation.

$$E(\boldsymbol{r},t) = F(\rho,\phi)A(z,t)\exp(i\beta_0 z - i\omega_0 t) + c.c. \tag{2.1.9}$$

This is appropriate because the transverse mode structure in the fiber is to first order independent of propagation length and time. The quickly varying parts in both z and t are expressed as a plane wave, which propagates in the z-direction in a medium with effective index n. The Fourier transform of the above expression is

$$E(\boldsymbol{r},\omega) = F(\rho,\phi)A(z,\omega-\omega_0)\exp(i\beta_0 z) + c.c. \tag{2.1.10}$$

Substituting this into the wave equation results in two independent relations

$$\frac{\partial^2 F(\rho,\phi)}{\partial \rho^2}+\frac{1}{\rho^2}\frac{\partial^2 F(\rho,\phi)}{\partial \phi^2}+\frac{1}{\rho}\frac{\partial F(\rho,\phi)}{\partial \rho}+[\beta^2(\omega)-\beta_0^2]F(\rho,\phi)=0, \qquad (2.1.11)$$

$$\frac{\partial^2 A(z,\omega-\omega_0)}{\partial z^2}+2i\beta_0\frac{\partial A(z,\omega-\omega_0)}{\partial z}+[\beta^2(\omega)-\beta_0^2]A(z,\omega-\omega_0)=0. \qquad (2.1.12)$$

The first equation was solved before in order to find the fiber mode distribution $F(\rho,\phi)$ and propagation constant β_0. Inclusion of nonlinear polarization term has no effect on $F(\rho,\phi)$ but β_0 is slightly modified as follows. Dielectric constant can be approximated as

$$\varepsilon_r(\omega)=\left(n_0(\omega)+\Delta n_{NL}(\omega)\right)^2\cong n_0^2(\omega)+2n_0(\omega)\Delta n_{NL}(\omega), \qquad (2.1.13)$$

where the loss $\alpha(\omega)$ is implicitly embedded into $\Delta n_{NL}(\omega)$ as

$$\Delta n_{NL}(\omega)=n_2(\omega)|A(z,\omega-\omega_0)|^2+\frac{ic}{2\omega}\alpha(\omega). \qquad (2.1.14)$$

The nonlinear refractive index leads a corresponding nonlinear term in the propagation constant, which can be expressed as

$$\beta(\omega)=\beta_L(\omega)+\Delta\beta_{NL}(\omega), \qquad (2.1.15)$$

and calculated from

$$\Delta\beta_{NL}(\omega)=\frac{\omega}{c}\frac{\iint \Delta n_{NL}(\omega)|F(\rho,\phi)|^2\rho\mathrm{d}\rho\mathrm{d}\phi}{\iint|F(\rho,\phi)|^2\rho\mathrm{d}\rho\mathrm{d}\phi}\cong\frac{\omega}{c}\Delta n_{NL}(\omega). \qquad (2.1.16)$$

In the second equation, we can neglect the first term with second derivative since $A(z, \omega - \omega_0)$ is a slowly varying function of z. Also $\beta(\omega)$ and β_0 are very close to each other so we can use $\beta^2(\omega) - \beta_0^2 \cong 2\beta_0(\beta(\omega) - \beta_0)$ in order to obtain

$$\frac{\partial A(z, \omega - \omega_0)}{\partial z} - i[\beta(\omega) - \beta_0]A(z, \omega - \omega_0) = 0. \tag{2.1.17}$$

Now, if we write the truncated Taylor series expansion of β about ω_0 up to the second-order term

$$\beta(\omega) = \beta_0 + \beta_1(\omega - \omega_0) + \frac{1}{2}\beta_2(\omega - \omega_0)^2 + \Delta\beta_{NL}, \tag{2.1.18}$$

where $\Delta\beta_{NL} = \Delta\beta_{NL}(\omega_0)$ and inserting it into 2.1.12 yields

$$\frac{\partial A(z, \omega - \omega_0)}{\partial z} - i\left[\beta_1(\omega - \omega_0) + \frac{1}{2}\beta_2(\omega - \omega_0)^2 + \Delta\beta_{NL}\right]A(z, \omega - \omega_0) = 0. \tag{2.1.19}$$

Taking the inverse Fourier transform in terms of $\omega - \omega_0$ gives

$$\frac{\partial A(z,t)}{\partial z} + \beta_1\frac{\partial A(z,t)}{\partial t} + \frac{ik\beta_2}{2}\frac{\partial^2 A(z,t)}{\partial t^2} = i\Delta\beta_{NL}A(z,t). \tag{2.1.20}$$

This equation can further be simplified by a coordinate transformation. If the retarded time is used instead of the proper time such that

$$\tau = t - \frac{1}{v_g}z = t - \beta_1 z, \tag{2.1.21}$$

we may obtain the following equation

$$\frac{\partial A(z,\tau)}{\partial z} + \frac{i\beta_2}{2}\frac{\partial^2 A(z,\tau)}{\partial \tau^2} = i\Delta\beta_{NL}A(z,\tau). \tag{2.1.22}$$

Finally, we can insert $\Delta\beta_{NL}$ obtained from Eq. 3.1.15 so that

$$\frac{\partial a(z,\tau)}{\partial z} + \frac{i\beta_2}{2}\frac{\partial^2 a(z,\tau)}{\partial \tau^2} + \frac{\alpha(\omega_0)}{2}a(z,\tau) = i\gamma(\omega_0)|a(z,\tau)|^2 a(z,\tau). \tag{2.1.23}$$

Here, we used $a(z,\tau)$, which is the normalized version of $A(z,\tau)$, such that $|a(z,\tau)|^2$ gives the optical power. The nonlinear parameter $\gamma(\omega_0)$ is defined as

$$\gamma(\omega_0) = \frac{n_2(\omega_0)\omega_0}{cA_{eff}}, \tag{2.1.24}$$

where the effective area A_{eff} can be found from the modal distribution function by

$$A_{eff} = \frac{(\iint |F(\rho,\phi)|^2 \rho \mathrm{d}\rho \mathrm{d}\phi)^2}{\iint |F(\rho,\phi)|^4 \rho \mathrm{d}\rho \mathrm{d}\phi}. \tag{2.1.25}$$

Note that if $F(\rho,\phi)$ is approximated by a Gaussian function as in Eq. 1.3.17, effective area is simply

$$A_{eff} = \pi w^2. \tag{2.1.26}$$

Because of the resemblance, Eq. 2.1.22 is called the *nonlinear Schrödinger equation (NLSE)* and is used to describe the propagation of ultra short pulses through optical fibers, taking into account chromatic dispersion by β_2, fiber losses by α and fiber nonlinearities by γ.

It is useful to introduce two length scales, *dispersion length* L_D and *nonlinear length* L_{NL}. This makes it possible to compare the relative strengths of effects over the propagation distance. These lengths are defined as;

$$L_D = \frac{\tau_0^2}{\beta_2}, \qquad L_{NL} = \frac{1}{\gamma P_0}, \tag{2.1.27}$$

where τ_0 is the pulse width and P_0 is the pulse peak power.

There is a simple solution to this equation if β_2 is assumed to be negative (i.e. anomalous dispersion). This solution is called as "soliton", which was first observed in 1834 by Scott Russell in water waves propagating with undistorted phase over several kilometers through a canal. Assuming no losses, Eq. 2.1.23 can be written in the following form

$$\frac{\partial a}{\partial z} = i\gamma|a|^2 a - \frac{i\beta_2}{2}\frac{\partial^2 a}{\partial \tau^2}. \tag{2.1.28}$$

Here, we are searching a solution such that it will preserve its shape while propagating through the fiber. After some calculations, it can be verified that a hyperbolic secant function satisfies this condition:

$$a(z,\tau) = \sqrt{\frac{-\beta_2}{\gamma\tau_0^2}}\exp\left(-\frac{i\beta_2 z}{2\tau_0^2}\right)\operatorname{sech}\left(\frac{\tau}{\tau_0}\right) \tag{2.1.29}$$

After this point, we will develop the NLSE a bit more by adding the third-order dispersion (TOD) term β_3, which becomes significant for extremely short pulses (< 100 fs). Also, the spectrum of a short pulse can be wide enough that the Raman scattering will transfer

energy from high to low frequency components within the pulse, which is called the self frequency shift. Now, we have to write Eq. 2.1.3 in a more careful manner

$$\boldsymbol{P}_{NL}(\boldsymbol{r},t) = \varepsilon_0 \chi^{(3)} \boldsymbol{E}(\boldsymbol{r},t) \int_{-\infty}^{t} R(t-t_1)|\boldsymbol{E}(\boldsymbol{r},t_1)|^2 dt_1, \tag{2.1.30}$$

including the delayed response of the polarization by the response function $R(t)$ such that $\int_{-\infty}^{\infty} R(t)dt = 1$. After some calculations [31], the following result can be obtained:

$$\frac{\partial a}{\partial z} + \frac{i\beta_2}{2}\frac{\partial^2 a}{\partial \tau^2} - \frac{\beta_3}{6}\frac{\partial^3 a}{\partial \tau^3} + \frac{\alpha}{2}a = i\gamma\left[|a|^2 a + \frac{i}{\omega_0}\frac{\partial}{\partial \tau}(|a|^2 a) - T_R a \frac{\partial |a|^2}{\partial \tau}\right], \tag{2.1.31}$$

where T_R is the first moment of the nonlinear response function given by $T_R = \int_{-\infty}^{\infty} tR(t)dt$. The term with β_3 is responsible for third-order dispersion, ω_0^{-1} is for self-steepening and shock formation and T_R is for the self-frequency shift. Experimentally, it was found that $T_R = 3$ fs around 1.5 μm wavelength.

2.2. Gain

Optical gain through stimulated emission is a key ingredient of any laser. By doping the core of a fiber with suitable types of atoms, it is possible to obtain lasing at selected wavelengths. For certain applications like medicine, metrology, etc. where the eye-safe region (1.4-2.1 μm) is preferred, dopants such as erbium (1.5 μm), thulium (1.9 μm) and holmium (2.1 μm) are suitable. However, if pure power is required such as in material processing, the most suitable dopant is ytterbium (1.06 μm) because of its small quantum

defect. Also Yb ions have a single excited state, which means it is relatively immune to excited state absorption and self-quenching, thus Yb can be doped in higher concentrations.

Depending on the energy levels of the dopants, lasing schemes can be classified as a three-level (like Yb) or four-level (like Er) scheme (Fig. 2.2.1). In either case, dopants absorb pump photons to reach an excitation stage and then relax rapidly into a lower-energy excited state. The lifetime of this intermediate state is usually long (~1 ms for Yb, 10 ms for Er), and the stored energy is used to amplify incident light through stimulated emission. The difference between the three and four-level lasing schemes is the energy state to which the dopant relaxes after a stimulated-emission event. For a three-level case, the dopant ends up in the ground state, whereas for a four-level case, it ends up in an excited state.

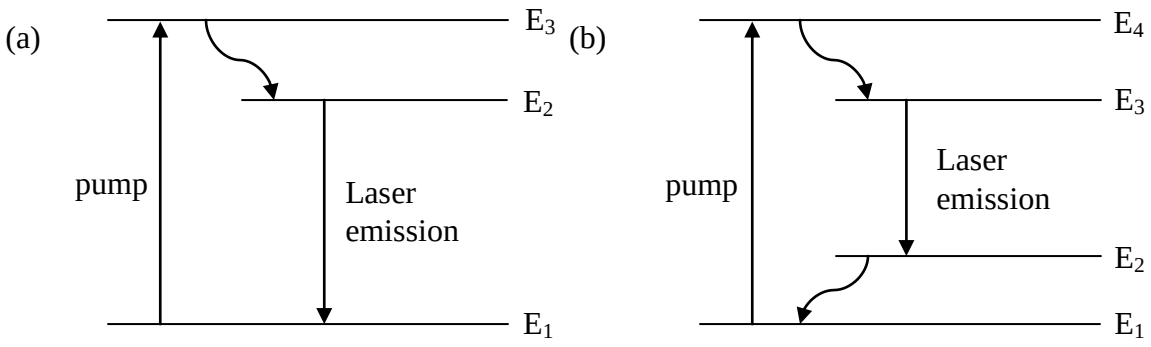

Figure 2.2.1. Illustration of (a) three and (b) four-level lasing schemes

Optical pumping creates the necessary population inversion between the excited and lower energy states and provides the optical gain as given by

$$g(\omega) = \frac{g_{ss}}{1 + (\omega - \omega_a)^2 \tau_2^2 + \frac{\tau_1 P}{E_{sat}}} = \frac{g_{ss}}{1 + (\omega - \omega_a)^2 \tau_2^2 + \frac{P}{P_{sat}}}, \qquad (2.2.1)$$

where g_{ss} is the small signal gain at the peak of the gain spectrum, ω is the frequency of the incident signal, ω_a is the atomic transition frequency and P is the optical power of the signal being amplified, P_{sat} is the saturation power, E_{sat} is the saturation energy, τ_1 is the gain relaxation time and τ_2 is the dipole relaxation time, which is usually on the order of 0.1 ps for the rare-earth doped glasses.

According to Eq. 2.2.1, the frequency dependence of the gain has a Lorentzian profile with a FWHM given by $\Delta\omega_g = 2/\tau_2$. However, the actual gain spectrum of a fiber laser can deviate significantly from the Lorentzian profile. The shape and the width of the gain spectrum are sensitive to core composition (i.e. the amorphous nature of the silica and the presence of other co-dopants such as aluminum or germanium). The measured absorption and emission spectrums of an Yb-doped silica fiber can be seen in Fig. 2.2.2.

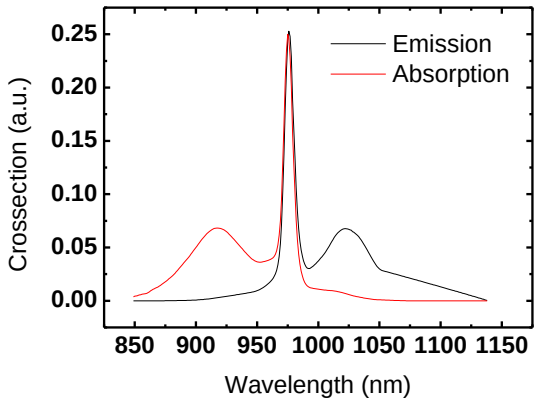

Fig. 2.2.2. Absorption (red) and emission (black) cross-sections of Yb-doped silica glass.

It can be seen that the real spectrum strongly deviates from the Lorentzian function, hence it is better to use the experimental data directly. Another important point is that when a

very high energy ($E_s \geq E_{sat}$) pulse enters in a gain medium, it will deplete the excited ions in the medium and experience a reduced gain approximated by

$$g' \cong g\frac{E_{sat}}{E_s}\left[1 - \exp\left(\frac{-E_s}{E_{sat}}\right)\right]. \tag{2.2.2}$$

Incorporating the gain term into the NLSE given by Eq. 2.1.23 is not an easy task [33], and there is more than one possible approach to modeling this effect, but a reasonably broadly applicable, yet simple result is given by

$$\frac{\partial a}{\partial z} + \frac{i(\beta_2 + ig\tau_2^2)}{2}\frac{\partial^2 a}{\partial \tau^2} + \frac{\alpha - g}{2}a = i\gamma|a|^2 a. \tag{2.2.3}$$

Note that the gain is simply added near the loss term with the inverse sign. However, the dispersion term is slightly modified by the "gain dispersion", which is caused by the finite gain bandwidth of the doped fibers. This equation, with the addition of saturable absorption (of the form $\delta|a|^2 a$) would constitute the so-called "master equation of mode-locking" [34].

2.3. Mode-locking

Mode-locking is, in simplified terms, to induce a fixed phase relationship between the longitudinal modes of a resonant cavity. There can be many modes in a ring cavity, which satisfy

$$n\lambda_n = L, \tag{2.3.1}$$

where L is the length of the ring cavity, n is the mode number and λ_n is the corresponding wavelength. Interference between these modes produces pulses, which can be as short as femtoseconds depending on the number of the modes involved. Of course this is related to spectral width of the pulse as it can be seen from the relation above. The total electric field in the cavity can be written in terms of the fields of separate modes as

$$E(z,t) = \sum_n E_n(z,t) = \sum_n E_{n,0}\, e^{ik_n z - i\omega_n t} = \sum_n \left|E_{n,0}\right| e^{i\phi_n}\, e^{ik_n z - i\omega_n t}, \qquad (2.3.2)$$

where $E_{n,0}$ is the complex amplitude of the n^{th} mode and ϕ_n is the phase. For simplicity let's assume the amplitude of all modes are the same (i.e. square shaped spectrum). Then we can write the intensity as

$$I(z,t) = E(z,t)E^*(z,t) = |E_0|^2 \sum_{n=1}^{N} \sum_{m=1}^{N} e^{i(\phi_n - \phi_m)(m-n)\Omega\left(\frac{z}{c} - t\right)}, \qquad (2.3.3)$$

where the frequency difference between two consecutive modes is defined as

$$\Omega = \omega_{n+1} - \omega_n = \frac{2\pi c}{L}. \qquad (2.3.4)$$

For the mode-locking condition, all of the modes should have a fixed phase relation. Then we can write the intensity in a simpler way

$$I(z,t) = |E_0|^2 e^{i\delta\phi} \sum_{n=1}^{N} \sum_{m=1}^{N} e^{i(m-n)\Omega\left(\frac{z}{c} - t\right)}. \qquad (2.3.5)$$

The term in the summation will be equal to unity for the following condition:

$$\Omega\left(\frac{z}{c}-t\right)=2\pi j, \tag{2.3.6}$$

where j is an integer. In this case, the intensity is the maximum, which means that a pulse is formed with

$$I_{max}=N^2|E_0|^2\equiv N^2 I_0. \tag{2.3.7}$$

The temporal and spatial separation of neighboring pulses can be derived from Eq. 3.3.6 as;

$$\Delta z=L\,,\qquad \Delta t=\frac{L}{c}=T. \tag{2.3.8}$$

This means the intensity maxima repeat with the roundtrip time T of the laser resonator and there is only one maximum inside the cavity at any time. The peak of the pulses is proportional to N^2. We can also calculate full-width-half-maximum (FWHM) of the pulses; the superposition of N modes is assumed to be similar to the interference of N planar waves at a fixed time $t=0$. Using geometric series;

$$I(t)=I_{max}\frac{\sin^2\left(\frac{N\Omega}{2}t\right)}{\sin^2\left(\frac{\Omega}{2}t\right)}. \tag{2.3.9}$$

The FWHM of the pulses can be derived from the above equation, which yields a pulse width decreasing with the number of modes, as expected;

$$\Delta T_{FWHM}=\frac{L}{Nc}=\frac{1}{N}T. \tag{2.3.10}$$

The fixed phase relation between the superposed modes can be achieved by creating a modulated gain (or loss) in the cavity with frequency Ω. All the techniques for mode-locking rely on this principle. Due to this modulation, the electromagnetic field in the cavity gets additional time dependence;

$$E_n(z,t) = \left[E_{n,0} + E_{n,mod}\cos\Omega t\right]e^{ik_n z - i\omega_n t}$$

$$= \left[E_{n,0}e^{-i\omega_n t} + E_{n,mod}\frac{1}{2}(e^{-i\Omega t} + e^{i\Omega t})e^{-i\omega_n t}\right]e^{ik_n z}$$

$$= \left[E_{n,0}e^{-i\omega_n t} + \frac{1}{2}E_{n,mod}e^{-i\omega_{n+1} t} + \frac{1}{2}E_{n,mod}e^{-i\omega_{n-1} t}\right]e^{ik_n z}. \qquad (2.3.11)$$

From this equation, it can be seen that the time dependence in every mode induces sidebands whose frequencies coincide with the frequencies of neighboring modes. Since this is valid for the total bandwidth, phase synchronization, so called "mode-lock", between all longitudinal modes is achieved.

There are several methods to create the desired gain or loss modulation in the resonator in order to achieve mode-locking, but in general giving loss is the easier and preferred one. These methods are mainly divided into two subgroups; active and passive mode-locking. For active mode-locking, generally (acousto-optic or electro-optic) modulators are utilized, while for passive mode-locking, saturable absorbers are used. As a saturable absorber, usually nonlinear polarization evolution (NPE) is used. Since the polarization rotation (due to Kerr effect) at the peak of a pulse will be higher than at the wings, it is possible to selectively pass the peak of the pulse through a polarizer beam cube (PBS) by carefully controlling the polarization so that NPE acts as a saturable absorber. The pulse formation is favored by the saturable absorber since the phase locked modes experience a lower loss.

2.4. Types of Fiber Lasers

We can classify the fiber lasers according to their mode-locking regimes: Soliton, stretched-pulse, all-normal-dispersion, similariton and soliton-similariton. Now we will focus on the differences and the properties of these regimes in detail. In a fiber laser cavity, there is a rich interplay between the four basic effects, namely Kerr nonlinearity, dispersion, gain and saturable absorption. These can be arranged or managed in many different ways leading to different laser types. However, the main rule remains the same; the pulse should somehow return to its initial state (both in time and frequency domains) after one roundtrip inside the cavity.

Soliton lasers are the first developed mode-locked fiber lasers. We have previously stated that the solution in the following form satisfies the NLSE equation and we called it a soliton:

$$a(z,\tau) = a_0 \operatorname{sech}\left(\frac{\tau}{\tau_0}\right) \tag{2.4.1}$$

A *soliton laser* [20, 21] can be defined as a fiber laser in which pulse maintains its shape throughout the cavity roundtrip. This means that the laser cavity should be mainly composed of anomalous dispersion fibers (Fig 2.4.1). This is possible at 1.5 μm wavelength in silica fibers where the dispersion is negative. The pulses are amplified in the gain medium where only their amplitude increases. In general, nonlinear polarization rotation (NPE) is used as a saturable absorber. In this case, it is possible to take the output of the laser from the rejection port of the NPE. Then, the pulse travels throughout the cavity without losing its shape and finally returns to its initial state.

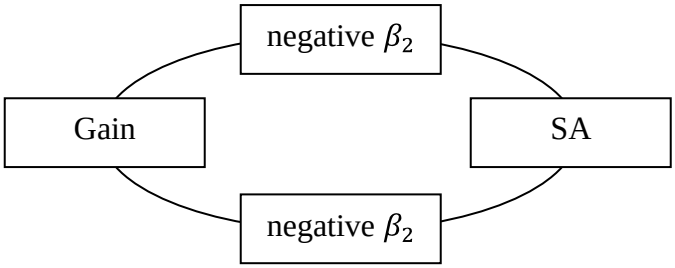

Fig 2.4.1 Schematic of a soliton laser. SA: Saturable absorber.

A modified version of the soliton laser is the *stretched pulse laser* [22], which can be seen in Fig. 2.4.2. In this case, there are both anomalous and normal dispersion fiber segments in the cavity, and pulse is allowed to change its shape. Pulse is highly chirped at the exit of the positive-dispersion segment. Then it starts to get narrower. After passing the transform-limited state, it starts to get broader and becomes highly negatively chirped at the exit of the negative-dispersion segment. Similarly it turns back to its original state after propagating through the positive-dispersion fiber.

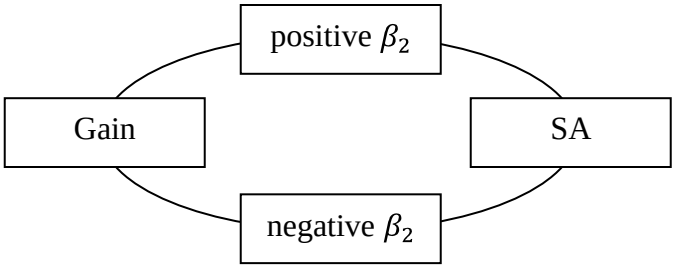

Fig 2.4.2 Schematic of a stretched-pulse laser. SA: Saturable absorber.

A *similariton laser* [23, 24] is qualitatively different from a soliton laser, since the combined effect of normal dispersion and nonlinearity is utilized in it. A similariton, which

will preserve its shape under these conditions, is a parabolic-shaped pulse given in the following form:

$$a(z,\tau) = a_0\sqrt{1-(\tau/\tau_0)^2} \tag{2.4.2}$$

The schematic is similar to Fig. 2.4.2. The pulses are propagating in the positive-dispersion fibers self-similarly and then they are compressed in a grating pair without losing their pulse shapes. The similariton lasers can go up relatively higher pulse energies since the self-similar pulses are highly resistant to nonlinearities.

A variant of the similariton laser is the *soliton-similariton laser* [26]. Here, the pulse propagates in the gain fiber (with positive dispersion) as a similariton. After the saturable absorber, a filter is used to change the pulse shape to a soliton and pulse propagates as a soliton through the rest of the cavity (with negative dispersion). At the input of the gain fiber, it turns back to the similariton form, which was the original state.

All-normal dispersion (ANDi) laser [25] differs from the above mode-locked lasers by its cavity, which is completely composed of positive-dispersion fibers (Fig. 2.4.3). The pulse continuously broadens throughout the entire cavity under the influence of both dispersion and nonlinearity. Since the pulse is always highly chirped, its shape in temporal and frequency domains is nearly the same. This means that by using a band-pass filter, it is possible to cut the wings of the pulse in both domains simultaneously such that it returns to its original state. ANDi lasers are especially suitable for building all-fiber cavities in 1 μm wavelength region since they do not require any negative-dispersion segments like a grating pair.

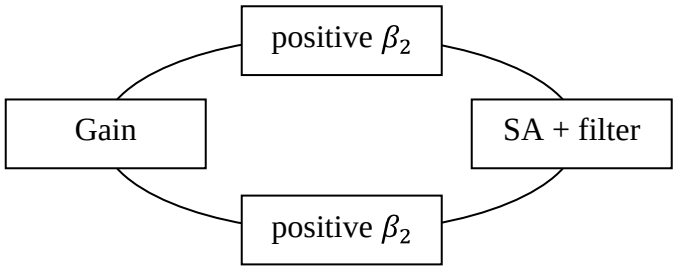

Fig. 2.4.3 Schematic of an ANDi laser. SA: Saturable absorber.

2.5. High Power Fiber Lasers

In this section, an overview of the current situation of the fiber lasers in the world market will be presented. Fig. 2.5.1 shows how the output power level of fiber lasers has increased in the past decade. As it can be seen from the figure, the power level is increasing by ~2.3 dB/year, which is equivalent to a yearly increase of 1.7. Hence, the fiber lasers are entering various new areas where they are replacing the previously used technologies. The main reason for this replacement is the low operation cost and higher than 40% wall plug-in efficiency of fiber lasers. Only direct-diode lasers have a higher efficiency (60%) than this however their beam quality is not comparable with fiber lasers. Nevertheless, direct-diode lasers are still preferable for some applications like welding. The other main competitor in high power arena is CO_2 laser, which has 20% plug-in efficiency and higher maintenance cost but requires a lower initial investment. Also, for scientific purposes, Ti-sapphire lasers are sometimes preferable over fiber lasers if very short pulses below 100 fs are desired.

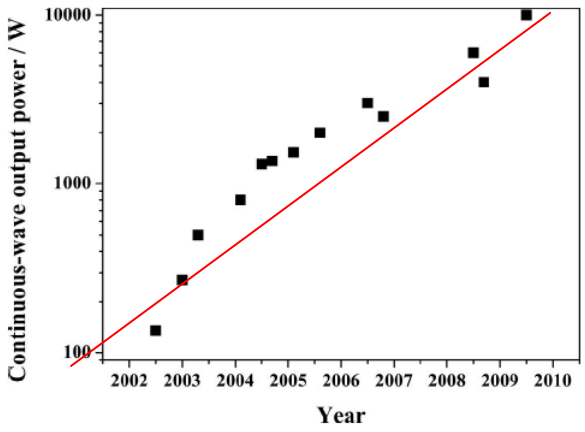

Fig. 2.5.1. Increase of the output power level of continuous-wave fiber lasers with nearly diffraction-limited beam quality [35]. Red line shows the 2.3 dB/year curve.

In 2009, total world laser market was around M$5,400 while the fiber laser market was M$240, which is equivalent to 4.4% market share and continuously increasing [28]. The most significant application area was material processing (M$160) followed by medicine (M$20). The total sales were dominated by high power continuous-wave lasers (40%) followed by pulsed lasers (30%). Average price level of a 1 kW continuous-wave laser was around $100,000 while a 20 W pulsed laser was around $15,000.

2.6. Double-clad Fibers

It is well known that the solid-state pump diodes are required for pumping fiber lasers. Luckily, the energy level of these pump diodes have been increasing very steeply in the past decades. Today, single-emitter pump diodes can give ~50 W of output power while the multi-emitter bars can go up to ~500 W. However, there is a problem; it is impossible to couple this much of power into a single-mode fiber core. Output of these diodes can only

be coupled into fibers with core diameters ranging from 105 μm to 600 μm depending on the power level. For a single-mode fiber, it is only possible to couple around 1 W. This can be understood with "conservation of brightness" principle. Since the brightness level of a solid-state laser is technologically limited, the brightness inside the fiber will also be limited. The only way to increase coupled power is to increase the core diameter. However, there is a practical limit for the core diameter if a single-mode laser operation is desired; it is difficult to produce a preform that would yield a fiber with a *NA* below ~0.05. After this point, the fibers become very sensitive to the bending losses, and the splice losses also increase. For this *NA* value, the maximum single-mode fiber core diameter can be calculated from Eq. 1.2.2 as 15 μm at 1 μm wavelength. Of course, there are some tricks to increase this value without losing the single-mode operation, which will be explained later.

What happens if we had a "brightness converter"? Actually an active double-clad fiber is a kind of brightness converter; it takes low brightness light as an input and gives out high brightness laser output. So we can state that the invention of double-clad fibers [27] is the enabling technology for high power lasers. Fig. 2.6.1 shows the sectional view of a double-clad fiber.

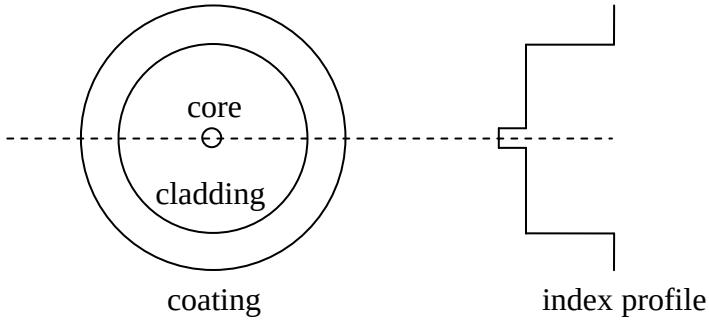

Fig 2.6.1. The cross-sectional structure of a double clad fiber with its index distribution on the right. The dimensions are exactly scaled version of a 25/250DC fiber.

Since *NA* depends on the index difference between neighboring sections, the *NA* of the core is much smaller than that of the cladding, which is 0.46 for an acrylic coating. Note that, rarely the acrylic coating is also coated with a standard high-index polymer for enhanced environmental stability. There are some designs where the coating is also made from (fluorinated) glass. However, it is hard to obtain a *NA* more than 0.25 in this case.

Another interesting design (Fig. 2.6.2) is photonic crystal fibers (PCF) where the guidance in the core is maintained by the small index variation induced by small holes drilled surrounding the core area. Also pump guidance is sustained by this way. However, this time the holes are larger in order to obtain a larger *NA* of 0.8. These structures are very successful for mid-powers. However, there are some questions about their long term mechanical stability for high power operation (> 1 kW). The air gap acts as an insulator, which makes thermal management difficult. Also cleaving and splicing this type of fibers are difficult.

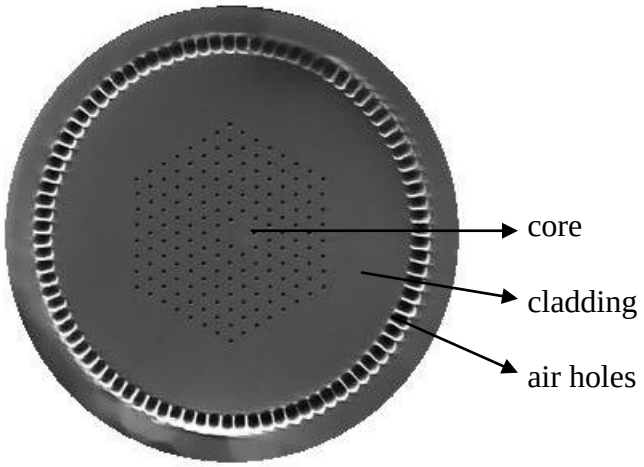

Figure 2.6.2 Air-clad photonic crystal fiber [36].

The working principle of a double-clad fiber is as follows: Suppose that pump light is guided in the multimode cladding area and signal is guided in the core, which is doped with active ions like Yb. Then the pump light occasionally passing through the core region will be absorbed by active ions, which will amplify the signal via stimulated emission. As a result, the low brightness pump light is converted to a high brightness signal light. Note that, if the cladding is circular, there can be some guided modes of pump light whose intensity drops to nearly zero at the center, which means some portion of the pump light will not be absorbed by the Yb ions. In order to solve this problem, the cladding is generally made asymmetric or at least non-circular and up to 30% increase in the absorption coefficient of the fiber can be achieved by this way. Fig. 2.6.3 shows some different designs used to break down the circular symmetry [37].

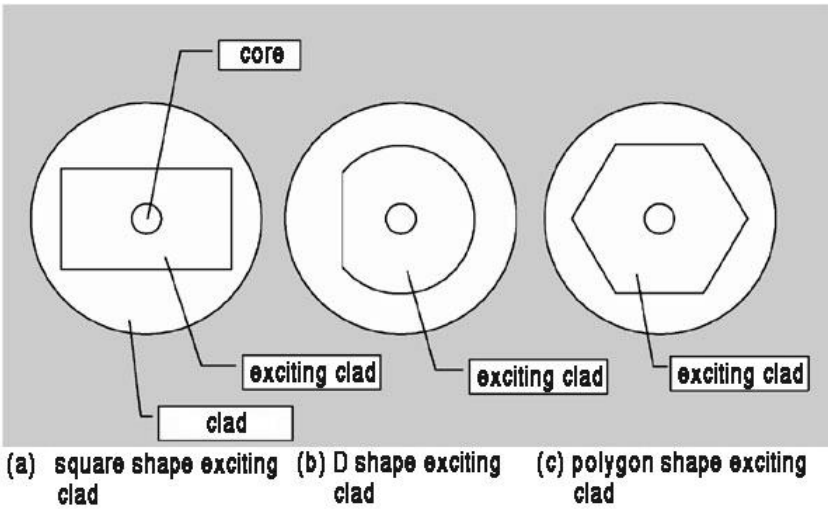

Fig. 2.6.3 Different cladding shapes in order to increase pump absorption.

Although we can increase the maximum coupled pump power by increasing the cladding diameter, this results in using a longer fiber since the absorption coefficient of an active double-clad fiber is proportional with $(a/b)^2$ where a, b are the core and cladding

radiuses, which were defined earlier. However, using a longer fiber brings nonlinear effects together. As a result, we are forced to use larger core diameters by releasing the single-mode core condition. For example, when a core diameter twice as large is used, a four times shorter fiber length will be enough to absorb the same amount of pump power. Since the nonlinearities are proportional to the intensity, we will gain another factor of four from here. As a result, nonlinear effects will be reduced by 16 times, which is desirable, however this brings on the multi-mode operation regime, loosing behind one of the main advantages of fiber lasers; diffraction-limited pulse quality. When processing a material using a beam with $M^2 = 3$ for example, we will need a 9 times more powerful laser system in order to achieve same intensity level on the material.

Fortunately, there are some methods developed in order to use a multi-mode double-clad fiber in single-mode operation. The simplest method uses the fact that the fundamental mode is the least sensitive mode for bending losses. So the fiber can be coiled with a radius such that fundamental mode is subjected to low loss while all the others are subjected to high loss [38]. Similarly, a section (generally the ends) of the fiber can be tapered such that it will selectively pass the fundamental mode [39]. Also a special radial doping distribution may lead to higher amplification of the fundamental mode [40]. Another design is the chirally-coupled core (CCC) fibers [41], where the higher order modes can be suppressed effectively. However, this technology is yet to prove itself. Meanwhile, it is always important to seed the fiber in a correct way without exciting the higher-order modes.

2.7. Pump Combiners

As it was stated, the most powerful fiber lasers in the literature are not the all-fiber designs where the pump light is coupled into the fiber via free space optics. However, this limits the

robustness of the fiber lasers, which is one of the main reasons why they are preferred over the solid state lasers. Hence, some kind of all-fiber structures to couple pump light without going to free space is desired. There are many designs to achieve this goal, which are in general called multi-pump combiners (MPC). Fig. 2.7.1 shows some of them.

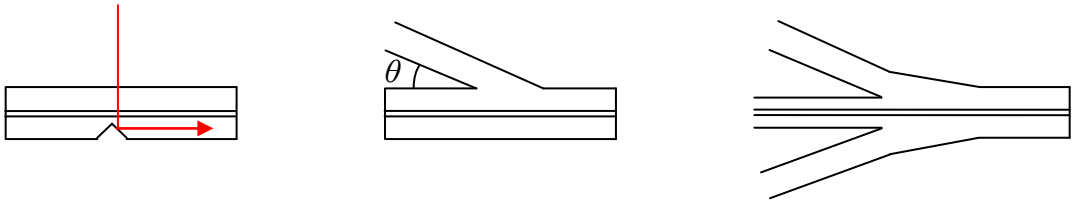

Fig. 2.7.1 Notch coupling, angle coupling, tapered bundle coupling.

In notch coupling, pump light is focused on a notch from where it is reflected inside the fiber. In this design, the area of the beam should be smaller than the notch. In angle coupling pump fiber is fused to the main fiber with an angle of θ. The coupling efficiency is good if $NA_{pump} + \theta \leq NA$. Among the various combiner schemes, tapered bundle coupling is the most extensively used one. A tapered bundle of fibers with six pump channels and one signal channel ready for splicing to the output fiber is shown in Fig. 2.7.2.

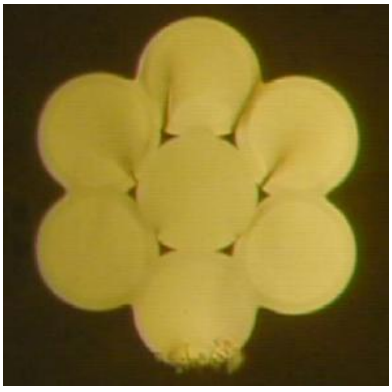

Fig 2.7.2. Cross-sectional view of a fiber bundle [42] composed of 6 pump fibers and 1 signal fiber in the middle.

It is natural to ask how many pump fiber can be tapered and coupled to a given output fiber. The answer comes again from the conservation of brightness principle.

$$d_b NA_b \leq d_o NA_o, \tag{2.7.1}$$

where d_b is the diameter of the whole bundle before tapering, which can be estimated from $d_b = d_i\sqrt{N}$, d_i is the diameter of input fibers, N is the number of fibers in the bundle, NA_b is the largest numerical aperture among those of the input fibers, d_o and NA_o are the cladding diameter and numerical aperture of the output fiber. For example, if $d_i = 125$ μm with $NA_b = 0.15$ and $d_o = 125$ μm with $NA_{pump} = 0.46$, then $N \leq 9$. Some possible configurations are given in Table 2.7.1. In general, their pump power loss is on the order of 0.3 dB.

Input fibers/Output fiber	125 μm, 0.46NA	250 μm, 0.46NA	400 μm, 0.46NA
105/125 μm, 0.15NA	7×1	19×1	61×1
105/125 μm, 0.22NA	4×1	7×1	37×1
200/220 μm, 0.22NA	1×1	4×1	7×1
400/440 μm, 0.22NA	-	1×1	3×1

Table 2.7.1 Various possible MPC configurations [42]. These numbers are chosen such that the bundle shape is as circular as possible.

2.8. Main Limitations

In this section, we will present the factors that mainly limit the high power designs. In fiber lasers, light is strictly confined in the core region and propagates for long distances (several

meters) in a nonlinear medium compared to other solid state lasers. So it is understandable that the nonlinear effects are the main concerns in high power fiber laser design, coming before the material damage or thermal problems.

Stimulated Raman scattering (SRS) is the most important nonlinear effect, which severely limits the performance of a high power system. As explained before, SRS involves conversion of an incident photon to a lower energy scattered photon and an optical phonon. This effectively extracts energy from the main pulse and generates a Stokes wave at a downshifted frequency. The basic equation governing the Raman process is

$$\frac{\mathrm{d}I_s}{\mathrm{d}z} = g_R(\Omega) I_p I_s, \tag{2.8.1}$$

where I_s is the Stokes intensity, I_p is the incident pump intensity, and g_R is the Raman gain coefficient, which is a function of the frequency difference Ω between the pump and Stokes waves. Raman gain coefficient is fundamentally related to the imaginary part of the third-order susceptibility $\chi^{(3)}$. Fig 2.8.1 shows the Raman gain spectrum for silica as a function of Ω taken from Ref. [31].

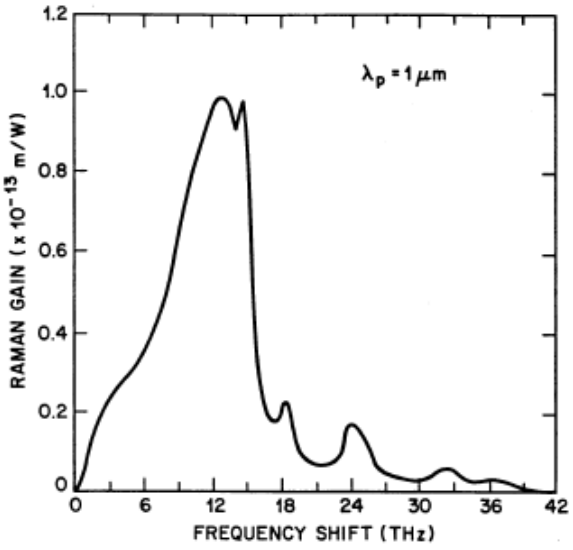

Fig 2.8.1. Raman gain spectrum for silica at 1 μm wavelength [31].

For silica, the Raman spectrum is a continuum because of its amorphous structure unlike many media where the Raman shift occurs in specific frequencies. The peak of the Raman gain is 10^{-13} m/V occurring around 13.2 THz. This means that for a 1060 nm pump wavelength, the peak of the Stokes wave will be around 1120 nm. If we integrate Eq. 2.8.1, we get

$$I_s = I_s(0)\exp\left(g_R I_p L\right). \tag{2.8.2}$$

From here we can deduce two important results. First, the Stokes wave grows exponentially with the pump intensity and the length of the fiber L, hence so at some point SRS will set a fundamental limit to the achievable power of the system. Second, Stokes wave needs an initial intensity $I_s(0)$ in order to grow up. If there is no signal in Stokes frequency, it will grow from the quantum fluctuations in the cavity. Assuming a single photon in each mode of the cavity, the following relation can be obtained [31]:

$$\frac{g_R P_{cr} L}{A_{eff}} \cong 16 \tag{2.8.3}$$

Here P_{cr} is the critical incident pump power where the Raman threshold is reached and defined as the power at which the Stokes power becomes equal to the pump power at the fiber output.

Stimulated Brillouin scattering (SBS) is similar to SRS. It is also related to the third-order susceptibility $\chi^{(3)}$ and can be effective at very low powers if the conditions are suitable. SBS is basically conversion of an incident photon to a scattered photon with slightly lower energy and an acoustic phonon. Due to the phase-matching requirements, the scattered photon travels in the opposite direction of the incident photon. The frequency difference between the incident and scattered photons, which is also called the Brillouin shift is given by $\nu_B = 2n v_a/\lambda$ where n is the effective index of the fiber, λ is the wavelength of the incident photon, and v_a is the velocity of acoustic phonons. For silica, this is on the order of 10 GHz with a bandwidth of 10 MHz. It is also possible to write an equation for the Brillouin threshold [31] similar to Eq. 4.4.2,

$$\frac{g_B P_{cr} L}{A_{eff}} \cong 21, \tag{2.8.4}$$

where g_B is the Brillouin gain with a peak value of 5×10^{-11} m/V. This is a relatively larger value compared to the Raman gain indicating a smaller onset time for SBS. However, because of its small bandwidth, SBS can only be effective for very narrow-spectrum pulses like the ones form a single-frequency laser. For pulses shorter than 10 ns, SBS is negligible. Also, there are some techniques to suppress the SBS. Since it is sensitively dependent on the phonon velocity, nonuniform heating of the fiber throughout its length will help by changing the phonon velocity. Actually, in an amplifier this is the

case; the entrance of the fiber where the pump light is injected has significantly higher temperature than the output end.

Bulk material damage threshold of silica is one of the important parameters to keep in mind while designing a high power fiber laser. In literature, one can find many values for this threshold. Also, pulse duration and doping level have effects on this value, which makes things more complex. In general, it is safe to assume a value of 100 GW/cm^2 for a 1 ns-long pulse, which is inversely proportional to the square root of the pulse duration. For CW operation, the damage threshold approaches to 10 GW/cm^2. For doped fibers half of these values should be used.

Surface damage threshold of silica is much smaller than the bulk damage threshold. Again, there is no agreement about its value however taking it as five times smaller than the bulk damage threshold is a reasonable estimate. This means that the fiber ends are much more sensitive to optical damage than the bulk fiber itself. In high power designs, it is customary to use end-caps in order to increase this threshold level.

Self-focusing is a phenomena occurring at extremely high powers. The guided light focuses onto itself because of the index profile created by the intense electric field. The critical power can be estimated from

$$P_{cr} \cong \frac{0.15\lambda^2}{n_0 n_2}, \tag{2.8.5}$$

where n_0 is the refractive index and n_2 is the nonlinearity coefficient. For silica, the critical power for self-focusing is around 4.5 MW at 1 μm wavelength.

Core fusing (or fiber fusing) is a catastrophic damage induced by a defect point, which can occur at power levels as low as few watts. This defect point can be inside the core as well as a dust particle at the tip of a fiber. At this point, a hot plasma forms and travels in the backward direction with a relatively slow speed (~1 m/s), even detectable by eye. It is especially dangerous in telecommunication systems where kilometers of fiber may be destroyed by this process. It is also important for the high power systems since it is an unpredictable event, which may damage the other parts of the system.

Thermal damage of the coating is another important factor. Since the melting temperature of silica is very high (1700 ºC), the most sensitive part to thermal loads in a fiber laser system is the coating of fibers. In general, a double-clad fiber is coated with a low-index fluorinated acrylic polymer in order to form the second cladding. Although its optical properties are excellent, thermal properties of an acrylic coating is rather poor. It can be damaged at temperatures as low as 150-200 ºC and the suggested operation temperature is 80 ºC. Furthermore, it has a low thermal conductivity, which is around 0.24 $WK^{-1}m^{-1}$. Even if the outside of the acrylic coating can be hold below 30 ºC by an aggressive cooling, the temperature at the silica-acrylic interface (which is the most critical place) can be much higher. This temperature difference can be approximated by

$$\Delta T \cong \frac{Qd}{2\pi r k}, \tag{2.8.6}$$

where Q is the thermal loading, d is the coating thickness, r is the radius of silica-acrylic interface and k is the conductivity of the coating. For a Liekki 25/250DC fiber, the temperature difference is 50 ºC for a thermal loading of 200 W/m.

Finally, photodarkening is the increase of optical losses by formation of color centers. Although the absorption occurs mainly in the visible region, its extension into the infrared

region may severely drop the performance of fiber lasers operating in the 1-2 μm band. The formation of color centers becomes easier in the presence of large diameter atoms (like rare-earth atoms such as Yb) and their number rapidly increases by the collaborative action of excited Yb ions. As a result, lowering the doping level is an efficient way to reduce photodarkening rate. Co-doping with certain ions like phosphorus also helps. Photodarkening is a reversible process that can be cured by annealing the fiber at ~300 ºC but the coating will be destroyed during this process.

2.9. Material Processing with Lasers

High power lasers have been used in material processing for a long time since 1960s [43]. They have significant advantages over conventional processing techniques. First of all, the non-contact nature of laser processing eliminates tool wearing which is one of the primary expenditures in mechanical processing. Second, no chemicals (like solvents, lubricants, etc.) are used in the process so it is environmentally clean. Third, by adjusting the wavelength or intensity, selective material removal is possible without damaging the under layer. Also, laser processing is extremely flexible with computer controlling and good for prototyping. The first and most widely used lasers in industry are CO_2 [44], Nd:YAG [45], direct-diode [46], and excimer [47] lasers. Ti:sapphire [48] lasers, being the primary source of femtosecond pulses, remain as laboratory tools due to their high price and limited robustness. Nowadays, new kinds of solid state (primarily fiber and thin-disk) lasers are increasingly replacing these conventional lasers because of their various advantages such as better beam quality, power scalability and efficiency.

The main application areas of lasers in machining are cutting, drilling, welding, surface treatment, bending, forming, cleaning, rapid prototyping, the details of which can be found

in various textbooks on the subject [43, 49]. Especially, for micromachining applications where extremely high precision is required, short-pulsed lasers are utilized. There are numerous examples of precision machining in the literature. For example, surface texturing is one of the main application areas. By treating the surface with a pulsed laser, one can control surface reflectivity, obtain hydrophobic surfaces, create nanograting structures, etc. Pulsed lasers are also used in production of micro structures like microelectromechanical systems (MEMS), microfluidic channels and in lithography (especially in photovoltaics for scribing). Laser drilling is especially important for production of high-quality, ultra-narrow nozzles, which is extremely difficult to produce by mechanical means. These are used in many areas like ink-jet nozzles or cooling holes on turbine blades. Femtosecond lasers can also be used in micromachining of transparent media like glass. Since light is absorbed by a multi-photon process in this regime, it is possible to directly modify the focal region inside the glass without damaging the surface. Fiber Bragg gratings (FBG) written directly in fiber cores or waveguides written into various glasses can be produced by this method. In chemical or media assisted processing, 3D structures can be formed again by using intensity dependent absorption. Pulsed lasers are also good for processing brittle materials since they do not create excessive thermal loads. More detailed information can be found in textbooks or review type papers [43, 49, 50, 51].

The most common laser-matter interaction model used in academic literature is a simple, one-dimensional heat flow model, schematic of which can be seen in Fig. 2.9.1. Here, heat flow is assumed to occur only in z-direction, assuming that the spot radius is much larger than the heat penetration depth.

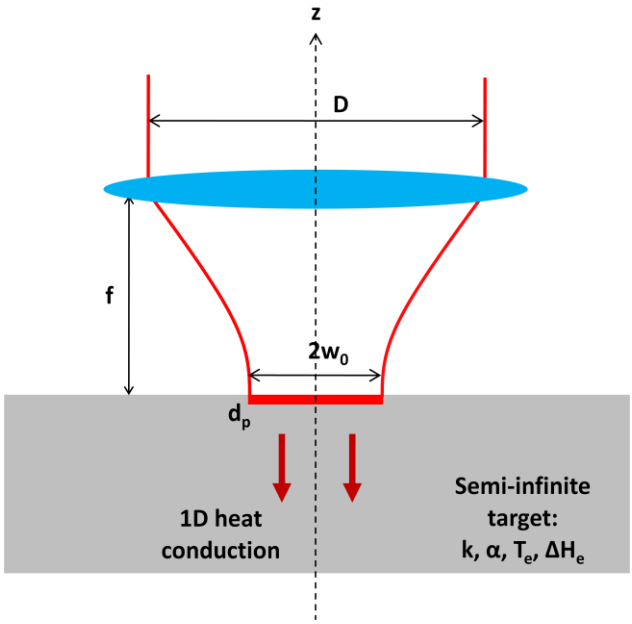

Fig 2.9.1. Schematic of the laser-matter interaction model commonly used in literature.

The important parameters involved in material processing can be divided in two subgroups; beam parameters and material properties. Beam parameters include spatial and temporal intensity profiles, beam quality, spot size, and depth of focus (DOF). Spatial intensity profile of a beam delivered from a single mode fiber was turned out to be a Gaussian function given by Eq. 1.3.17 which is generally approximated by a flattop profile for practical reasons. Temporal profile has a large range from continuous-wave operation to femtosecond pulses with hundreds of MHz repetition rate. Generally, the collimated beam coming from the laser-amplifier system is directed to the target by a galvo-scanner composed of two controllable mirrors and focused by an f-theta lens (the focal point of which always remains on a plane). When a collimated beam with a diameter D is focused by a lens of focal length f, a waist will form according to

$$w(z) = w_0 \sqrt{1 + \left[\frac{M^2 \lambda (z - z_0)}{\pi w_0}\right]^2}, \tag{2.9.1}$$

where $w(z)$ is the beam radius at a distance z from the focal plane, w_0 is the waist radius, λ is the wavelength of the beam, z_0 is the location of focal plane, and M^2 is a measure of beam quality which approaches to unity for a perfect Gaussian beam. For this condition, the spot-size $(2w_0)$ is given by $4\lambda f/\pi D$, and the depth of focus (DOF, the length for which beam diameter remains smaller than $\sqrt{2}$ times the spot size) is given by $8\lambda f^2/\pi D^2$.

The material properties include surface reflectivity, thermal conductivity and diffusivity, evaporation temperature, and heat of evaporation. The surface reflectivity has a strong dependency on the wavelength. At 1 μm wavelength, its value is greater than 0.9 for many metals like Al, Cu, etc. However, this value decreases with temperature. For example, at 1000 K, reflectivity of steel, Al, and Cu is around 0.7. Thermal conductivity and diffusivity are also important since the local temperature in a poor thermal conductor (like steel) can reach much higher values compared to a good thermal conductor (like Al, Cu). Also, it is easier to remove material from the surface if the evaporation temperature and heat of evaporation are low.

When light strikes a metallic surface, the first processes occurring include the reflection. Along with losing much of its energy due to reflection, light is rapidly absorbed by the material. For metals, typical optical penetration depth is around 10 nm at 1 μm wavelength. Light is mainly absorbed by the conduction band electrons, which subsequently transfer their energy to the lattice within few picoseconds through excitation of phonons. This time scale is also referred to as thermalization time. For ultrashort pulses comparable to thermalization time, it is customary to use a two-temperature model [52] where the heating of conduction band electrons and lattice are defined separately. Since the conductivity of

electrons is much larger than the lattice, the heat conduction in the lattice is generally ignored. This regime is valid until the electron and lattice temperatures equalize due to electron-phonon scatterings. For pulses longer than 10 ps, the two-temperature model can be reduced to the following simple form [53], where heating of conduction band electrons can be completely ignored by assuming that the light is directly heating up the lattice:

$$\frac{\partial T}{dt} = \alpha \frac{\partial^2 T}{\partial z^2} + \frac{1-R}{\rho c_p d_p} I(r,t) e^{-z/d_p}, \tag{2.9.2}$$

where R is the reflectivity, α is the thermal diffusivity, ρ is the density, c_p is the heat capacity, and d_p is the optical penetration depth. Here, $I(r,t)$ describes both the spatial and temporal beam profile which is equal to a constant value of I_0 for a rectangular pulse both in space and time domains. For this case, the temperature distribution is given by [53]

$$T(z,t) = I_0 \frac{(1-R)\sqrt{4\alpha t}}{k} \mathrm{Ierfc}\left[\frac{z}{\sqrt{4\alpha t}}\right], \tag{2.9.3}$$

where Ierfc$[x]$ is the integrated complementary error function. If the maximum temperature does not exceed the melting temperature, heat is simply dissipated through conduction. However, there can still be some phase changes occurring inside the material due to the high temperatures, and this region is called as heat-affected-zone (HAZ). If temperature is in between evaporation and melting temperatures, a liquid pool forms on the surface, which solidifies immediately after the pulse but alters the material properties like grain size, hardness, etc. If temperature exceeds evaporation temperature, the material removal from the surface starts. This can occur through direct evaporation/sublimation or liquid ejection by the pressure of the vapor phase. If temperature is even higher, a plasma phase may form. At this stage, the physical properties of plasma gain importance. The ejected plasma plume absorbs some portion of the pulse energy resulting in a shielding effect. If this process

occurs close to the surface, the plasma may transfer the absorbed energy to the surface through conduction. However, if plasma is separated well enough from the surface, it effectively shields the beam leading a significant decrease in material removal rate.

Note that, if the photon energy is high enough or the intensity is high enough for multi-photon absorption, chemical or optical breakdown may occur at the absorption layer and the material can be directly ablated from the surface. Moreover, if the pulse duration is comparable with the thermalization time, the ablated material cannot find enough time to transfer its energy as heat into the bulk material before removing from the surface. This leads material removal with significantly small HAZ, which is an important regime for extremely precise applications.

Chapter 3

All-Fiber Low-Noise High-Power Femtosecond Yb-Fiber Laser Amplifier System

3.1. Introduction

In this chapter, we present an all-fiber, high-power, low-noise amplifier system seeded by an all-normal-dispersion laser. To our knowledge, this work is the first high-power source of femtosecond pulses with completely fiber-integrated amplification stage comprising commercially available components. Note that the most of the results presented in this chapter were published in [54] (copyright © 2009, IEEE). In this study, the oscillator and preamplifier were mainly built by the author, the power amplifier was mainly built by Pranab Mukhopadhyay, and the noise measurements were conducted by Levent Budunoğlu.

As stated before, there is strong interest in literature for developing high power fiber lasers. An important branch of them is the ultrafast fiber lasers, which provide high-power femtosecond pulses. In addition to well-known application areas like nonlinear optics, metrology and spectroscopy, numerous applications have been reported where the ultrafast laser serves as an advanced tool for material processing or imaging with sub-diffraction-limit precision and greatly reduced or absent heat effects. These applications range from

precision micromachining [55] and pulsed-laser deposition [56] to biomedical imaging [57], tissue processing [58] and even nanosurgery [59]. While it is clear that these emerging applications hold potential for major scientific and industrial impact, progress is hampered due to a lack of compact, low cost, simple-to-operate, and robust laser sources. All-fiber lasers can potentially address all of these requirements.

Much progress has been made in recent years in terms of scaling up the power output of high-repetition-rate Yb-doped fiber amplifiers using self-similar amplification [60, 61], as well as chirped-pulse amplification [62] and large-mode-area fibers (LMA) [63]. Limpert *et al.* [64] have demonstrated 76 W of average power at 75 MHz repetition rate with 400 fs pulse duration, and subsequently, Röser *et al.* [65] demonstrated average power in excess of 130 W with 220 fs pulse duration. Impressive performance in terms of pulse energy has also been demonstrated up to the 1 mJ level at 100 kHz repetition rate [66]. In terms of pulse duration, 70 fs duration and 10.6 W of average power have also been obtained through the use of custom fibers and fiber-Bragg gratings for higher-order dispersion control [67]. However, these systems employ discrete optical components for coupling of the pump and signal beam to the gain fiber, and in several of the cases, a bulk solid-state oscillator to seed the amplifier, along with bulk grating stretchers. Much of the system is actually not fiber. This counters some of the main advantages of fiber. For instance, slight misalignment of the pump coupling easily leads to fiber facet damage during operation at high powers. All-fiber amplification of pulses directly from mode-locked fiber lasers has been demonstrated [68], but the results were limited to low powers due to unavailability of high pump powers.

With the development of MPCs, single-mode signal fiber as well as several multimode pump fibers from high-power laser diodes can be delivered to the core and cladding regions

of a double-clad (DC) fiber, respectively [69]. The DC fiber can be fusion-spliced to a matching doped fiber. This approach eliminates possibility of pump misalignment.

The work presented in this chapter, to the best of our knowledge, the first demonstration of an all-fiber amplifier at 10.6 W power level with completely in-fiber delivery of the pump. The laser system is constructed using commercially available components only, and as such, it can easily be duplicated. The amplifier is seeded, also for the first time to our knowledge, by a compact all normal-dispersion (ANDi) Yb-doped mode-locked oscillator [25]. Pulses are compressed to sub-160-fs duration using an external grating pair. We achieved diffraction-limited beam quality ($M^2 < 1.1$) and intensity noise of ~0.2% (measured over 20 Hz to 250 kHz) at 10.6 W.

An all-fiber amplifier is most naturally seeded by a fiber oscillator directly from an intracavity fiber coupler [68]. As it was stated before, there are several mode-locking regimes. Among these, the ANDi laser does not require the use of diffraction gratings and has the potential for all-fiber integration. Owing to its simplicity and robustness, we have adapted an ANDi laser as the seed source in this study. Record-high pulse energies have been obtained from such lasers [70, 71]. On the other hand, these lasers produce relatively long pulses with residual nonlinear chirp. It was not clear to us *a priori* whether seeding a strongly nonlinear amplifier with such pulses would not compromise the amplified pulse quality. As such, extensive numerical simulations were performed to understand the pulse shaping and guide the experiments.

3.2. Experimental Setup

The experimental setup is shown schematically in Fig. 3.2.1. The system consists of the following parts: an ANDi-type Yb-doped fiber oscillator connected to a fiber pulse-

stretcher followed by a preamplifier and a power amplifier. Finally, the amplified pulses are compressed in a grating compressor, which is not shown in the figure.

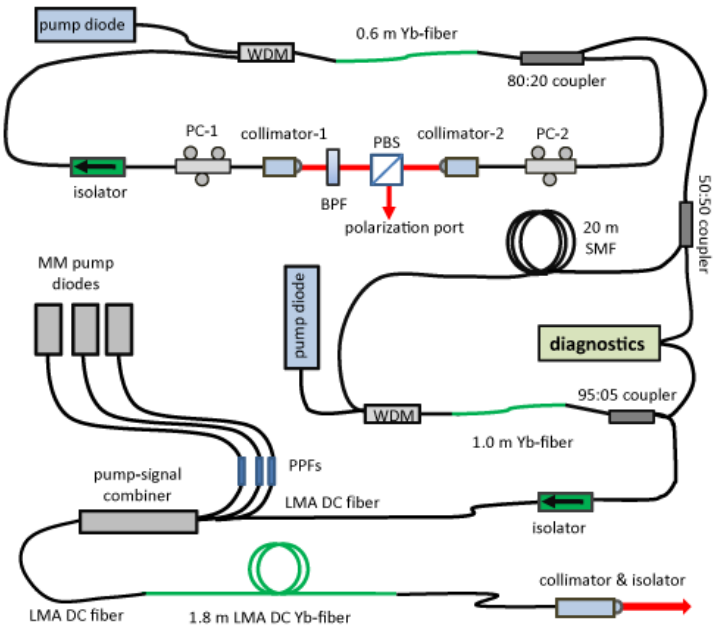

Fig. 3.2.1. Schematic of the laser setup: BPF: band-pass filter, PBS: polarizing beam splitter cube, PC: polarization controller, LMA: large-mode-area fiber, DC: double-clad fiber, SMF: single-mode fiber, PPFs: pump protection filters, WDM: wavelength-division multiplexer.

The oscillator comprises 2.1 m of standard single-mode fiber (SMF) for 1 μm wavelength (core diameter of 6.2 μm, 0.14NA) and 0.6 m of highly Yb-doped gain fiber (core diameter of 6.2 μm, 0.14NA, ~500 dB/m absorption at 976 nm), followed by another 1.7 m of SMF. The gain fiber is pumped in-core by a fiber-coupled laser diode operating at 976 nm with a maximum output power of 300 mW. Total group velocity dispersion (GVD) of the cavity is ~0.1 ps^2. Fast saturable absorption required for mode-locking is obtained from nonlinear

polarization evolution (NPE), which is implemented with two in-fiber polarization controllers and a polarizing beam splitter cube. An interference filter with a bandwidth of 10 nm is placed right after the polarizer. Due to the heavy chirp on the pulse, the influence of filter in the time domain is to remove the temporal wings of the pulse, and assist the saturable absorber. The transmission peak, centered at 1060 nm, sets the central wavelength of the pulses [72]. An optical isolator is placed for unidirectional ring cavity configuration. Mode-locked operation is self-starting and appears to be stable indefinitely.

An output power of 26 mW at 43 MHz repetition rate is obtained directly through a 20% output coupler after the gain fiber. Direct fiber coupling of the seed pulses to the amplifier completely eliminates the possibility of interruption of the seed due to misalignment or accidental blocking of the beam path. We found that the power from the seed laser is sufficient to suppress the amplified spontaneous emission (ASE) in the subsequent amplifying stages due to the gain peak at 1030 nm. Around 50% of the output power from the oscillator traverses a 20-m-long SMF section to stretch the pulses. The rest is used for monitoring purposes. Inclusion of an in-line preamplifier relaxes the power requirements from the oscillator, allowing it to be operated at moderate power levels, where its long-term operation is most stable. The pulses from the oscillator are amplified to an average power of ~100 mW in the preamplifier stage consisting of a 1-m-long Yb-doped fiber (of the same type as in the oscillator) pumped in-core by a 976 nm laser diode. The power amplifier is in forward pumping configuration in order to protect the pump diodes from optical damage due to leakage of the high-peak-power signal to the pump ports. Pump delivery to the gain fiber is accomplished with a 6 port MPC incorporating a single-mode signal feed through. The signal port of the MPC is an LMA fiber (core diameter of 20 μm, 0.07NA), whereas the output of the isolator is standard SMF, resulting in a lossy, but mechanically strong splice. Due to the combined loss of the isolator (~50%) and the splice, only 25 mW of signal power is coupled to the output fiber of the MPC, which is an undoped DC LMA

fiber with 20 μm core diameter (0.07NA), 123 μm inner cladding diameter (0.46NA) and 250 μm outer cladding with an octagonal structure (made of low-index acrylic polymer). We used three 975 nm diodes with 8 W of maximum power coupled to 105 μm core diameter multimode fibers as pump for the power amplifier. Unused pump ports are utilized for monitoring the backward propagating signal. It is essential to use pump protection filters (PPF) that transmit the pump wavelength around 975 nm but block wavelengths above 1020 nm to protect the diodes from optical damage due to the feedback from the amplified signal or spontaneous emission. We measured that 85% of the pump power is coupled to the MPC. The high-power amplifier comprises a 1.8 m-long Yb-doped DC LMA fiber, which has similar specifications with the output fiber of MPC. The ytterbium doping concentration is 8.5×10^{25} m^{-3}. The V-parameter of the fiber is 4.15 so it was coiled to ~10 cm diameter to avoid the excitation of higher order spatial modes. The gain fiber is spliced with the output fiber from the MPC. The stripped off outer cladding is recoated using a low-index polymer for uninterrupted guiding of the pump beam through the splice region. The other end of the gain fiber is spliced to a non-DC LMA fiber to gently strip off any unabsorbed pump light. Finally, the output is taken through an in-fiber isolator-collimator with a transmission of 90%. The isolator helps prevent the reflected beam from coupling back into the laser system, e.g., during material processing. For some applications, an isolator is not required.

.

3.3. Numerical Simulation Software

In this section, we introduce the numerical simulation software developed previously in our group. It is mainly based on solving NLSE by the *split-step Fourier method* and includes the effects of second and third-order dispersion, saturable gain, linear losses and nonlinear effects such as gain dispersion in the amplification section, self-phase modulation, Raman

scattering, saturable absorption and band-pass filter. The pulse is assumed to start from noise (or Gaussian profile) and is iterated over many roundtrips until a steady state solution is achieved. NLSE containing all of these effects can be written by combining Eq. 2.1.31 with Eq. 2.2.3 as

$$\frac{\partial a}{\partial z} + \frac{i(\beta_2 + ig\tau_2^2)}{2}\frac{\partial^2 a}{\partial \tau^2} - \frac{\beta_3}{6}\frac{\partial^3 a}{\partial \tau^3} + \frac{\alpha - g}{2}a$$

$$= i\gamma\left[|a|^2 a + \frac{i}{\omega_0}\frac{\partial}{\partial \tau}(|a|^2 a) - T_R a\frac{\partial |a|^2}{\partial \tau}\right], \tag{3.3.1}$$

which can be written in a more compact way by using two newly defined operators;

$$\frac{\partial a}{\partial z} = (\widehat{D} + \widehat{N})a, \tag{3.3.2}$$

where the differential operator $\widehat{D}$ governing the linear dispersion and absorption terms and the nonlinear operator $\widehat{N}$ governing all nonlinear effects on pulse propagation are given by

$$\widehat{D} = -\frac{i(\beta_2 + ig\tau_2^2)}{2}\frac{\partial^2}{\partial \tau^2} + \frac{\beta_3}{6}\frac{\partial^3}{\partial \tau^3} - \frac{\alpha - g}{2} \tag{3.3.3}$$

$$\widehat{N} = i\gamma\left[|a|^2 + \frac{i}{\omega_0}\frac{1}{a}\frac{\partial}{\partial \tau}(|a|^2 a) - T_R\frac{\partial |a|^2}{\partial \tau}\right]. \tag{3.3.4}$$

Now, suppose that the fiber is divided into small segments of thickness h. The split-step Fourier method obtains an approximate solution by assuming that propagation over distance h is carried out in three steps. First, the pulse propagates over half the distance

with only dispersive effects. Then, in the middle of the section, nonlinearity is included after which the pulse propagates again half the distance (Fig. 3.3.1). Mathematically,

$$a(z+h,\tau) \cong \exp\left(\frac{h}{2}\widehat{D}\right)\exp\left(h\widehat{N}\right)\exp\left(\frac{h}{2}\widehat{D}\right)a(z,\tau). \tag{3.3.5}$$

The terms with $\widehat{D}$ can be evaluated in Fourier domain much more easily:

$$\exp\left(\frac{h}{2}\widehat{D}\right)a(z,\tau) = F_T^{-1}\exp\left(\frac{h}{2}\widehat{D}(i\omega)\right)F_T a(z,\tau), \tag{3.3.6}$$

where F_T denotes the Fourier transform operation. Since $\widehat{D}(i\omega)$ is just a number in the Fourier space, the evaluation of Eq. 3.3.5 is straightforward. This is why the split-step Fourier method is order of magnitude faster than methods like finite difference [31].

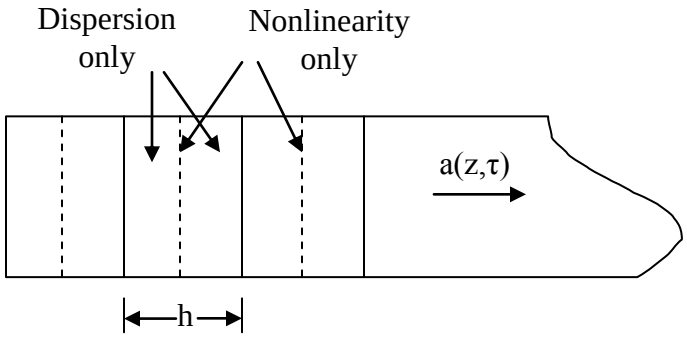

Figure 3.3.1. Illustration of split-step Fourier method used for numerical simulations.

A screenshot of the simulator interface is shown in Fig. 3.3.2. The parameters to be entered into the simulator are listed in Table 3.3.1. The initial pulse shape can be one of the pre-defined pulse shapes ranging from Gaussian pulse shape to noise. Each segment of the laser should be configured separately. The saturable absorber (SA) is implemented at the end of

a segment, by converting the total nonlinear phase shift accumulated over the round trip into an amplitude modulation. The semiconductor and NPE saturable absorbers are modeled in the simulation as

$$\frac{I'_{SC}}{I} = 1 - q\left(1 + \frac{I}{I_{sat}}\right)^{-1}, \tag{3.3.7}$$

$$\frac{I'_{NPE}}{I} = 1 - q\cos^2\left(\frac{\pi}{2}\frac{I}{I_{sat}}\right), \tag{3.3.8}$$

where I and I' are the intensities before and after SA, q is the modulation depth and I_{sat} is the saturation intensity of the SA. Gain saturation is also taken into account as

$$g(E) = \frac{g_{ss}}{1 + \frac{1}{E_{sat}}\int |a|^2 \mathrm{d}\tau}. \tag{3.3.9}$$

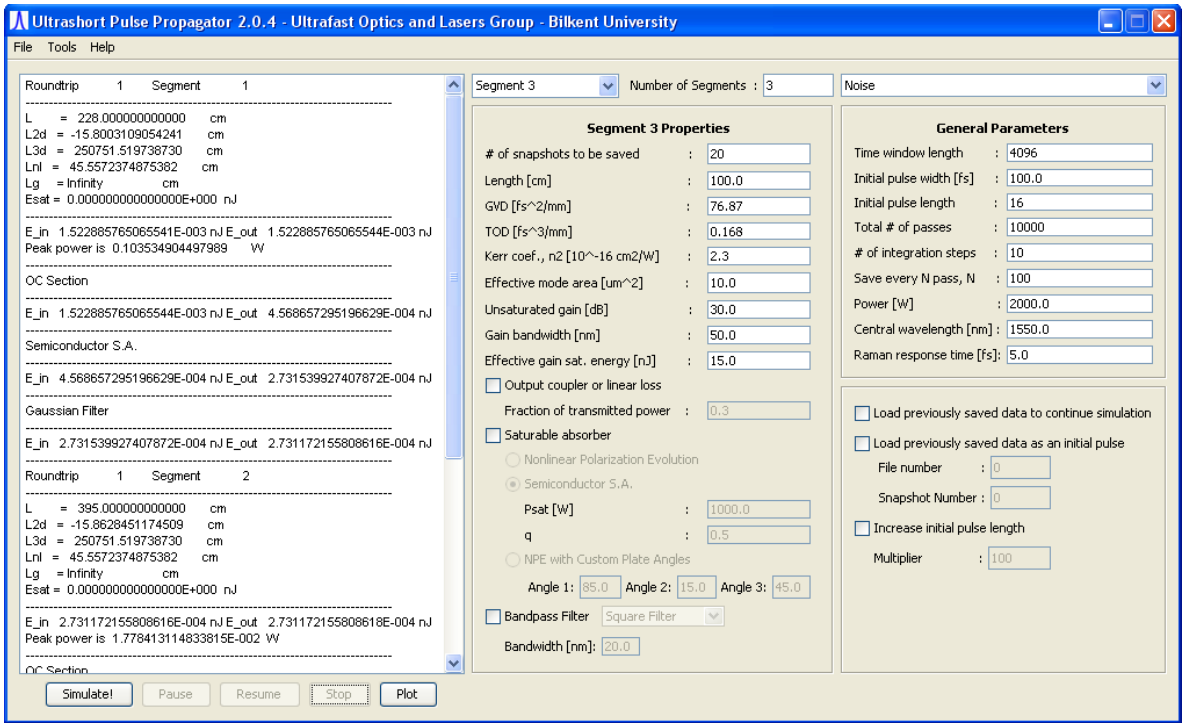

Figure 3.3.2. A screenshot of the simulator interface.

Parameter	Function
Time window length	Number of data points for discretizing time
Initial pulse width [fs]	Actual length of the pulse corresponding to a # of data points
Initial pulse length	# of discrete points representing the FWHM of initial pulse
Total # of passes	# of passes to be made over the entire sequence of segments
# of integration steps	# of discrete steps taken per each page per segment
Save every N pass, N	# of roundtrips after which data is saved to file
Power [W]	Actual power corresponding to unit size of power
Central wavelength [nm]	The central wavelength of the light used for simulation
Raman response time [fs]	Parameter characterizing the strength of the Raman effect

# of snapshots to be saved	# of segments each fiber section is divided into
Length [cm]	Physical length of the segment
GVD [fs^2/mm]	Second order dispersion parameter
TOD [fs^3/mm]	Third order dispersion parameter
Kerr coef., n_2 [10^{-16}cm2/W]	The Kerr nonlinearity coefficient
Effective mode area [μm^2]	Effective mode area for the propagating beam
Unsaturated gain [dB]	Small signal gain of the amplifier
Gain bandwidth [nm]	Finite gain bandwidth for parabolic approximation
Effective gain sat. energy	Saturation energy in arbitrary units for the gain
Output coupler/linear loss	Adds an output coupler to the end of the segment

Table 3.3.1. Numerical parameters needed for the simulator.

3.4. Results & Simulations

Numerical simulations are employed to study the pulse dynamics throughout the system, starting with pulse generation in the oscillator, followed by propagation through the fiber stretcher, preamplifier, power amplifier and grating compressor (Fig. 3.2.1). We run separate simulations for pulse generation in the oscillator and pulse propagation outside the oscillator. The numerical output of oscillator simulation serves as the initial condition for propagation through the fiber stretcher, the preamplifier, the power amplifier, and the grating compressor.

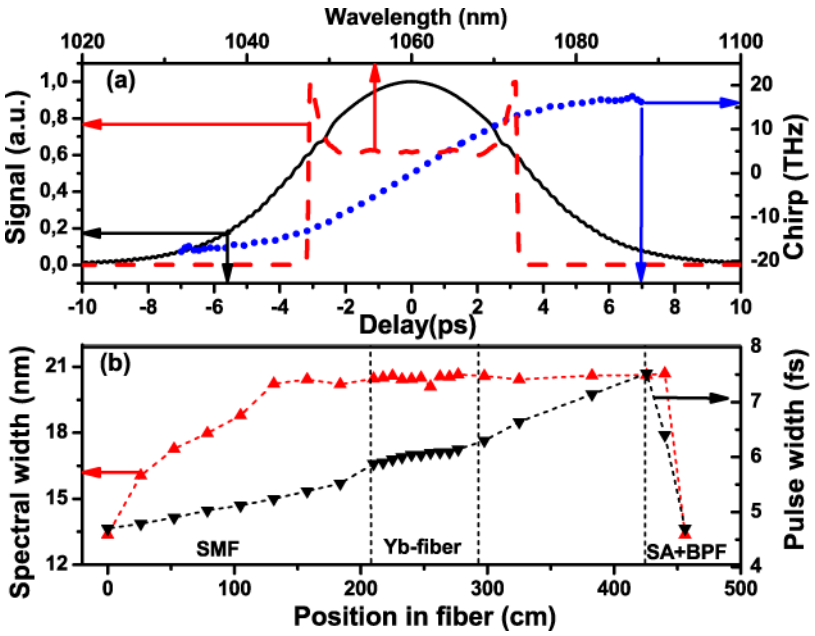

Fig. 3.4.1. Numerical simulation results for the oscillator: (a) Pulse characteristics at the 20% output port, showing the temporal shape (black, solid line), the spectrum (red, dashed line), and temporal chirp (blue, dotted line). (b) Variation of the spectral (red, upward triangles) and temporal (black, downward triangles) width (FWHM) along the length of the cavity (referenced to collimator-1). Lines are to only guide the eye.

The following parameters used for the oscillator fiber segments: $\beta_2 = 23$ fs^2/mm, $\beta_3 = 41$ fs^3/mm, $n_2 = 2.3 \times 10^{-16}$ cm^2/W. The effective mode area for the SMF and gain fiber was 30 μm^2 and 22 μm^2 respectively. The fiber is followed by a lumped saturable absorber that represents NPE and a Gaussian-shaped band-pass filter with 10 nm bandwidth (both of which are modeled as transfer functions, in time and frequency domains, respectively). The initial field is white noise. Simulations are run until the field converges within a finite number of round trips through the cavity. We verify numerical accuracy by checking that the results are unchanged after doubling each of the sampling

resolutions. In Fig. 3.4.1(a) and (b) we summarize the simulation results for the oscillator with total cavity GVD of $0.1\ \mathrm{ps}^2$, $E_{sat} = 1.8\ \mathrm{nJ}$, and $g_0 = 30\ \mathrm{dB}$. The lengths and positioning of the fibers are as used in the experiments. The combined action of gain, nonlinearity, normal dispersion, and spectral filtering leads to linearly chirped optical pulses with a spectral profile that develops the steep and structured edges characteristic of self-phase modulation (SPM). Starting at the location of collimator-1, the full-width at half-maximum (FWHM) temporal and spectral widths of the pulse both increase monotonically in the SMF section (Fig. 3.4.1(b)). In the gain fiber and the second SMF section, the spectral width remains nearly constant owing to gain narrowing in the Yb-fiber and increased pulse duration in the second SMF section, but the pulse duration continues to increase due to GVD. We find that NPE has relatively little effect, compared to the spectral filter terms of their effect on the temporal and spectral widths. These findings are in agreement with those of references [25], [70].

As shown in Fig. 3.4.2(a), though the spectrum is highly structured, the corresponding temporal profile is a smooth, positively chirped Gaussian with 7 ps FWHM width at the fiber-coupled output of the oscillator (taken as input for the propagation simulations). The width of the chirped pulses from the polarization port inferred from autocorrelation measurements agree very well with the numerical results. The simulated and measured spectra for the oscillator output match very closely. The bandwidth is ~22 nm, corresponding to a transform-limited pulse width of 132 fs.

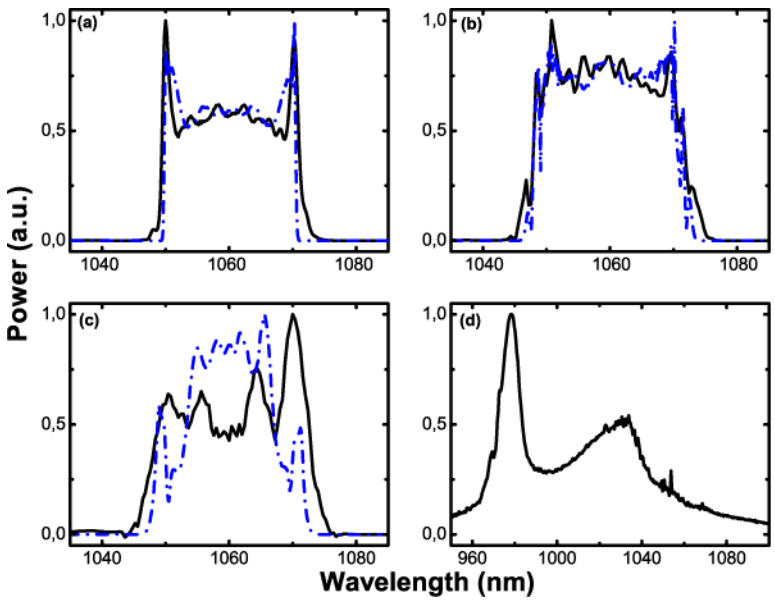

Fig. 3.4.2. Measured (solid, black lines) and simulated (dash-dotted, blue lines) spectra obtained from: (a) oscillator output, (b) preamplifier output, (c) amplifier output (at 10.6 W of power), (d) an unused pump port (showing backward propagating ASE signal and residual pump power).

The pulses from the oscillator are stretched in a 20-m-long SMF section. Based on the numerical simulations, the pulse duration increases to ~18 ps after the fiber stretcher. The stretched pulses are amplified in a 1-m-long single-mode Yb-fiber. The measured and simulated spectra of the pulses after the preamplifier are shown in Fig. 3.4.2(b). The spectral width is increased slightly to 23.5 nm and some oscillations develop at the edges of the spectrum due to nonlinearity. There is no significant ASE signal at the gain peak of 1030 nm, nor a Raman-shifted signal at longer wavelengths. For the simulations, we adjust the saturation energy of the gain fiber to obtain the same amplification factor as in the experiment. Pulse propagation through the power amplifier is simulated in the same manner, with the effective mode area of the gain fiber set to 314 μm^2 and the length of 1.8

m. The gain in the simulations is adjusted to obtain the same amplification factor of the pulse energy for the corresponding pump power in the experiments. The main features of the simulated and experimental spectra match very well at low powers. Fig. 3.4.2(c) shows results at 10.6 W, where the agreement is still reasonable. At 10.6 W of average power, the pulse energy is ~230 nJ and the peak power is estimated to be 13 kW. Some oscillations develop on the spectrum only at high powers, which we attribute to polarization beating. In addition, the oscillations are accompanied by quick variation of the polarization state with pump power. This can be avoided with a polarization-maintaining fiber system. Fig. 3.4.2(d) shows a spectrum recorded from an unused pump port of the MPC, showing a small amount of (few mW) backward-propagating ASE and residual pump light. The backward-propagating light contains a small fraction of the pulses as well. For this reason, protection of the pump diodes is essential. In order to better understand the power scaling characteristics and ASE production in the power amplifier, we used a model similar to the one explained in Section 6.3. The following values are used in the model: 20 μm core diameter; 125 μm cladding diameter; 1.8-m-long gain fiber; $N_{tot} = 8.5 \times 10^{25}$ m^{-3}; $\sigma_{ap} = 25 \times 10^{-13}$ μm^2, $\sigma_{ep} = 21.7 \times 10^{-13}$ μm^2, $\sigma_{as} = 0.448 \times 10^{-13}$ μm^2, $\sigma_{es} = 2.62 \times 10^{-13}$ μm^2 and $\tau_1 = 0.8$ ms.

Experimentally measured and calculated signal power dependences on pump power are shown in Fig. 3.4.3. At a total coupled pump power of 20 W, we measure 10.6 W at the isolator-collimator port, corresponding to 53% optical conversion efficiency.

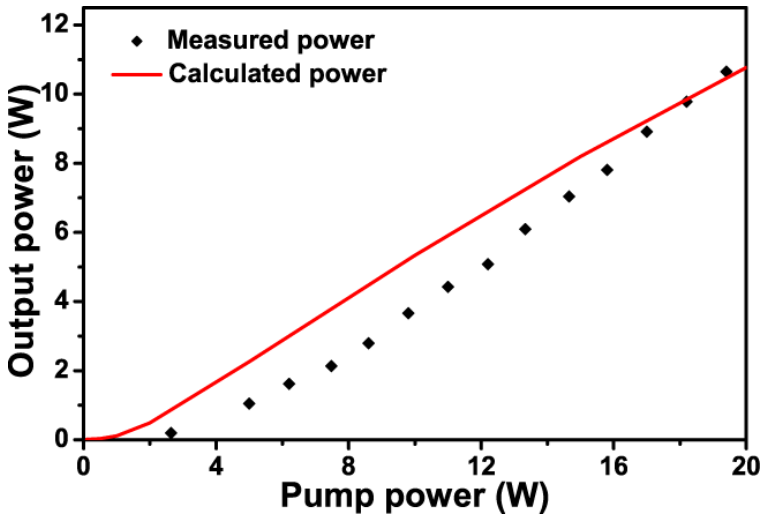

Fig. 3.4.3. Power scaling characteristics of the power amplifier. Points represent measured output power versus total pump power. Solid line shows the simulation results.

We attribute deviation of the measured values from calculations at lower pump powers to a shift of the diode emission wavelength. At low pump powers, the peak emission wavelength from the diodes is around 955–960 nm, which is far away from the peak absorption wavelength (~976 nm) of an Yb-doped fiber. This can be compensated by increasing the diode temperature, which was avoided not to strain the diodes. As the diode drive current is increased, the emission wavelength shifts toward 976 nm. Chirped pulses from the power amplifier are compressed to near-transform limit in a grating pair, which is in near-Littrow configuration, and characterized with short-span interferometric and long-span intensity autocorreletions. The overall efficiency of the current grating compressor is around 50%. However, efficiencies as much as 80% are readily available with higher quality gratings.

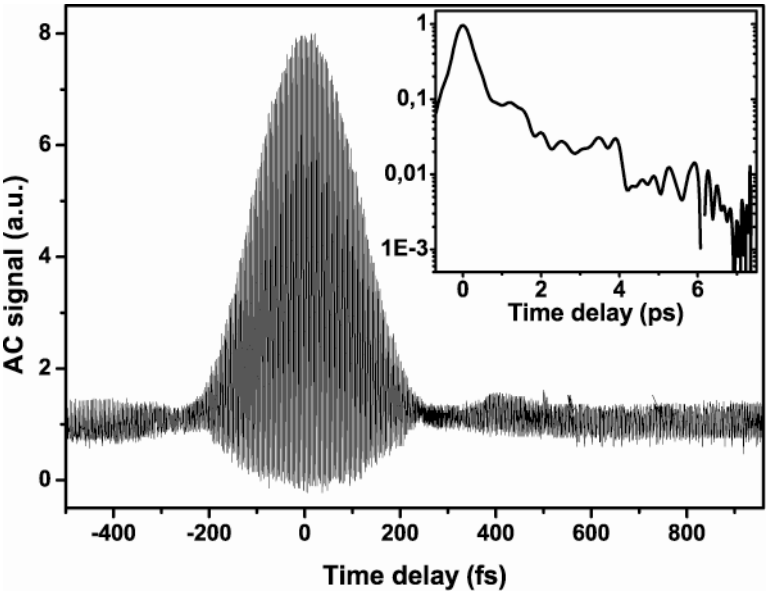

Fig. 3.4.4. Interferometric autocorrelation trace of dechirped pulses at 10.6 W of power. Inset shows long-range intensity autocorrelation on semi-log scale.

An interferometric autocorrelation (AC) trace of the dechirped pulses corresponding to 10.6 W of average power is shown in Fig. 3.4.4. The FWHM width of the AC is 240 fs, which corresponds to an estimated pulse duration of ~160 fs (assuming a Gaussian pulse shape). Despite the highly structured spectral shape, the temporal profile is reasonably smooth. The side lobes contain less than 10% of the pulse energy. The inset of Fig. 3.4.4 shows the corresponding long-range intensity AC trace. Possibility of multiple pulsing is eliminated by carefully checking the following points: The long-range AC trace shows no secondary pulse (up to 16 ps range, obtained by offsetting zero-delay point); The RF pulse spectrum is not modulated (using a 12 GHz photodiode and a 26 GHz spectrum analyzer, thus eliminating a secondary pulse with temporal spacing larger than 25 ps); There is no periodic modulation on the optical spectrum (wavelength resolution of 15 pm of the analyzer corresponds to absence of a secondary pulse within a time window of <200 ps).

The autocorrelation of the simulated temporal shape is calculated based on simulated grating compression with corresponding GVD and TOD parameters and the grating spacing optimized for minimum chirp. The FWHM width of the simulated pulse is 148 fs, in close agreement with the experiment. The intensity AC traces of the measured and the simulated pulses are plotted in the Fig. 3.4.5, showing reasonable agreement. The simulated pulse shape is shown in the inset. The measured pulse duration at 10.6 W is 25% higher than the zero-phase-transform-limited value, which we attribute to uncompensated TOD and SPM.

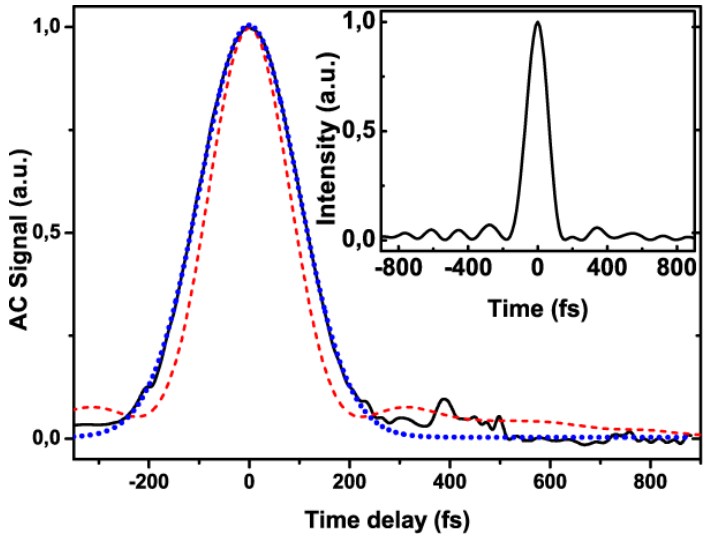

Fig. 3.4.5. Intensity autocorrelation of the measured (solid, black line), along with a Gaussian fit (dotted, blue line) and simulated (dashed, red line) pulses at 10.6 W of power. Inset shows the corresponding simulated temporal pulse shape.

The measured and simulated variation of the FWHM pulse width as a function of the output power is shown in Fig. 3.4.6. Initially, the pulse width decreases with power as SPM-induced spectral broadening counteracts gain narrowing. The minimum pulse duration of 137 fs is obtained at 5 W of power. However, beyond this point, the pulse width gradually increases due to excessive SPM. The optimal amount of grating spacing required

to dechirp the pulses over the range of operating power corresponds to a total GVD range of -0.93 ps^2 to -0.97 ps^2. The amount of TOD from the gratings over the same range is about $+0.00015$ ps^3. The TOD introduced by the grating pair is of the same sign as that of the optical fiber. This indirectly places a limitation on the maximum pulse energy achievable, since further stretching of the pulses to reduce SPM would lead to accumulation of even more TOD in the compressor. It has been shown that prisms can be introduced in the pulse compressor for TOD control [27].

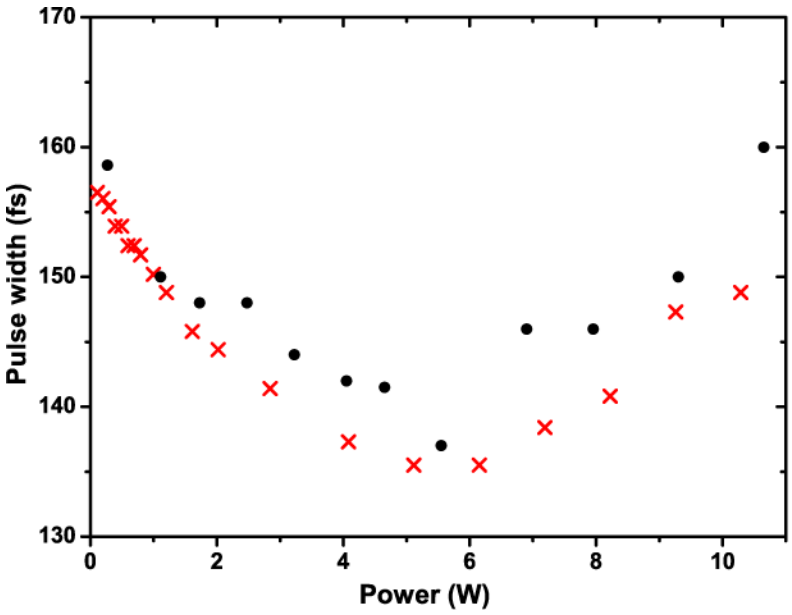

Fig. 3.4.6. Measured (black circles) and simulated (red crosses) variation of the FWHM width of the compressed pulse as a function of the output power.

Good beam quality is essential for any intended application and it must be checked carefully when using LMA fibers that are not strictly single mode. The spatial beam quality of the laser system is characterized by the well-known beam propagation method [74]. To this end, an artificial waist is created by focusing the beam and the beam radius is measured

around the waist region as a function of distance from a reference plane with a beam profiler and motorized delay stage. The M^2 parameter is estimated using the propagation equation given by

$$w(z) = w_0 \sqrt{1 + \left[\frac{M^2 \lambda (z - z_0)}{\pi w_0}\right]^2}, \tag{3.4.1}$$

where $w(z)$ is the spot radius at a distance z from the reference plane, w_0 the waist radius, λ the wavelength of the beam, z_0 is the waist location and M^2 is the beam propagation factor.

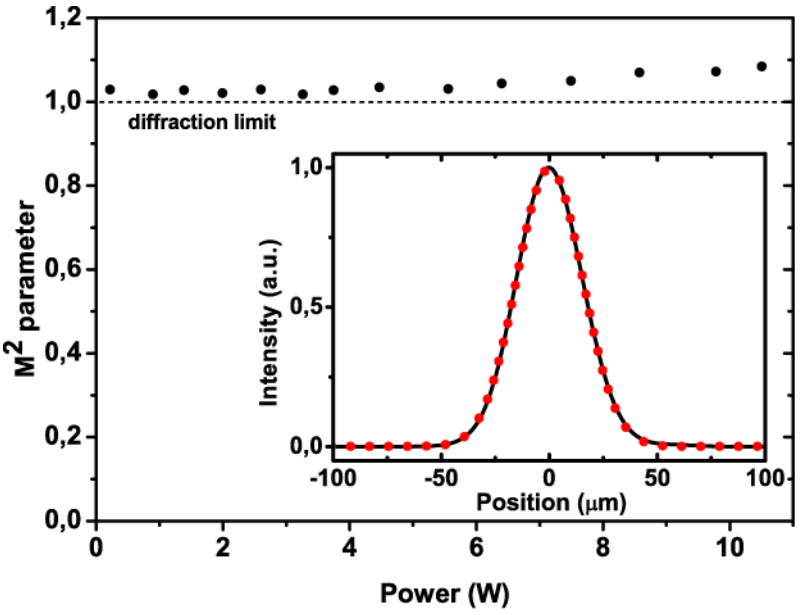

Fig. 3.4.7. Variation of the M^2 parameter with output power. Inset is a measured beam profile (solid, black line) along with a Gaussian fit to it (red, dotted line).

In Fig. 3.4.7, we plot the variation of M^2 parameter as a function of the output power. It can be seen that the beam quality remains close to the diffraction-limited value (M^2 < 1.1) even at 10.6 W of power. The estimated error for the M^2 value obtained by fitting of the multimode beam propagation equation is <3%. The beam is circular in shape with a Gaussian intensity distribution (inset of the Fig. 3.4.7).

The signal-to-noise ratio of nearly all laser experiments is ultimately limited by fluctuations in the laser power, i.e., laser intensity noise. Low laser intensity noise is directly linked to repeatability and uniformity in applications based on laser-material interactions with femtosecond pulses due to the highly nonlinear nature of these interactions. It is well known that intensity noise can easily be increased during amplification due to pump noise of the amplifying stages and ASE introduced during amplification, which can be kept low through careful optimization [75]. Even though impressive advances have been made with ever more powerful Yb-doped fiber amplifiers in recent years, there is virtually no discussion of how the noise is affected in the high-power systems. Given that multiple stages of amplification are used and the system is typically optimized for maximum power output, there is reason to think that excess noise may be introduced. Any fluctuations due to asynchronous shift of the wavelengths with the pump power and temperature of the diodes can lead to increase in intensity noise. Therefore, we characterized the relative intensity noise (RIN) of our laser system using the standard method [76]. In this method, the laser signal is detected with an InGaAs detector with 5 ns rise time. Since the detected periodic signal has an amplitude modulation spectrum common to all harmonics, measuring the spectrum of the photocurrent at baseband gives the desired noise spectrum. Signal at baseband is obtained by passing the photocurrent through a low-pass filter (DC to 1.9MHz). The output of the filter is sent to a high dynamic range baseband spectrum analyzer (bandwidth of 250 kHz) to obtain the noise spectrum. The noise spectrum gives the RIN in the photocurrent signal at the single sideband (SSB).

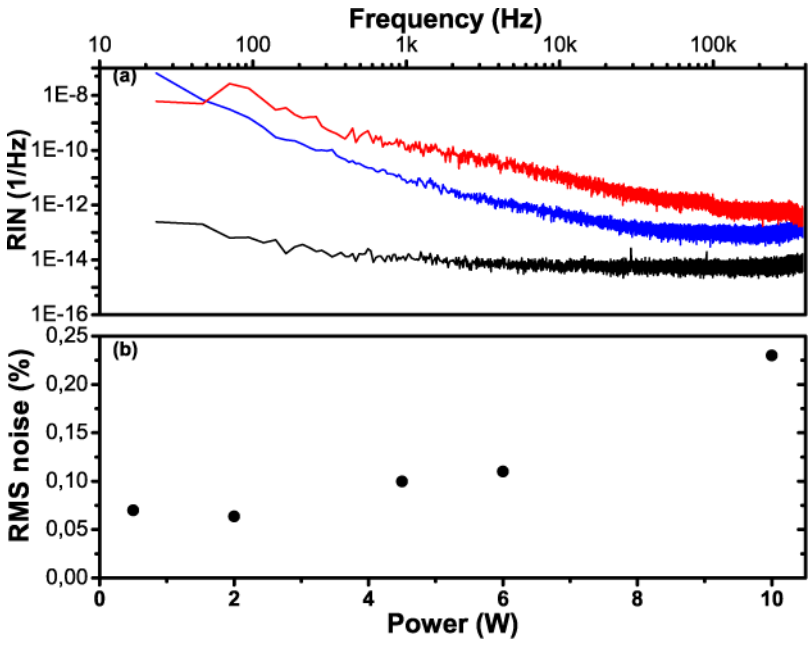

Fig. 3.4.8. (a) Measurement of relative intensity noise (RIN): upper (red) curve is the amplifier RIN at 10.6 W of power, middle (blue) curve is the oscillator RIN, and lower (black) curve is the noise floor. (b) Variation of integrated noise as a function of power for the frequency range of 20–250 kHz. Integrated noise of the oscillator is 0.029% over the same range.

Fig. 3.4.8(a) displays the SSB spectral density of RIN of the output from the oscillator–amplifier system. It can be seen from the figure that the noise is increased significantly in the amplifier stage at high powers. It is convenient to refer to the integrated noise for quantitative comparison, which is obtained by integrating the spectral density of RIN over a specified bandwidth (also multiplied by a factor of 2 for double sidebands). Fig. 3.4.8(b) shows the calculated amplitude noise of the amplifier as a function of output power, integrated over a frequency range from 20 Hz to 250 kHz. The integrated noise of the oscillator is as low as 0.029% over the same range. Integrated noise for the amplifier output starts from 0.06% at lower powers and increases up to ~0.2% at 10.6 W. Systematic studies

are needed to fully understand the reason of the increase, but we attribute it partly to the small amount of ASE generated during amplification and partly to the better wavelength stability of the single-mode oscillator pump diode compared to the high-power pump diodes. To the best of our knowledge, this was the first time that the intensity noise of an ultrafast fiber-based amplifier system has been characterized. The noise level is found to be comparable to low noise continuous-wave fiber lasers [77] and significantly better than bulk ultrafast solid-state lasers.

We also explored the limits of our system. The pulse energy is limited by nonlinearity; higher energies would lead to distortion of the pulse shape. This can be overcome by reducing the undoped lead fiber of the collimator, by further chirping the pulses together by implementing TOD control [73] or by utilizing SPM-TOD compensation [78, 79]. The latter, however, requires use of several hundred meters of stretcher SMF. Pulse duration is currently limited by TOD and SPM. Also, it should be possible to reduce the amplifier intensity noise to values comparable to the oscillator noise by even better suppression of the small amount of ASE introduced in the power amplifier. We have successfully used this laser system in our laboratory for processing of various materials, primarily modification of Ti disk surfaces for biomedical applications. These results demonstrate the utility of the laser system and constitute an independent confirmation of the beam and pulse quality, which will be presented in Chapter 9.

3.5. Conclusion

In conclusion, we have demonstrated a 10.6 W (which was later increased to 20 W after further improvements for cooling of the active fiber and addition of extra pump diodes) fiber amplifier, based on strictly in-fiber pump delivery from several multimode diodes via

a multimode pump-signal combiner. The compact laser system consists of commercially available components and it is compact and robust. Pump-to-signal optical efficiency is 53%. The amplifier is seeded by pulses from an ANDi-type fiber laser for the first time. The repetition rate is 43 MHz. Amplified pulses are compressed to sub-160-fs duration, which shows that ANDi-type fiber lasers are suitable seed lasers, offering a simpler cavity structure and great potential for all-fiber integration. Nearly diffraction-limited ($M^2 < 1.1$) beam quality is obtained even at the highest powers. Despite its importance for virtually all applications, intensity noise of high-power femtosecond fiber amplifiers is largely unknown. As a first step in this direction, we have characterized the noise of the present system, which is measured to be <0.2%. We measured the ANDi-type oscillator's intensity noise to be <0.03%. Extensive numerical simulations explain the observed behavior of the system and closely guide the experimental efforts.

Chapter 4

All-Fiber All-Normal Dispersion Laser with a Fiber-Based Lyot Filter

4.1. Introduction

In this chapter, we propose the use of a short section of polarization-maintaining fiber as a birefringent medium to construct an all-fiber Lyot filter inside the cavity of a fiber laser. This allows mode-locked operation of an all-fiber all-normal dispersion Yb-fiber oscillator without the use of a bulk bandpass filter and using standard components. This oscillator may also act as a seed for all-fiber amplifier systems such as the one explained in previous chapter. Note that the most of the results presented in this chapter were published in [80]. This work is mainly conducted by the author.

All-normal-dispersion fiber lasers working in the ytterbium wavelength region have attracted much interest because of their simpler cavities compared with other types of fiber lasers [25, 81]. The large chirp on the pulse minimizes the nonlinear effects and allows high-energy operation. The mode-locked operation is described well by dissipative soliton formation [82]. In practice, the use of an interference or birefringent filter instead of a

grating pair amounts to a certain simplification of the cavity. However, these filters are bulk components, whereas an all-fiber oscillator design is attractive, as it would be misalignment free. Various approaches have been pursued to build an all-fiber cavity operating at 1 μm. Prochnow *et al.* [83] used a saturable Bragg reflector along with nonlinear polarization evolution (NPE) for building an all-fiber cavity and obtained 0.8 nJ, 10 ps pulses compressible up to 627 fs. Nielsen *et al.* [84] used a fiber Bragg grating for spectral filtering in their laser, which is mainly based on nonlinear polarization rotation. Their pulse energy was 1.3 nJ with 5.6 ps duration. Kieu *et al.* [85] used a wavelength division multiplexing (WDM) based filter along with a carbon nanotube saturable absorber and obtained 3 nJ, 1.5 ps pulses that could be dechirped to 250 fs. Schultz *et al.* [86] also used a WDM based filter along with NPE producing 1.8 nJ, 7.6 ps pulses that can be dechirped to 179 fs. Lastly, Fekete *et al.* [87] used a semiconductor saturable absorber along with NPE in order to obtain 0.2 nJ, 10 ps pulses compressible to 200 fs.

Here, we demonstrate theoretically and experimentally that a short section of polarization-maintaining (PM) fiber placed after a polarizer mimics a Lyot filter [88], allowing the construction of an all-fiber all-normal-dispersion Yb-doped fiber laser using standard components. NPE [89] is utilized as an effective saturable absorber to start and stabilize the mode-locked operation.

4.2. Theory

A Lyot filter is ordinarily composed of two polarizers with a birefringent plate at an angle of 45° sandwiched in between (Fig. 4.2.1). The first polarizer imposes linear polarization, which is decomposed into orthogonal states as it couples to the fast and slow axes of the

birefringent medium. The birefringence leads to the accumulation of a relative phase difference, $\Delta\varphi$, between the beams propagating along the slow and fast axes, which corresponds to wavelength-dependent rotation of the polarization state. The second polarizer converts this rotation into amplitude modulation, and the transmittance is given by $T = \cos^2(\Delta\varphi/2)$. Thus a spectral filter with cosine-square profile is obtained [90].

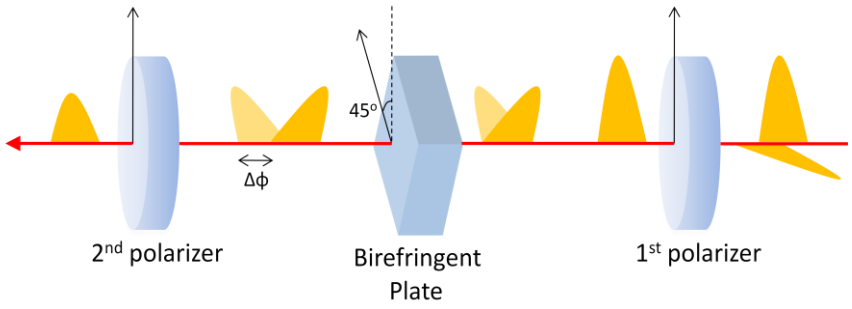

Fig. 4.2.1 Schematic of a Lyot Filter.

In our all-fiber-integrated scheme, PM fiber output of an in-fiber polarizing beam splitter (PBS) is spliced to a length of PM fiber, which acts as the birefringent plate. The axes of the two PM fibers are spliced at an angle (nominally 45°), thereby coupling light into both axes of the PM fiber. Ordinarily this should be followed by a second PBS; however, it is not needed for a ring cavity configuration, since the first PBS delivers the function of the second polarizer at the end of one round trip.

A schematic of the laser cavity is shown in Fig. 4.2.2, with the polarization evolution indicated. The bandwidth, central wavelength, and the modulation depth of the filter are in principle controllable. The phase difference accumulated between the fast and slow axes over a section of PM fiber is given by

$$\Delta\varphi = (2\pi/\lambda)L\Delta n, \tag{4.2.1}$$

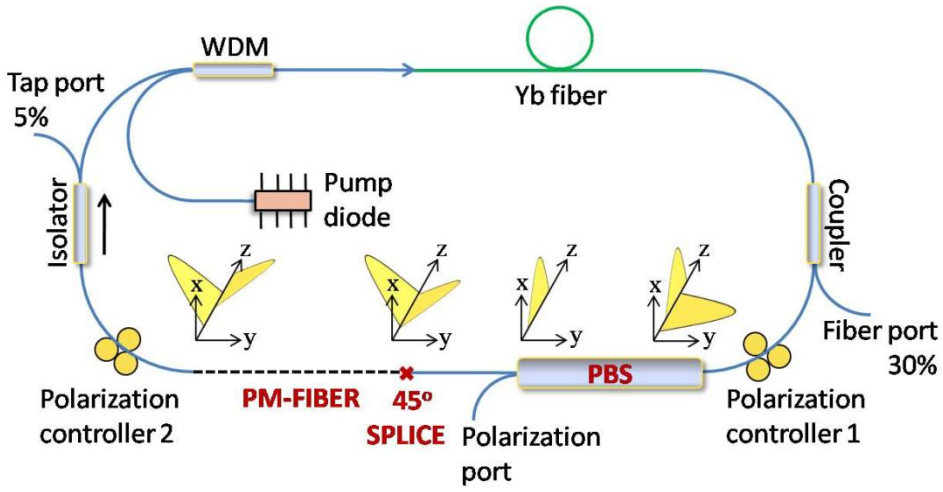

Fig. 4.2.2. Sketch of the setup. The Lyot filter action is illustrated. Fast axis of the PM fiber makes a 45° angle with the polarizer. The *z* axis is along the fiber direction.

where L is the length of the PM fiber, λ is the wavelength, and $\Delta n = n_{slow} - n_{fast}$ is the birefringence. The boundary conditions imposed by the cavity will be the same if the phase difference $\Delta\varphi$ accumulated in the PM-fiber section is a multiple of 2π. Two successive wavelengths satisfying this condition are $\lambda_m = L\Delta n/m$ and $\lambda_{m+1} = L\Delta n/(m+1)$, where m is an integer. Assuming $m \gg 1$, the peak-to-peak filtering bandwidth, $\Delta\lambda$, of the PM-fiber section is given by

$$\Delta\lambda = \lambda_m - \lambda_{m+1} = L\Delta n\left(\frac{1}{m} - \frac{1}{m+1}\right) \cong \frac{\lambda^2}{L\Delta n}. \qquad (4.2.2)$$

Thus the bandwidth can be controlled through the length of the PM fiber section. After the PM fiber, the beam undergoes polarization rotations through the rest of the cavity until it reaches to the PBS again. A simplified analysis of the cavity based on Jones matrices,

beginning from the PBS, can be constructed to illustrate the key properties of the filter. If the electric field in the fiber is represented by the following Jones matrix

$$\begin{bmatrix} E_x \\ E_y \end{bmatrix}. \tag{4.2.3}$$

its evolution can be investigated throughout the cavity by multiplying it with the Jones matrices of single components one by one. Jones matrix of the first component (PBS) is given by

$$\begin{bmatrix} 1 & 0 \\ 0 & 0 \end{bmatrix}. \tag{4.2.4}$$

The PM fiber section spliced at an angle of θ is equivalent to a θ-angle-rotated birefringent plate. So its Jones matrix is given by

$$\begin{bmatrix} \cos\theta & -\sin\theta \\ \sin\theta & \cos\theta \end{bmatrix} \times \begin{bmatrix} e^{i\Delta\varphi} & 0 \\ 0 & 1 \end{bmatrix} \times \begin{bmatrix} \cos\theta & \sin\theta \\ -\sin\theta & \cos\theta \end{bmatrix}. \tag{4.2.5}$$

If we multiply Eq. 4.2.4 by Eq. 4.2.5, the combined effect of PBS and PM fiber can be written as

$$\begin{bmatrix} e^{i\Delta\varphi}\cos^2\theta + \sin^2\theta & 0 \\ \left(e^{i\Delta\varphi} - 1\right)\sin\theta\cos\theta & 0 \end{bmatrix}. \tag{4.2.6}$$

After the PM fiber section, the polarization state of the beam will experience arbitrary polarization rotations for the rest of the cavity. These rotations can be represented by the multiplication of Jones matrices for an arbitrary rotation α and retardation β:

$$\begin{bmatrix} \cos\alpha & \sin\alpha \\ -\sin\alpha & \cos\alpha \end{bmatrix} \times \begin{bmatrix} e^{i\beta} & 0 \\ 0 & 1 \end{bmatrix} = \begin{bmatrix} e^{i\beta}\cos\alpha & \sin\alpha \\ -e^{i\beta}\sin\alpha & \cos\alpha \end{bmatrix} \tag{4.2.7}$$

As a result, after one roundtrip the electric field matrix becomes

$$\begin{bmatrix} e^{i\beta}\cos\alpha & \sin\alpha \\ -e^{i\beta}\sin\alpha & \cos\alpha \end{bmatrix} \times \begin{bmatrix} e^{i\Delta\varphi}\cos^2\theta + \sin^2\theta & 0 \\ \left(e^{i\Delta\varphi} - 1\right)\sin\theta\cos\theta & 0 \end{bmatrix} \times \begin{bmatrix} E_x \\ E_y \end{bmatrix}, \tag{4.2.8}$$

where the left matrix represents the polarization rotations in the rest of the cavity and the right matrix represents the combined effect of the PBS and the PM fiber, which is spliced at an angle of θ. The modulation depth of the filter is determined by the ratio of light coupled into the slow and fast axes of the PM fiber and is maximized for 45° angle. By taking $\theta = 45°$, the resultant matrix simplifies and the Jones matrix of the electric field after one roundtrip can be calculated as

$$\begin{bmatrix} E_x' \\ E_y' \end{bmatrix} = \begin{bmatrix} \left(e^{i\Delta\varphi} + 1\right)e^{i\beta}\cos\alpha + \left(e^{i\Delta\varphi} - 1\right)\sin\alpha & 0 \\ -\left(e^{i\Delta\varphi} + 1\right)e^{i\beta}\sin\alpha + \left(e^{i\Delta\varphi} - 1\right)\cos\alpha & 0 \end{bmatrix} \times \begin{bmatrix} E_x \\ E_y \end{bmatrix}. \tag{4.2.9}$$

The peak transmission wavelength is given by the condition for maximizing the horizontal electric field component E_x'. This is because the beam is about to enter to the PBS again for the next roundtrip. Differentiating E_x' with respect to $\Delta\varphi$ and equating to zero yields

$$\tan\Delta\varphi = -\tan(2\alpha)\sin\beta. \tag{4.2.10}$$

For $\alpha, \beta = 0$, it reduces to an ordinary Lyot filter, and the maximum transmission occurs at $\Delta\varphi = 2\pi m$, where $m = 0, 1, 2, \ldots$. For different α and β values, peak transmission wavelength shifts, but the filter bandwidth is unchanged. Thus the peak transmission

wavelength can be controlled by polarization controllers, though this degree of freedom is reserved for NPE operation and offers little practical value.

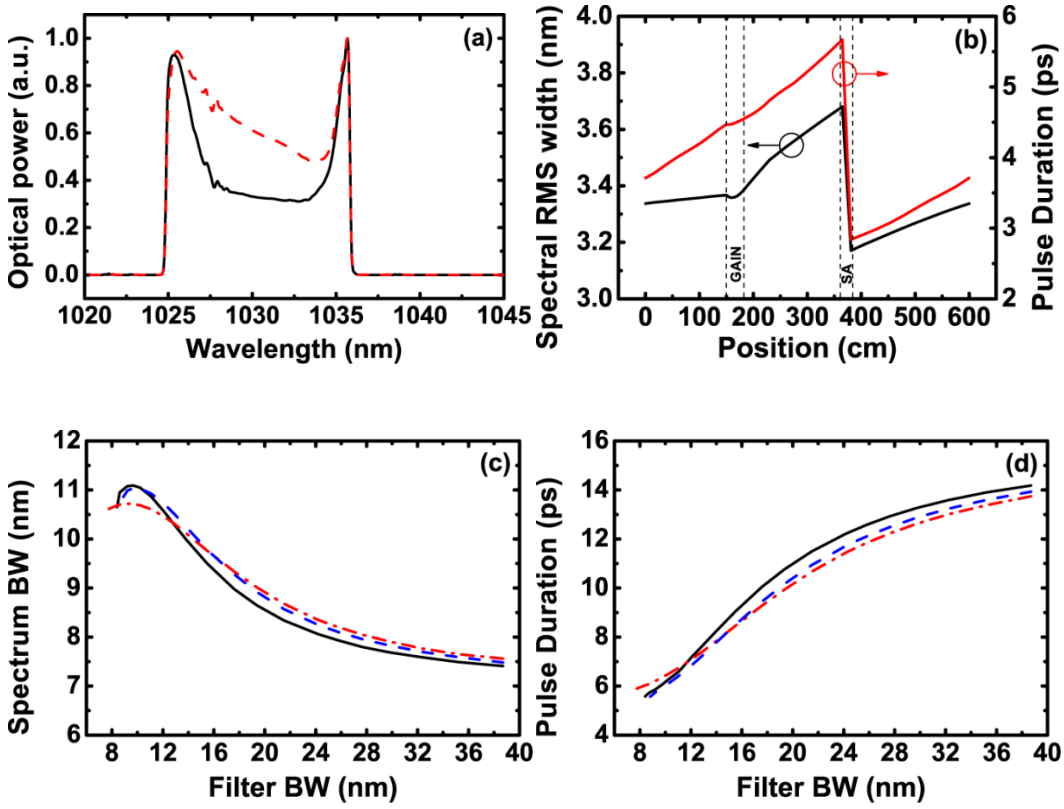

Fig. 4.2.3. (a) Simulated laser spectrum after the gain fiber (solid black curve) and after the PM fiber (red dotted curve). (b) Simulated spectral bandwidth (solid black curve) and pulse duration [solid gray (red) curve] variation over the cavity. Comparison of (c) the spectral width and (d) the pulse duration obtained numerically with the PM-fiber filter (solid black curves), Gaussian filter (red dashed-dotted curve) and cosine-square filter (blue dotted curves).

Although the operation of a PM fiber implementation of the Lyot filter is straightforward for a CW laser, its applicability to mode-locked operation is not clear *a priori*. In addition

to the phase-difference accumulation, there is temporal walk-off due to the difference in group velocities along the PM fiber, which can destabilize mode-locked operation by breaking a pulse into two components. We have resorted to numerical simulations based on the model described in [54] to address these questions using parameters that correspond to the experiments described below. The effect of the walk-off is modeled by splitting the field into two components corresponding to the fast and slow axes of the PM fiber. The slow component is temporally delayed and then the components are added together, similar to the analysis in [91]. We find that maximum tolerable walk-off increases with decreasing modulation depth of the filter. For maximum modulation depth, stable operation is attained for up to ~600 fs temporal walk-off, which corresponds to a minimum (peak-to-peak) filter bandwidth of approximately 6 nm. Fig. 4.2.3 shows the simulation results obtained with the PM fiber filter, in comparison with ordinary filters with cosine-square and Gaussian shapes.

4.3. Experimental Results & Simulations

Encouraged by the simulation results, we constructed an all-normal-dispersion Yb-fiber laser oscillator (Fig. 4.2.2). A 980 nm diode pumps a highly doped 30-cm-long Yb-fiber through a WDM. Approximately 30% of the beam is extracted from the cavity through a fiber coupler placed after the gain fiber. The rest of the light is sent to the PBS. A section of PM fiber is spliced at 45° angle to the PM lead fiber of the PBS. All the other fibers in the cavity are non-PM. An inline isolator ensures unidirectional operation and has a 5% output port for monitoring purposes. Two in-line polarization controllers are used to control the polarization. Since a number of cavity elements can effectively function as unintended filters, it is important to verify that the PM-fiber filter is the dominant filtering mechanism.

This is confirmed by CW operation of the laser, which operates only at distinct wavelengths, with fixed distances between the peaks (Fig. 4.3.1). The peaks shift all together when the polarization state is changed via polarization controllers, as predicted by Eq. 4.2.1. For two different PM fiber lengths, namely 37 cm and 24 cm, the measured (peak-to-peak) bandwidths are 6.5 nm and 10.0 nm, respectively.

These values precisely match the inverse scaling of bandwidth with fiber length. The calculated birefringence of the fiber is $\Delta n = 4.4 \times 10^{-4}$, which is very close to the value obtained from the beat length ($L_B = \lambda/\Delta n$) specified as ≤ 2.7 mm by the manufacturer.

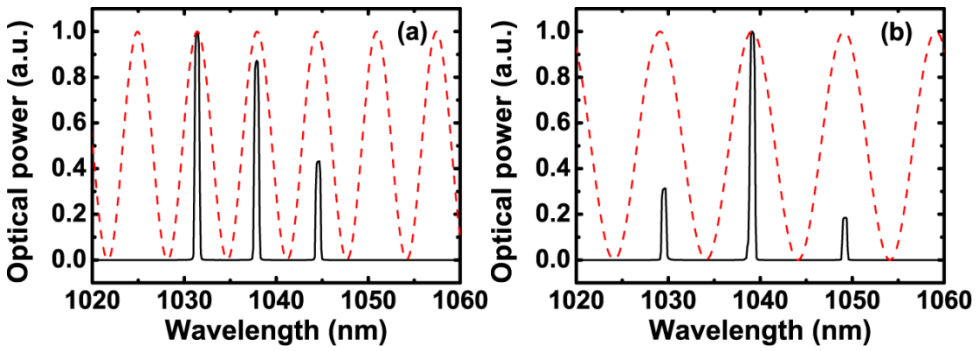

Fig. 4.3.1. Measured optical spectra for CW operation (solid black curve) and theoretical transmission curves (red dotted curves) for effective filter bandwidths of (a) 6.5 nm and (b) 10 nm.

For the remainder of the work, we set the PM-fiber length to 28 cm, which corresponds to 8.6 nm filter bandwidth and 410 fs of temporal walk-off. The laser is mode-locked easily by adjusting the polarization controllers. The output power of the laser is 33 mW at the 30% fiber port and 50 mW at the polarization port at a repetition rate of 34 MHz, which corresponds to 1.0 nJ and 1.5 nJ of pulse energy at the fiber and polarization ports, respectively. The intracavity pulse energy is 3.3 nJ after the gain fiber. Fig. 4.3.2 shows the

spectra of the laser obtained at different ports, showing that the spectral filtering is taking place primarily at the PBS, as expected. The laser produces chirped pulses, which are compressed externally using a grating compressor, giving a minimum pulse duration of 230 fs, assuming a Gaussian deconvolution factor. The autocorrelation trace of the compressed pulses and high-dynamic-range RF spectrum are shown in Fig. 4.3.2(d). The RF spectrum of the laser shows 90 dB suppression of the sidebands, which are 1.5 kHz apart. There is no sign of multiple-pulsing at this energy level, which is limited by the maximum available pump power of 300 mW.

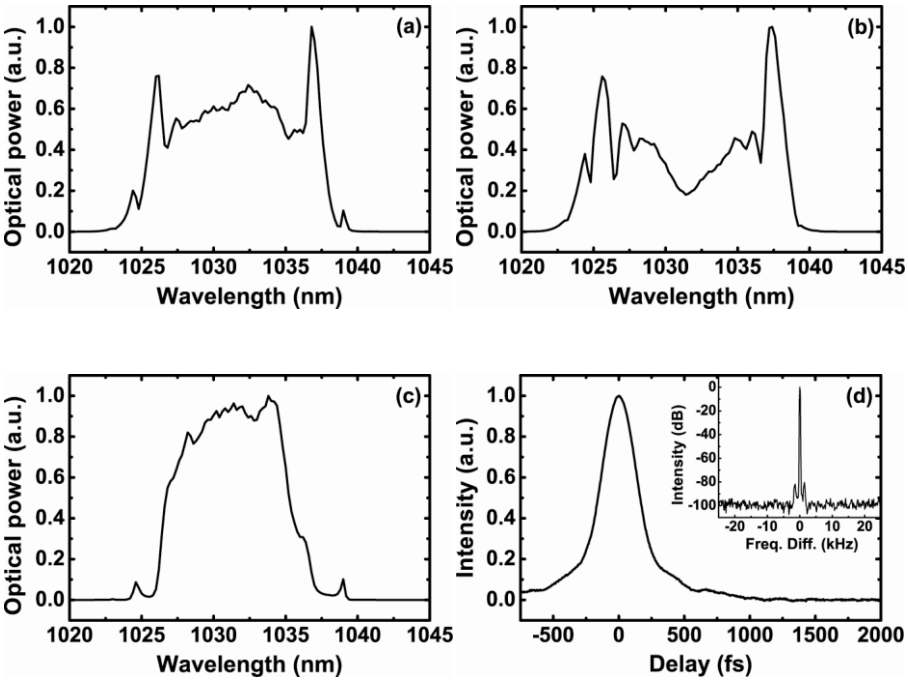

Fig. 4.3.2. Measured spectra of pulses for 8.6 nm effective filter bandwidth from (a) the 30% fiber port, (b) the polarization extraction port, (c) the 5% tap port. (d) Measured autocorrelation of the pulses from the 30% fiber port. Inset: RF spectrum of the pulses.

4.4. Conclusion

In conclusion, we demonstrate that a PM-fiber section inserted into an all-normal-dispersion laser cavity functions as a Lyot filter and stable mode-locked operation is possible, which is confirmed experimentally and numerically. The filter bandwidth and modulation depth are adjustable through the length and splice angle of the PM-fiber section, respectively. We have demonstrated an all-fiber Yb-doped laser cavity without using specialty components such as semiconductor saturable absorbers or chirped fiber Bragg gratings for the first time to our knowledge. The laser generates 1.0 and 1.5 nJ-energy pulses from its two ports. The pulses can be dechirped to ~230 fs. Low-noise operation is confirmed by high dynamic- range RF spectrum measurements. Its all-fiber design is highly compatible with all-fiber amplifier systems.

Chapter 5

83 W, 1 ns, 3.1 MHz All-Fiber Laser For Micromachining

5.1. Introduction

In this chapter, we demonstrate an all-fiber-integrated laser based on off-the-shelf components producing square-shaped, 1 ns-long pulses at 1.03 μm wavelength with 3.1 MHz repetition rate and 83 W of average power. The master-oscillator power-amplifier system is seeded by a fiber oscillator utilizing a nonlinear optical loop mirror and producing incompressible pulses. A simple technique is employed to demonstrate that the pulses indeed have a random chirp. We propose that the long pulse duration should result in more efficient material removal relative to picosecond pulses, while being short enough to minimize heat effects, relative to nanosecond pulses commonly used in micromachining. Micromachining of Ti surfaces using 0.1 ns, 1 ns and 100 ns pulses supports these expectations. Note that the most of the results presented in this chapter were published in [92]. This work is mainly conducted by the author. Bülent Öktem helped with materials processing experiments, Sinem Yılmaz made the high-power splices of critical importance, and Koray Eken constructed the 100-ns-pulsed oscillator and the optical delivery system.

There is much interest in high-power, short-pulsed fiber lasers, which are finding applications in a diverse range of scientific, industrial, biomedical and defense applications. In particular, the use of short-pulsed fiber lasers in material processing is promising due to their simplicity, low cost and ease of use. For precision micromachining [93], surface texturing [94], pulsed laser deposition [95], and marking, typically relatively low power (< 20 W) pulsed fiber lasers are utilized. The pulse durations and repetition rates range from 100 fs to 100 ns and from 20 kHz to 100 MHz, respectively. High repetition rates and sub-nanosecond pulses are usually generated by mode-locked lasers; low repetition rates and nanosecond pulses rely on Q-switched or directly modulated diode lasers. The region around few MHz is harder to access. Generally, use of ultrafast fiber lasers requires complex pulse picking systems and pulse stretchers and compressors to manage nonlinear effects. The dynamics of mode-locked fiber oscillators are governed by a rich interplay of Kerr nonlinearity, dispersion, and gain [96]. A commonly encountered but usually ignored operation mode is where very long, incompressible pulses are produced. This type of pulses was first observed in Er-doped fiber lasers, which were referred to as noise-like [97, 98]. In cavities utilizing saturable absorbers (SA) with sinusoidal transmission, such as nonlinear polarization evolution or nonlinear loop mirror (NOLM) [102], if the pump power is increased beyond a critical point, the pulse will collapse to a bunch of small pulses [99] due to the peak power clamping effect [100]. The mode characteristically exhibits a broad, smooth spectrum and is evidenced by an autocorrelation trace with a narrow coherence peak on top of a large pedestal [97]. However, if the net cavity dispersion is large and positive, square-shaped, few nanosecond pulses [101] are formed, which are also incompressible, but having a narrower spectrum. Fiber laser cavities producing such pulses have low repetition rates of around few MHz, which is convenient for easily reaching microjoule energies through external amplification. In addition, the ~1-ns pulse duration and sub-microsecond pulse-to-pulse spacing is an interesting regime for micromachining, with the expected performance being intermediate to ultrafast pulses and long nanosecond

pulses: The longer lasting plasma formation as well as pulse-to-pulse cumulative effects should lead to more efficient ablation. Yet, the pulse duration remains short enough to limit the heat affected zone (HAZ).

In this work, we demonstrate an integrated Yb-fiber laser producing square-shaped, 1 ns-long pulses at 1.03 μm wavelength with 3.1 MHz repetition rate and 83 W of average power. This is, to the best of our knowledge, the first use of a NOLM [102] in producing square nanosecond pulses. This, in principle, allows the all-fiber-integrated system to be constructed entirely from polarization maintaining (PM) fibers for ultimate environmental stability. We show, using a simple technique, that these pulses indeed have an incompressible chirp. Finally, we make a comparison of the Ti-surface micromachining performance using 0.1 ns, 1 ns and 100 ns pulses.

5.2. Experimental Results & Discussion

Schematic of the experimental setup can be seen in Fig. 5.2.1. The oscillator comprises of a 0.7-m-long Yb-doped fiber, followed by a 30% output coupler, a 10-nm bandpass filter, an inline isolator to ensure unidirectional operation and a 50-m-long Sagnac loop. The fundamental repetition rate of the cavity is 3.1 MHz. Although the oscillator can operate without the bandpass filter, its presence sets the central wavelength and improves stability. As pump source, we use a fiber-coupled single-mode 980-nm diode laser delivering a maximum power of 650 mW. The oscillator output seeds a two-stage all-fiber amplifier, similar to the system described in Ref. [54]. A core-pumped preamplifier stage is used to increase the signal level up to 170 mW. The power amplifier stage is composed of a multiple-port pump-signal combiner (MPC) and six pump diodes coupled to 105 μm-core

multimode (MM) fibers, each delivering up to 25W. The double-clad Yb-doped fiber of the power amplifier in this study has 25 μm core diameter, core numerical aperture of 0.07 and cladding diameter of 250 μm.

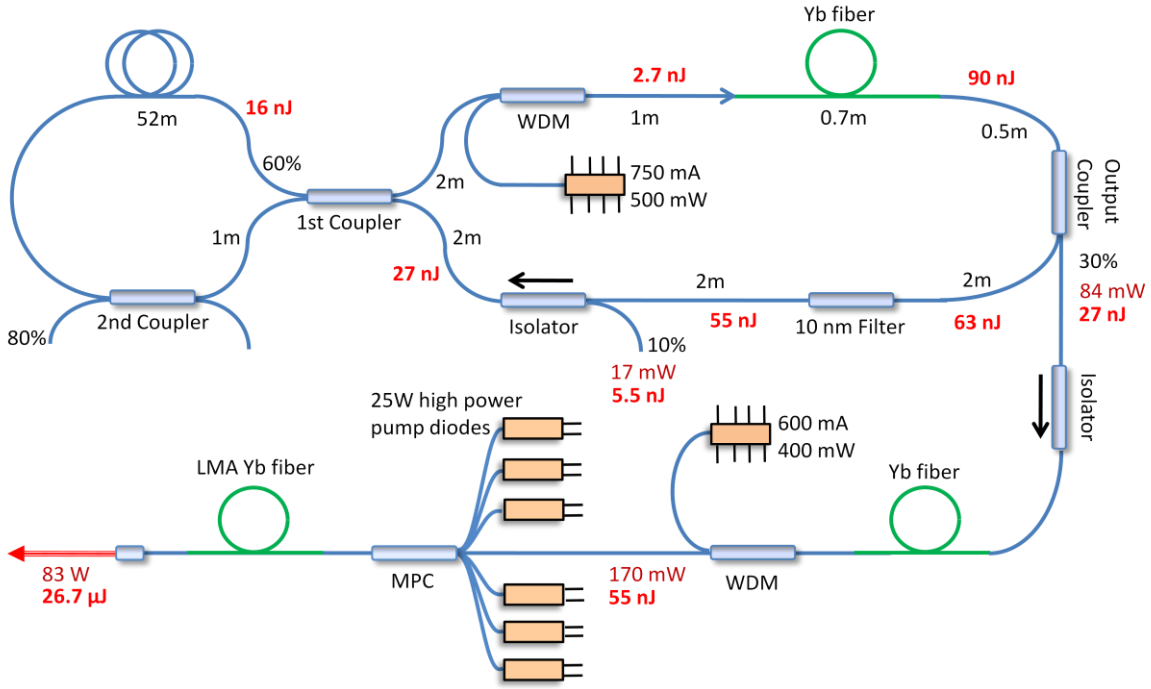

Fig. 5.2.1. Schematic of the oscillator-amplifier setup. WDM: Wavelength-division multiplexer; LMA: Large mode area; MPC: Multi pump combiner. The fiber lengths, powers and pulse energies are indicated.

Pulsed operation of the oscillator is attained readily. The nonlinear phase shift accumulated in the CW and CCW directions in the loop can be calculated by using

$$\Delta\varphi = \gamma PL = \frac{2\pi n_2}{\lambda}\frac{P}{A_{eff}}L, \tag{5.2.1}$$

where n_2 is the Kerr nonlinearity coefficient, P is the peak power and L is the effective propagation distance. Using experimental values, the relative phase shift between two counter propagating beams is estimated to be close to $\sim\pi$. Thus, the laser converges on a state supporting a nearly square-shaped pulse, which is maximally transmitted through the NOLM. This is to be expected, given that the extra long pulse duration and random chirp nullifies the influence of dispersion. The pulse duration is determined by the intra-cavity energy with the peak power remaining constant. This is verified by changing the pump power from 350 mW to 650 mW. As expected, the pulse duration increases linearly with output power; no change in spectral width or shape is observed (Fig. 5.2.2(a)). Fig. 5.2.2(b) shows the optical spectrum recorded from the 10% monitor port of the isolator. The temporal profile of the pulses is measured with a 50-GHz sampling oscilloscope and 12-GHz photodiode, with a combined rise time of ~30 ps (Fig. 5.2.2(c)). The inset shows the RF spectrum of a comb line, which is clean of sidebands and modulations down to −70 dB, indicating low-noise operation and absence of Q-switching instability. The short-term power stability of the pulse train is further characterized by its relative intensity noise (RIN) spectrum measured using the standard method [76, 103]. The intensity noise, integrated over the range of 3 Hz to 250 kHz, is measured to be 0.66% for the oscillator and 1.86% after the power amplifier. Increase in the intensity noise after the power amplifier is attributed to pump fluctuations coupled from the relatively noisy MM pump diodes [54]. At full pump power, the amplifier output reaches 83W of average power, corresponding to ~25 μJ of pulse energy and 25 kW of peak power. Fig. 5.2.2(d) shows the optical spectrum of power amplifier at various output powers. The growing influence of Raman amplification is evident, confirming the high peak power of the source. The formation of a Raman-induced red-shifted peak is not detrimental to applications that depend solely on peak power since the Raman part of the spectrum is temporally overlapping the main pulse. Nevertheless, the pulse duration is confirmed to be unchanged at all power levels.

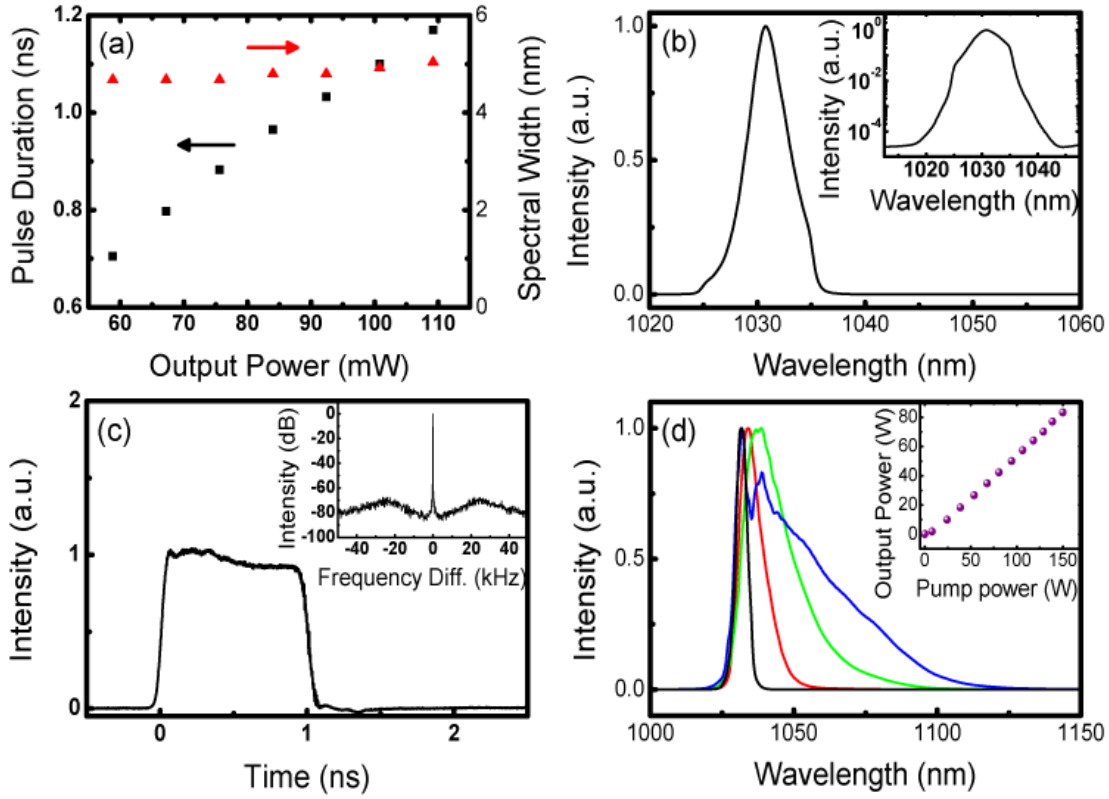

Fig. 5.2.2. (a) Variation of pulse duration (black) and spectral width (red) with the output power of the oscillator. (b) Optical spectrum of the pulse train measured at the 10% output port. Inset: Optical spectrum in logarithmic scale. (c) Pulse shape measured with a 30 ps-rise time sampling scope. Inset: RF spectrum of an individual comb line demonstrating low-noise operation. (d) Optical spectra measured directly from the oscillator (black), and from the amplifier output at powers of 26.6 W (red), 57.4 W (green), 83 W (blue). Inset: output power vs. pump power.

It is reasonable to ask if the oscillator simply has a giant, potentially very complex, but well-defined chirp, varying monotonically across the pulse. Although square-like pulsed

operation has been extensively studied, no direct confirmation of their phase or chirp profiles has been reported. We use a simple setup to measure the chirp on the pulses (Fig. 5.2.3(a)), similar to the spectrogram measurements in [104]. The oscillator's output is sent to a Mach-Zehnder interferometer, where a tunable bandpass filter is placed in one arm. The filtering action is obtained with a diffraction grating followed by a fiber collimator, which functions as a Gaussian aperture. The tuning of the central wavelength and the bandwidth of the filter is achieved by rotating the grating and by adjusting the distance to the fiber collimator, respectively. The output of the interferometer is sent to an optical spectrum analyzer along with a fast photodiode connected to the sampling scope. If the pulse has a well-defined and monotonic, albeit nonlinear temporal chirp, the spectral components constituting the pulse should be spread in time and also have a certain degree of temporal localization. Thus, spectrally filtering the pulse should produce shorter temporal waveforms, and the arrival time of different portions of the spectrum to the sampling scope should differ. We use a properly mode-locked all-normal dispersion (ANDi) laser [25] as reference for this measurement. The cavity setup is similar to that of Ref. [80] and its output is chirped to a duration of ~ 100 ps. While spectral filtering of the chirped pulses for the reference laser leads to shorter pulses, the pulse duration for the square-pulsed laser is unchanged (Fig. 5.2.3(b, c)). A spectrogram is obtained by recording the pulse width and temporal position against central wavelength for the filtered pulses. While results for the reference laser confirm the expected linear chirp (Fig 5.2.3(e)), for the 1 ns laser, the spectral components have virtually no fixed localization within the temporal envelope of the unfiltered pulse (Fig 5.2.3(d)). These results demonstrate conclusively that the square-like pulses are incompressible.

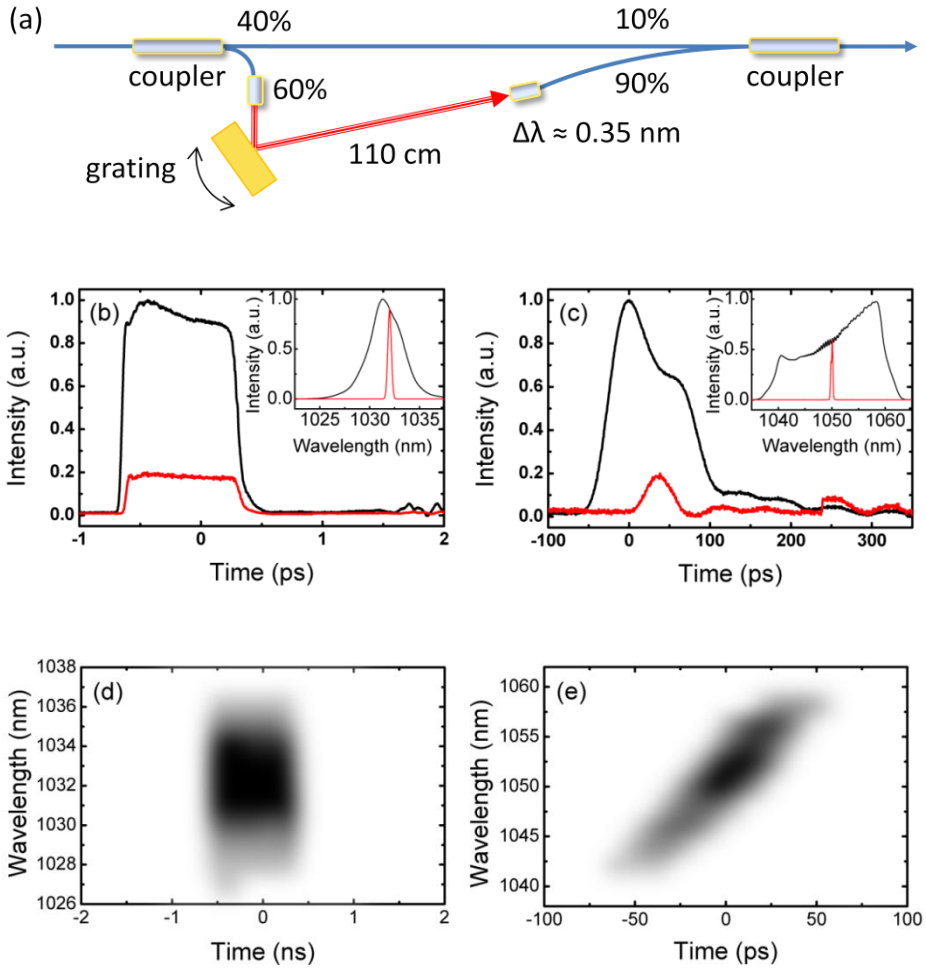

Fig. 5.2.3. (a) Experimental setup for the pulse chirp measurement. For (b) NOLM and (c) reference lasers, temporal and spectral (insets) profiles of the spectrally filtered (red) and unfiltered pulses (black). Spectrograms of (d) NOLM and (e) reference lasers are shown where gray-scaling indicates intensity. The data has been smoothened using Gaussian averaging to reduce graininess.

5.3. Micromachining of Ti Surfaces

In order to assess the utility of the system in material processing, we perform micromachine depressions on a polished titanium surface. The spot size is 20 μm. Three seed sources in these experiments, are connected to the same amplifier and followed by exactly the same delivery and focusing optics: the nanosecond system described here (1 ns pulses at 3.1 MHz), a commercial fiber laser set to produce 100 ns pulses at 31 kHz and a properly mode-locked ANDi fiber laser with 115 ps pulses at 27 MHz. All three systems are adjusted to yield the same peak power for the same average power. Fig. 5.3.1 shows the SEM images of holes produced at 3 W and 0.5 s exposure time in comparison. The depth of the holes is increasing with the pulse duration, indicating increased efficiency of material removal. On the other hand, the heat affected zone (HAZ) is significantly larger for the 100 ns pulses compared with the 0.1 ns and 1 ns pulses and the uniformity is poorer. A clear indication of the similarity of the 0.1 ns or 1 ns results and their distinction from the 100 ns results is the formation of similar sub-micron-sized crystalline structures, which are completely absent from the 100 ns results. Much of the formed structure is composed of TiO_2. Energy-dispersive X-ray spectroscopy measurements were performed, which indicate that the oxidation level is significantly larger for the 100 ns pulses. This can be explained by higher temperatures reached when using long pulses. These results are consistent with our qualitative expectations on the performance of 1 ns-long pulses.

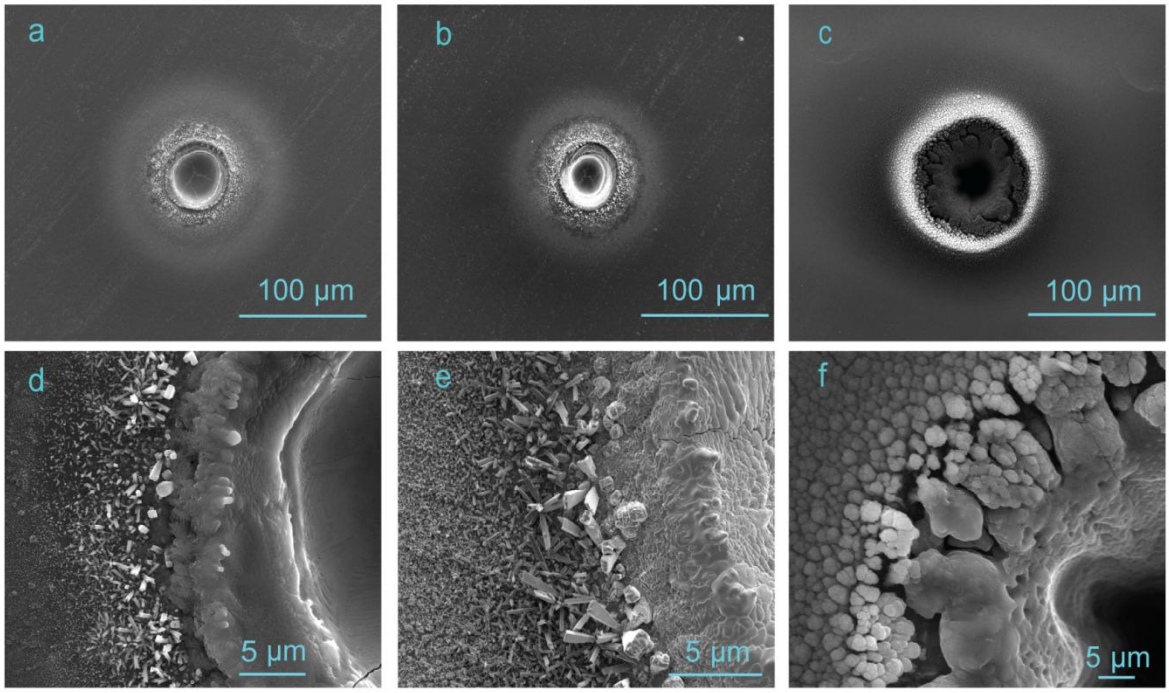

Fig. 5.3.1. Wells on the polished Ti surface drilled by (a) 115 ps, (b) 1 ns and (c) 100 ns pulses in comparison. (d,e,f) shows corresponding close SEM images.

5.4. Conclusion

In conclusion, we have demonstrated the generation of 1-ns-long pulses from an all-fiber-integrated Yb laser cavity, which uses a NOLM to initiate low-repetition-rate (3.1 MHz) pulsed operation, eliminating the need for pulse picking. We demonstrate, to our knowledge, the first use of such pulses in micromachining. Since beam propagation is fiber-guided everywhere, the laser system is extremely robust. We also verified using a simple setup that these pulses indeed lack a well-defined chirp and are, therefore, incompressible. Nevertheless, the intensity fluctuations of the oscillator are found to be low

(< 0.7%). We compared the micromachining performance of the 1 ns, 3.1 MHz laser system with an industrial fiber laser producing 100 ns-long pulses at 31 kHz and an ultrafast fiber laser system producing 115 ps-long pulses at 27 MHz, while maintaining the same average and peak power. The results indicate that the repeatability and uniformity of the micromachined surfaces are similar for the 1 ns and 0.1 ns lasers and significantly better than those of the 100 ns laser. The amount of ablated material is higher for the 1 ns laser than for the 0.1 ns, but lower than the 100 ns laser. This regime occupies a large portion of the phase space for long cavity lasers, exhibiting a high tolerance to environmental perturbations. In addition, the all-fiber-integrated architecture improves stability and allows for direct beam delivery to the sample via fiber. As such we expect it to find wide use in industrial applications.

Chapter 6

114 W Continuous-wave Fiber Laser System

6.1. Introduction

All of the systems presented in previous chapters are pulsed lasers. However, the most powerful laser systems in the literature are the continuous-wave (CW) systems such as [105]. This is partly because at high powers (more than 1 kW) the nonlinear effects begin to show themselves even in the CW regime, which means there is no room for pulsed operation. Instead, there are some quasi-CW systems, which are used at mid-powers in order to hold the peak power above a threshold by switching on and off the pump diodes. Recently, 2.1 kW of output power from a CW fiber laser was demonstrated [106] with free space coupling of the pump light (Fig. 6.1.1). In this setup, a 20 m of homemade Yb-doped fiber with 50 μm core diameter is used. Dichroic mirrors are used to split signal from the pump light and forming the laser cavity. For pumping, three diode stacks are utilized with lots of complicated optics for spatial beam combining and focusing. It is hard to say that this setup carries some of the main advantages of fiber lasers; simplicity and flexibility.

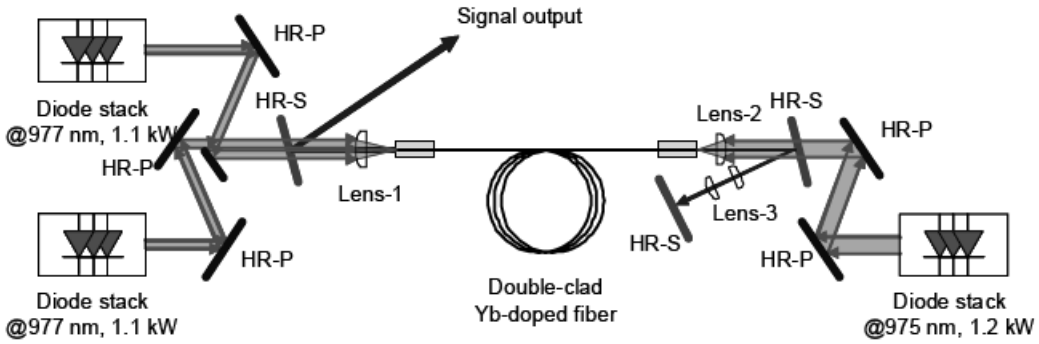

Fig 6.1.1. Experimental arrangement of 2.1 kW CW fiber laser [106]. HR-P: Highly reflective for the pump, HR-S: Highly reflective for the signal wavelength.

The alternative for the setup above is the all-fiber design. Here, there are no free space optics; diode stacks and lenses are replaced by fiber-coupled diodes and MPC, dichroic mirrors are replaced by fiber Bragg gratings (FBG). Sometimes, it is even enough to create the laser cavity by a single FBG in the input end and by the reflection from the cleaved output end of the fiber. However, the power levels of all-fiber lasers are far below the free space ones. Recently, a 300 W system [107] was demonstrated in 2008 followed by a 404 W system [108] in 2010.

In this chapter, we present our efforts on this concept. Sticking to the all-fiber design, we built a CW fiber laser system capable of delivering more than 100 W of output power. This power is limited by the available pump power and our splicing capabilities. We verified that making an extremely small loss splice is the key point in an all-fiber design. We also made extensive numerical simulations with a software mainly developed by Punya Paltani and modified by the author. In this study, Sinem Yılmaz helped the author in the construction of the experimental setup and numerical simulations, which guided the laser cavity design.

6.2. Experimental Results

The schematic of our experimental setup can be seen in Fig. 6.2.1. It is significantly simpler compared to the free space setup shown in Fig. 6.1.1. Of course, there can be several different arrangements. For example, it is possible to change the places of FBG07 with FBG99. In this case, the output will mix with the unabsorbed pump power, which is not a desirable situation. Another possibility is to change places of FBG07 with the MPC. It would be nice to take MPC out of the laser cavity by this change. However, there will be two critical splices in this case, which is a more detrimental situation.

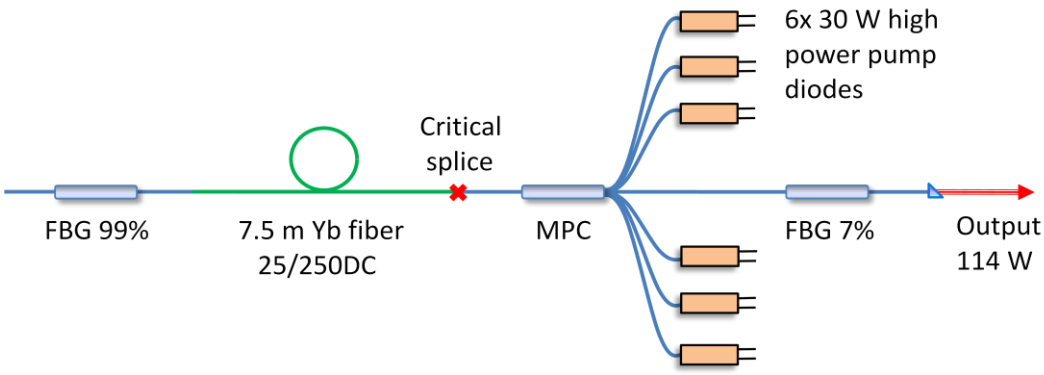

Fig. 6.2.1 Schematic of the all-fiber CW fiber laser.

There are two kinds of fibers in the setup; first one is the pump fibers, which have 105 μm core and 125 μm cladding diameter with 0.15NA. They are denoted as 105/125 fibers. The rest of the fibers are 25/250DC fibers, which have 25 μm core and 250 μm cladding diameters. DC stands for "double-clad", the details of which can be found in Chapter 2. Numerical apertures of the core and cladding are 0.06 and 0.46 respectively. The active

medium is composed of 7.5 m of Yb-doped fiber (Liekki Yb700-25/250DC) with a doping concentration of ~5×10^{25} m^{-3}. MPC is from ITF labs [42], which is a 6+1×1 combiner meaning that there are 6 pump inputs, 1 signal input and 1 output fiber. All of these ports are compatible with the fibers in the rest of the system. 30 W-capable pump diodes are from IPG photonics [28]. They can supply 30 W of output power at 12 A of diode current. Their wavelength can be stabilized at 975 nm (where the absorption of Yb-fiber is maximum) by proper cooling arrangements. Fig. 6.2.2 shows the characteristics of a sample pump diode.

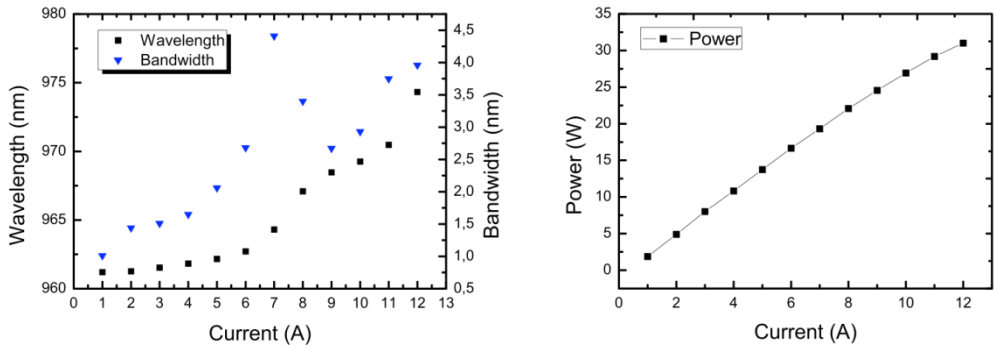

Figure 6.2.2 Characteristics of a sample 30 W pump diode.

Two FBGs are used in the system, which are produced as a pair by nLight [109]. One of them is highly reflective (99%) at 1060 nm wavelength with a bandwidth of 0.3 nm. The other has 7% reflectivity at the same wavelength with a bandwidth of 0.1 nm. A general problem of FBGs is that their operating wavelength shifts slightly with the temperature, which is not unusual for a high power operation. The difference in the bandwidths may compensate this shift up to a certain level.

Fig. 6.2.3 shows the output of the system versus launched pump power with a slope efficiency of ~61% and the output spectrum is given at 114 W. There are no signs of saturation, which means that the system is pump power limited.

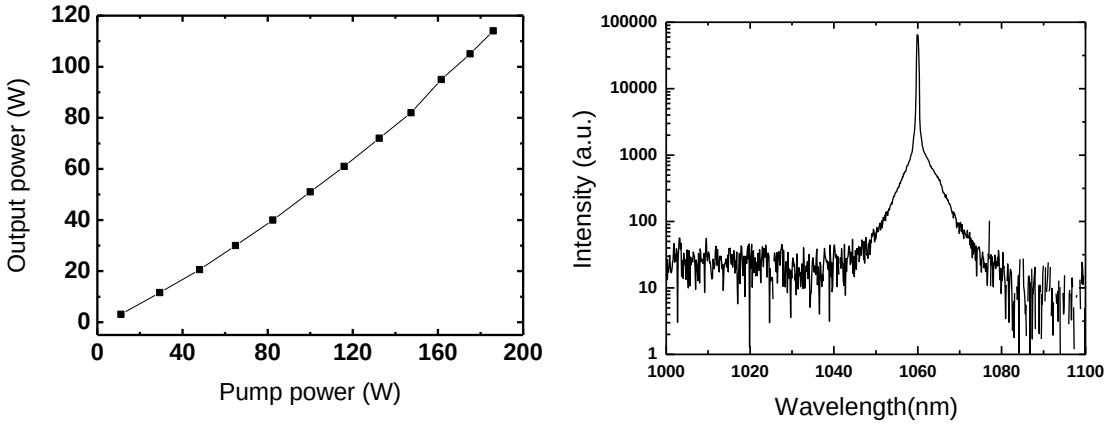

Figure 6.2.3 (a) Variation of the output power with respect to launched pump power. (b) Output spectrum at the maximum output of 114 W.

It can be said that we have successfully reached the limits of this system by fully utilizing all the 6 pump ports of the MPC by connecting the highest power pump diodes available in our hand and operating them at full capacity. However, there is still a problem that limits the output power. The most critical splice of the system is located in between output port of the MPC and Yb-doped fiber (Fig. 6.2.1), through which ~180 W of pump power is delivered. At these power levels, even a small loss may cause damage, so this splice should be very high quality, but our splice capabilities (especially for large diameter fibers like 250 μm) were limiting us here. The difference between one of our best splices and a perfect splice can be seen in Fig. 6.2.4.

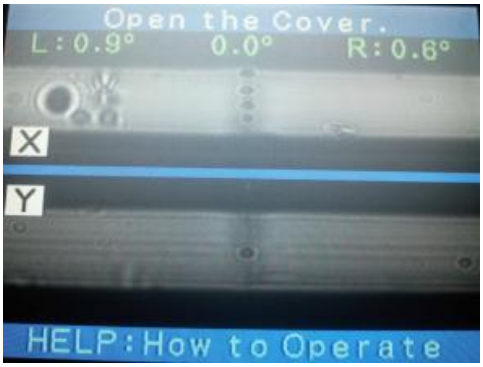

Fig. 6.2.4. The best splice we have obtained in comparison with a perfect splice. The small bubbles in the splice region are the sites for scattering.

As a result, we were forced to compensate the splice losses by an extensive cooling and we developed a water cooling system, which is far more efficient than air cooling. Water is chosen as the coolant because of its unique properties like high thermal conductivity, transparency near 1 μm wavelength, suitable index of refraction.

6.3. Simulations

In this section, we will present the simulation results obtained by using our simulation software where the laser medium is modeled as a two-level system. After setting the initial values of pump and signal powers at the entrance of the fiber, their values are iterated throughout the gain fiber several times until a steady-state is reached. It is also possible to use two FBGs reflecting at the desired wavelength such that the signal develops by itself. Mathematically, we can write the two coupled differential equations below in order to model a two-level laser system;

$$\frac{\mathrm{d}P_p}{\mathrm{d}z} = \eta_p\left(\sigma_{ep}n_2 - \sigma_{ap}n_1\right)N_{tot}P_p, \tag{6.3.1}$$

$$\frac{\mathrm{d}P_s}{\mathrm{d}z} = \eta_s(\sigma_{es}n_2 - \sigma_{as}n_1)N_{tot}P_s, \tag{6.3.2}$$

where P_p and P_s are the pump power and the signal power; η_p and η_s are the corresponding overlap factors; σ_{ep} and σ_{ap} are the emission and absorption cross sections for the pump wavelength; σ_{es} and σ_{as} are those for the signal wavelength. N_{tot} is the total population density, n_1 and n_2 are the population density ratios for the lower and upper levels respectively. The upper and lower-state population density ratios have steady-state values given by

$$n_2 = \frac{R_{12} + W_{12}}{R_{12} + R_{21} + W_{12} + W_{21} + A_{21}}, \qquad n_1 = 1 - n_2, \tag{6.3.3}$$

where transition rates are given by

$$R_{12} = \frac{\sigma_{ap}I_p}{h\nu_p}, \quad R_{21} = \frac{\sigma_{ep}I_p}{h\nu_p}, \quad W_{12} = \frac{\sigma_{as}I_s}{h\nu_s}, \quad W_{21} = \frac{\sigma_{es}I_s}{h\nu_s}, \quad A_{21} = \frac{1}{\tau_1}. \tag{6.3.4}$$

Here, A_{21} is the spontaneous transition rate, which is defined as the inverse of the upper-state lifetime. The values for σ_i can be obtained from experimental data such as given in Fig.3.2.1 for Yb-doped silica fiber. Lastly, $I_i = P_i/A_{eff}$ represents the intensity.

Having all these in hand, we first tried to get the experimental graph given in Fig. 6.2.3(a) by our simulations and obtained a successful result that can be seen in Fig. 6.3.1.

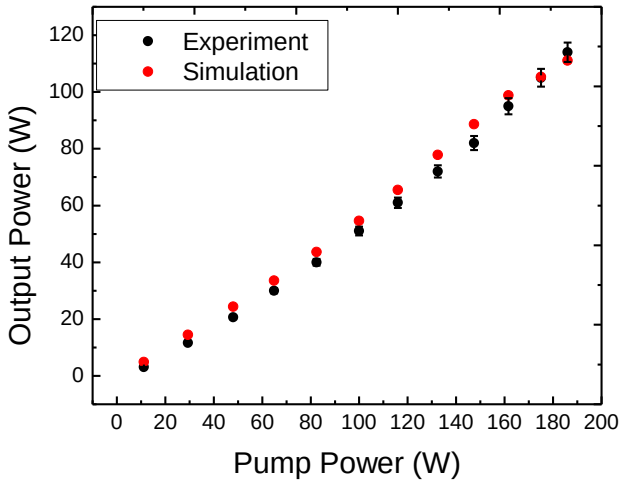

Fig 6.3.1. Comparison of simulation and experimental results.

After this point, we investigated how the system parameters affect the output of the system. Further, we made simulations for various different arrangements. Fig. 6.3.2(a) shows the normal configuration of the system without any changes. The pump light (green curve) is injected from the left-side of the 7.5 m Yb700-25/250DC fiber. Signal propagating in forward direction (black line) is reflected from FBG99. The reflected signal (blue curve) turns back to the beginning of the fiber where it is again reflected by FBG07. As a result, a cavity is formed in between two FBGs. The unreflected 93% from the FBG07 is taken out as the output of the fiber laser. When 170 W of pump power is injected to the fiber, the output is around 114 W. Fig. 6.3.2(b) shows the result when the places of FBG07 and FBG99 are interchanged. As it can be seen, the output power reduced slightly but the optimal fiber length reduced significantly to 5.5 m in this case. Using such a configuration would be beneficial but we did not use it because of the reason stated before.

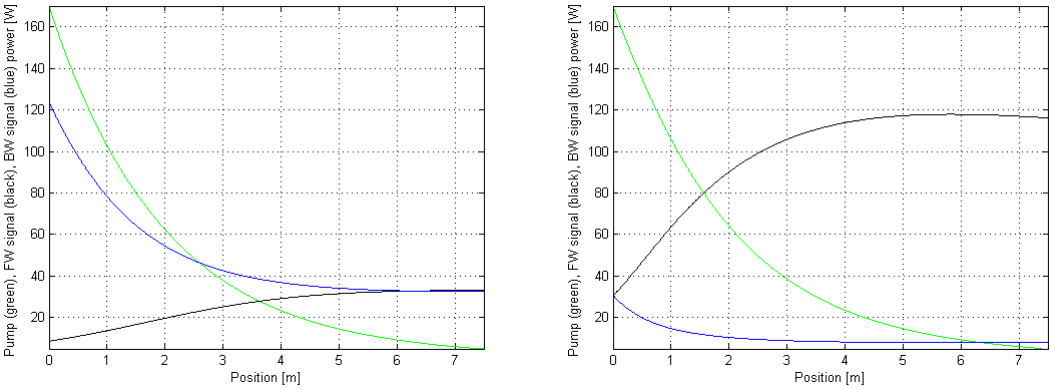

Fig. 6.3.2 The effect of replacing the FBGs with each other; (a) current configuration and (b) interchanged configuration.

Fig. 6.3.3 shows the effects of using 2x shorter and 2x longer fibers instead of the original 7.5 m fiber. In both cases the efficiency drops. For the first case, it is because the pump power was not absorbed efficiently and for the second case it is due to the excessive losses the signal experienced while propagating in a longer fiber.

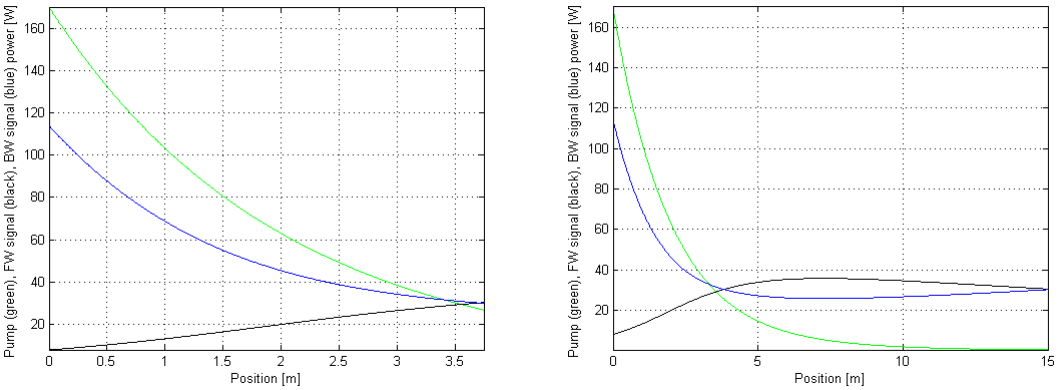

Fig. 6.3.3 The effect of fiber length on the performance; (a) 2x shorter, (b) 2x longer fibers.

We also simulated the effects of changing reflectivity of low-reflective FBG, which is currently 7% percent in the setup. When the reflectivity is dropped to 1%, intracavity energy also drops, which has an adverse effect on pump absorption. When the reflectivity is increased to 50%, the increase in the intracavity energy increases the total loss while dropping the efficiency and output power (Fig 6.3.4).

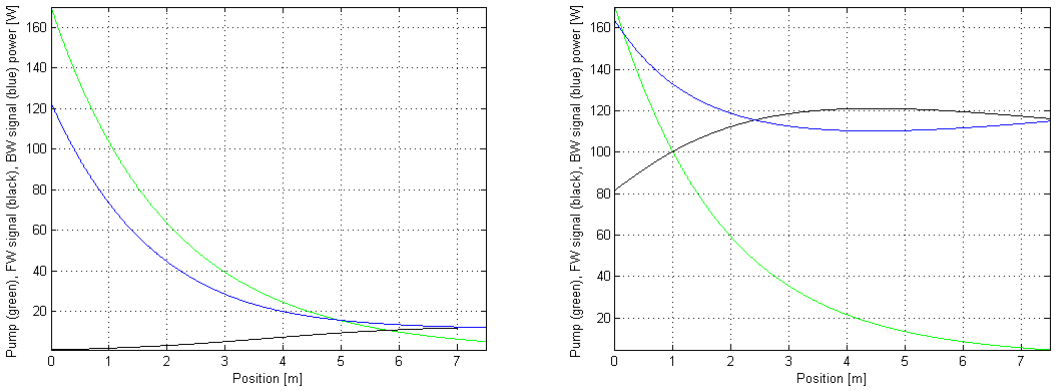

Fig. 6.3.4 The effect reflectivity ratio of the low-reflective FBG; (a) 1% reflectivity, (b) 50% reflectivity.

We compared the effects of using 2x highly doped fiber with using 2x longer fiber. As expected, there is no significant difference (Fig 6.3.5).

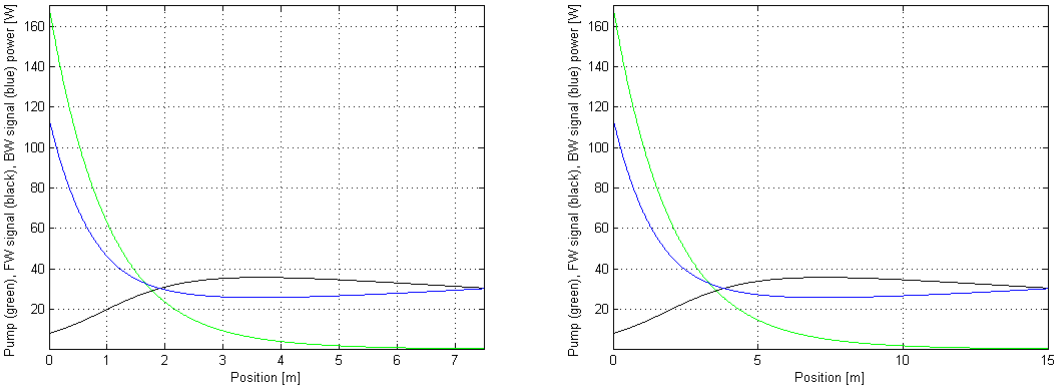

Fig. 6.3.5 Comparison of the effects of (a) using highly doped fiber with (b) using a longer fiber.

Lastly, we simulated the effects of pump parameters on the system and found that the optimal fiber length is independent of pump power, which can be seen in Fig 6.3.6(a). The pumps operating in our setup works around 975 nm coinciding with the absorption peak of Yb-doped fibers. When a wavelength-shifted pump is used, the pump absorption drops as in Fig 6.3.6(b) and the optimum fiber length increases.

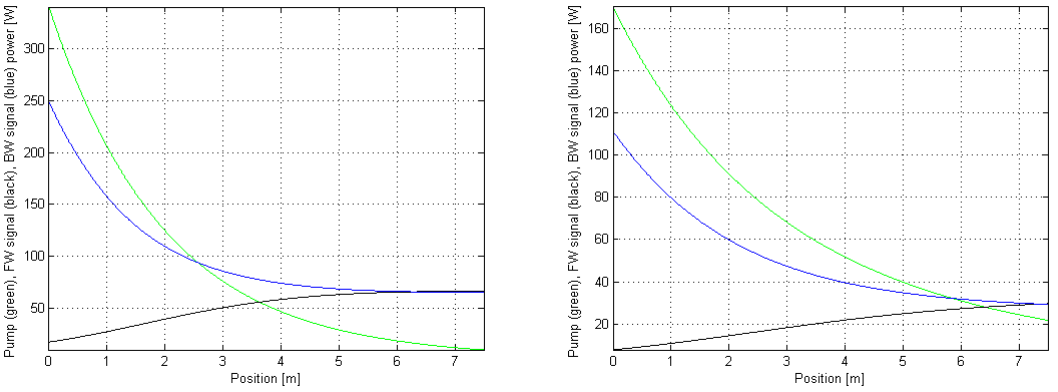

Fig. 6.3.6 The effects of pump parameters; (a) 2x power, (b) 981 nm pump wavelength.

6.4. Conclusion

As a result, we built of an all-fiber CW laser system capable of delivering 114 W of output power at 1060 nm. The power is both limited by the available pump power and the quality of the critical splice. The system was one of the highest power all-fiber laser systems of its time. Beam quality ($M^2 \cong 1.5$) can be improved by coiling the fiber more tightly and increasing the splice quality. We also developed a simulation software, which models the laser as a modified 2-level system. This software is very useful in order to give an idea about the effects of system parameters on the overall efficiency of the system and find the optimized parameters. All-fiber lasers are superior with respect to free-space fiber lasers in terms of flexibility and robustness so we believe that this study is a step towards higher power all-fiber lasers that are expected to find large application areas in industry.

Chapter 7

Comparison of picosecond, nanosecond and long-nanosecond pulses in drilling of various metals

7.1. Introduction

There are numerous industrial material processing applications of high-power lasers. Each of applications requires a different set of optimized laser parameters. As a result, lots of studies have been done for this purpose, however these are generally limited in terms of either variety of the laser parameters or the targets. In this study, we are focusing on micromachining of metal foils by drilling holes through them. These micron-sized holes can be used as ink-jet nozzles, cooling holes on a turbine blade, etc. [43]. We made a systematic comparison of wide range of pulse durations (0.1 ns, 1 ns and 100 ns) by keeping the same pulse peak power with the same average power. We used three different targets (stainless steel, Al, and Cu) in order to differentiate how material properties are affecting the process. In order to obtain a deeper understanding, we also developed a theoretical model incorporating certain simplifying assumptions, while capturing the essence of the underlying physics. We compared the simulation results with the experimental ones giving rise to a reasonable level of agreement within the validity range of our assumptions. In this study, the experimental results are obtained by the author and

Bülent Öktem together, while the theoretical model has been developed entirely by the author.

Cutting, drilling, welding, marking are some examples where fiber lasers are increasingly being used in place of Nd:YAG and CO_2 lasers. For sensitive micromachining applications, relatively low power (<20 W) pulsed lasers are preferred and the target materials have a wide range of spectrum: Metals, alloys (especially steel), silicon and other semiconductors, ceramics, plastics, etc. It is natural to expect the requirement for an optimized parameter set for each specific application. These are usually developed by the users in the field through experience and empirical optimization, with little or no theoretical guidance. Thus, there is need for a systematic study, where a wide range of laser parameters can be investigated for various targets and the dominant physical mechanisms can be identified. To date, indeed, quite a few studies have been reported. Some of the recent ones are the following: In 2008, Ancona *et al.* investigated drilling of steel and copper sheets with 800-fs-long pulses by varying the repetition rate [110]. They found that particle shielding and heat accumulation due to successive pulses may play an important role in the process at high repetition rates and they proposed a simple model for heat accumulation. In 2009, they investigated the effect of pulse duration by using 800 fs, 6 ps and 19 ps long pulses and concluded that the shorter pulses are more efficient and superior in terms of heat accumulation [111]. In 2009, O'Neill and Li demonstrated the importance of the pulse shape for high-quality micromachining of silicon targets where absorptivity is highly temperature dependent [93]. In 2010, Doring *et al.* imaged the hole shape evolution in ultrashort (8 ps) pulse laser drilling of silicon for the first time, *in situ* [112]. They observed that drilling significantly slows down after some threshold depth. Brandi *et al.* investigated the effect of spot-size on drilling efficiency by using 20 ns-long pulses on silicon targets [113]. They concluded that the particle shielding effect is responsible for the decrease in the ablation efficiency for larger spot sizes.

Here, we use three different fiber laser seeds in order to make a systematic study on processing of stainless steel, Al, and Cu targets. The pulse duration of these laser systems are 115 ps, 1 ns and 100 ns with repetition rates of 27 MHz, 3.1 MHz and 31 kHz, respectively. The repetition rates and pulse durations are arranged such that the pulse peak power is the same for same average power. We use these lasers at different power levels to drill holes at different thicknesses of steel, Al, and Cu foils. We develop a simple theoretical model in order to determine how the material removal rate scales with the laser parameters and material properties. We include the convective cooling of the target during heat accumulation due to successive pulses in order to obtain more realistic results. The previous studies were only estimating the initial material removing rate from the surface of a semi-infinite bulk material such as in [110]. Our model handles the drilling process more realistically by predicting a threshold power level after which drilling virtually stops, which is confirmed by the experiments.

7.2. Experimental results

Schematic of the experimental setup can be seen in Fig. 7.2.1. There are three choices for seeding the common amplifier. The first seed is an ordinary ANDi fiber oscillator [25], which is operating at 27 MHz with an output power of 50 mW. Its output is sent to a stretcher fiber in order to increase the pulse duration up to 115 ps. The second seed is another fiber oscillator based on nonlinear optical loop mirror (NOLM) saturable absorber, which directly produces square-like, 1 ns-long pulses at a repetition rate of 3.1 MHz with an output power of 50 mW. The third seed directly produces 100 ns of pulses at 31 kHz repetition rate by modulating a fiber coupled laser diode. Its output power is 150 mW after an internal in-fiber preamplifier. Then, the output of the selected seed is connected to a protective isolator and amplified in a two stage amplifier system. Although the amplifier

system is capable of easily reaching 25 W, maximum power handling capacity of the integrated isolator-collimator limits the output power to 10 W.

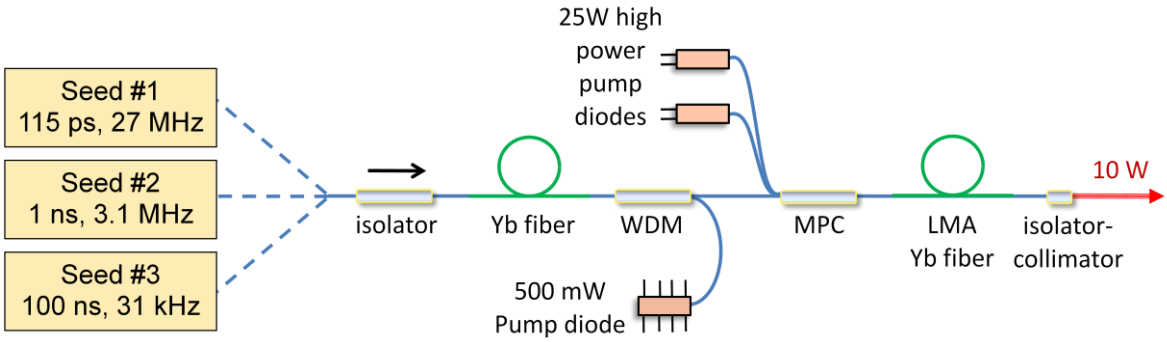

Fig. 7.2.1 Schematic of the oscillator-amplifier setup. WDM: Wavelength-division multiplexer; MPC: Multi pump combiner; LMA: Large mode area.

In order to determine the material removal rate, we focused the laser beam to a spot size of 20 μm on the foil surface. We used a photodetector in order to determine the drilling time of the holes. Since the detector (placed at a suitable location) can also detect a small signal when the laser is turned on, we were able to measure exact time interval for drilling. Fig. 7.2.2 shows the drilling time at different power levels, for different targets and thicknesses. Here, the data points represent the experimental measurement and the lines represent simulation data, which is explained in detail in the next section. Fig 7.2.3 shows the corresponding scanning electron microscope (SEM) images at an average power of 8 W. Note that, the 115-ps system was able to drill only steel foils. If these two figures are examined more carefully, important conclusions can be deduced: (i) Drilling rate increases with decreasing thermal conductivity of the target; (ii) longer pulses are more effective in drilling than the shorter ones; (iii) there is a limiting hole depth after which drilling virtually stops; (iv) crater formation is affected by the exposure time; namely, larger crater

formation is observed for longer exposure times; (v) liquid ejection together with large amount of spall is observed for longer pulses, indicating faster material removal rate.

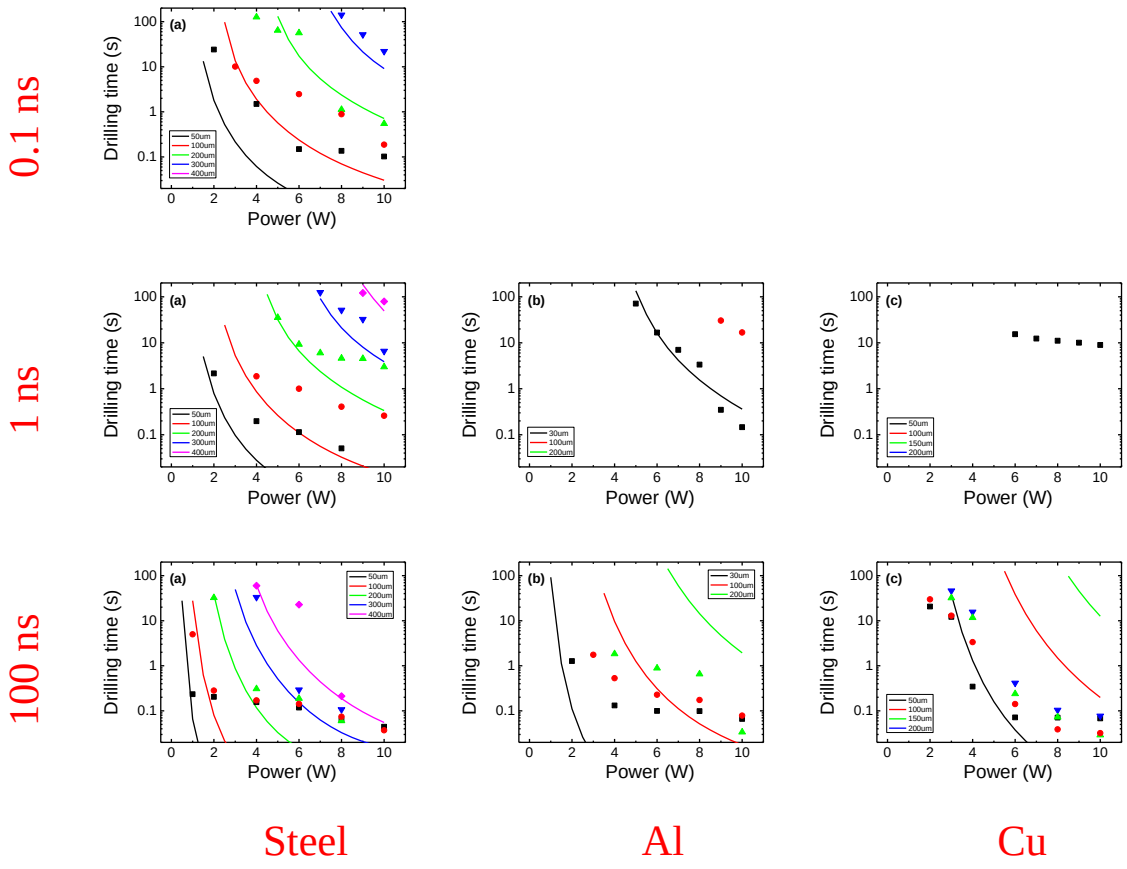

Fig. 7.2.2 Variation of drilling times with respect to laser power and material thickness for (a) steel, (b) Al and (c) Cu targets. Upper, middle and bottom rows are for 115 ps, 1 ns, 100 ns pulse durations, respectively. Points represent experimental results whereas lines represent simulation results.

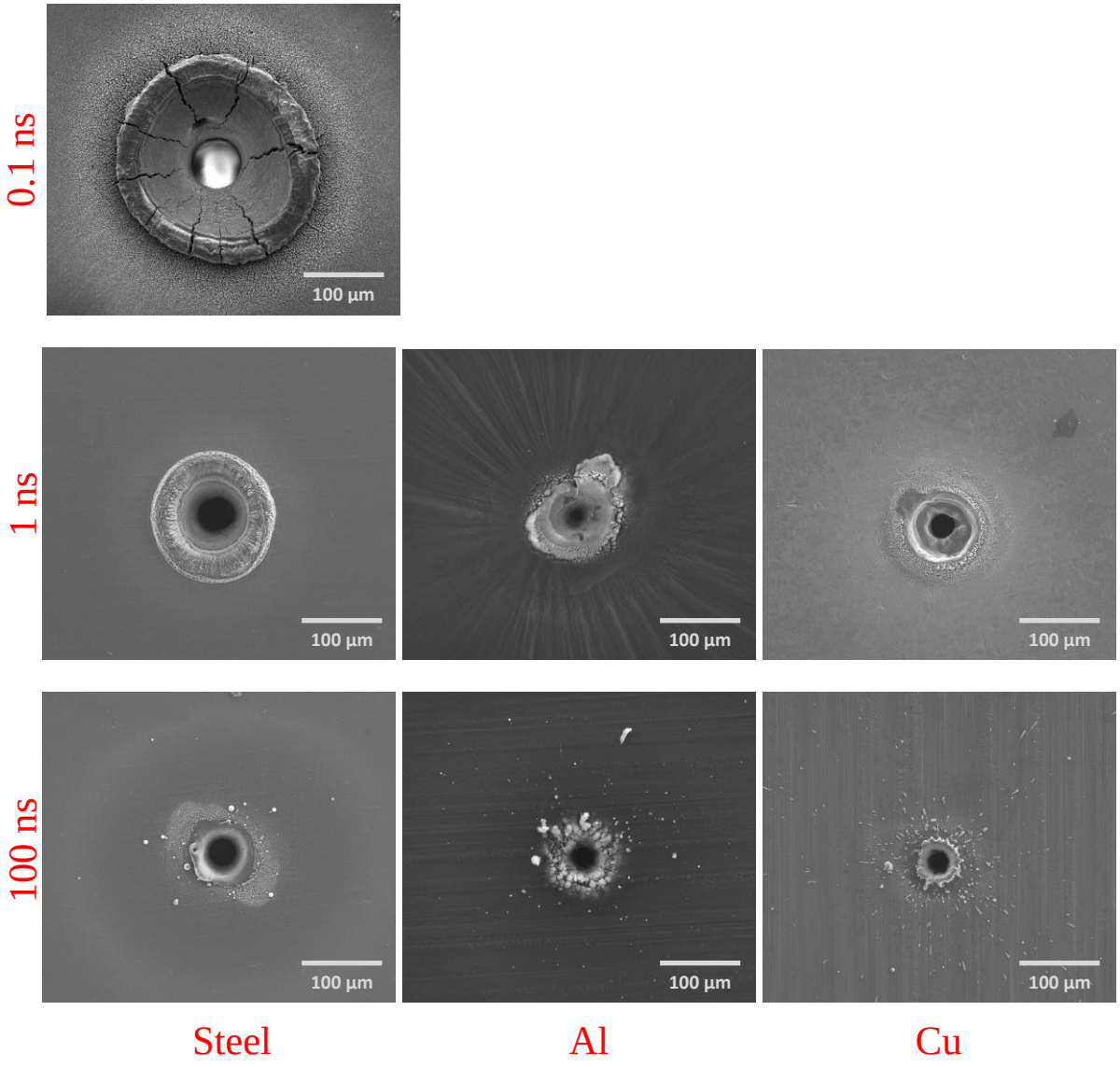

Fig. 7.2.3 SEM images of the holes drilled at 8 W of output power with 115 ps, 1 ns, and 100 ns pulses. Crater formation can be seen for 115 ps pulses due to long exposure times required for drilling. This structure diminishes with increasing pulse duration where drilling rate is higher. However, some liquid ejection occurs this time together with large amount of spall.

7.3. Theoretical Model & Simulations

When light interacts with a surface, the main linear processes that occur are reflection, absorption, and scattering. The reflectivity of most metals is larger than 0.7 at a wavelength of 1 μm. This means that only 30% or less of the incoming light will be able to pass the surface barrier. After this point, light is rapidly absorbed in a metallic medium where the typical penetration depth (also known as skin depth) is around 10 nm. Light interacts with the metals primarily by accelerating the conduction band electrons. Consequently, the kinetic energy of these electrons is converted to heat through collisions, which takes place within few picoseconds. Since all the energy is absorbed within a very thin layer of material, the temperature can rise to very high values, resulting in the formation of a gaseous or even plasma phase. The outer part of this plasma will be ejected as a plume. Ejection speed may be as high as 3000 m/s. This process is completed in 30 ns. However, ejection of cooler and larger particles may continue for up to 1 μs [114]. Meanwhile, diffusion of heat into the bulk of the material takes place. The governing heat transfer equation is

$$\frac{\partial u(\boldsymbol{x},t)}{\partial t} = \alpha \nabla^2 u(\boldsymbol{x},t) + f(\boldsymbol{x},t), \tag{7.3.1}$$

where $u(\boldsymbol{x},t)$ is the temperature rise, $f(\boldsymbol{x},t)$ is the heat generation (source) function, describing the influence of the pulse, and α is thermal diffusivity, which is on the order of 10^{-4} m^2/s. Although it looks like a simple equation, it is a nonlinear (due to the heat source function) partial differential equation and analytical solutions exist for only highly symmetric geometries. However, drilling is actually a very complex process since the surface morphology is continuously changing and there is no exact analytical solution.

Even, solving the heat equation numerically is computationally very demanding. However, certain simplifications can be made, while retaining the essence of the underlying physics: (i) Intensity is homogenously distributed inside the hole. (ii) Temperature distribution is mainly determined by radial heat flow; we ignore any flow in the vertical direction. (iii) Hole radius remains the same throughout the drilling process. (iv) Hole depth is already reached to a significant value where the evaporation is the dominant ablation mechanism. The schematic of our 2D cylindrically symmetric model is shown in Fig. 7.3.1.

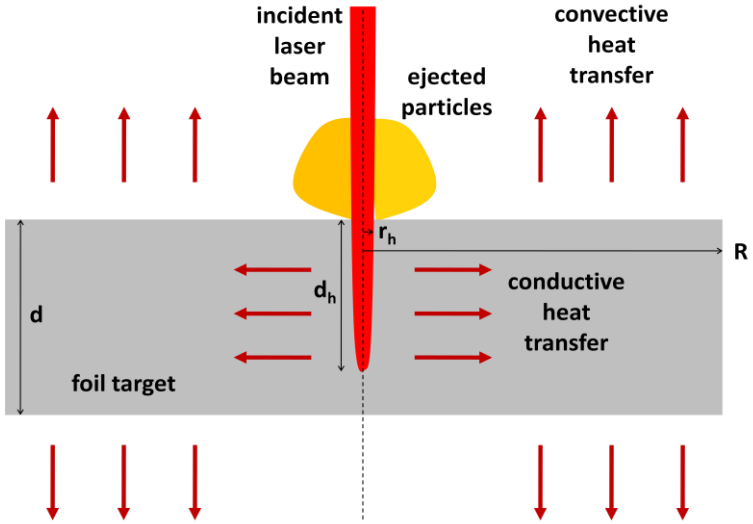

Fig. 7.3.1 Schematic of our laser-matter interaction model.

The heat equation can be most easily solved by using Green's function method that gives a general solution in n-dimensions as

$$u(\boldsymbol{x},t) = \int_0^t \int_{R^n} \phi(\boldsymbol{x}-\boldsymbol{x}', t-t')\, f(\boldsymbol{x}', t') d\boldsymbol{x}' dt', \tag{7.3.2}$$

where $\phi(\boldsymbol{x},t)$ is the fundamental solution given by

$$\phi(\boldsymbol{x},t)=\frac{1}{(4\pi\alpha t)^{n/2}}e^{-\boldsymbol{x}\cdot\boldsymbol{x}/4\alpha t}. \tag{7.3.3}$$

In 2D with cylindrical symmetry this can be written as

$$u(r,t)=\int_0^t\int_0^R\int_{-\pi}^{\pi}\frac{1}{4\pi\alpha(t-t')}e^{-(r^2+r'^2-2rr'\cos\theta)/4\alpha(t-t')}f(r',t')r'd\theta'dr'dt', \tag{7.3.4}$$

which can be simplified by introducing a new time coordinate $t''=t-t'$, and using the approximation of $\cos\theta\cong 1-\theta^2/2$;

$$u(r,t)=\int_0^t\int_0^R\int_{-\pi}^{\pi}\frac{1}{4\pi\alpha t''}e^{-(r-r')^2/4\alpha t''}e^{-rr'\theta^2/4\alpha t''}f(r',t'')r'd\theta'dr'dt''. \tag{7.3.5}$$

If the incident pulse is assumed to be square-shaped in time domain with a constant peak power of P_p, and uniformly distributed throughout the surface of the hole, heat generation function can be written as

$$f(r,t)=\frac{P_p\gamma}{c_p\rho\pi r_h(r_h+2d_h)d_p}f_t(t)=\frac{I_p}{d_p}\frac{\alpha}{k}f_t(t)\,,\quad r_h<r<r_h+d_p\,, \tag{7.3.6}$$

where γ is the ratio of the pulse energy absorbed by the target, c_p is the specific heat, ρ is the density, k is the thermal conductivity, d_p is the penetration depth, d_h is the hole depth, r_h is the hole radius, I_p is the intensity on the surface, and $f_t(t)$ is the time dependence of $f(r,t)$ which can be seen in Fig. 7.3.2.

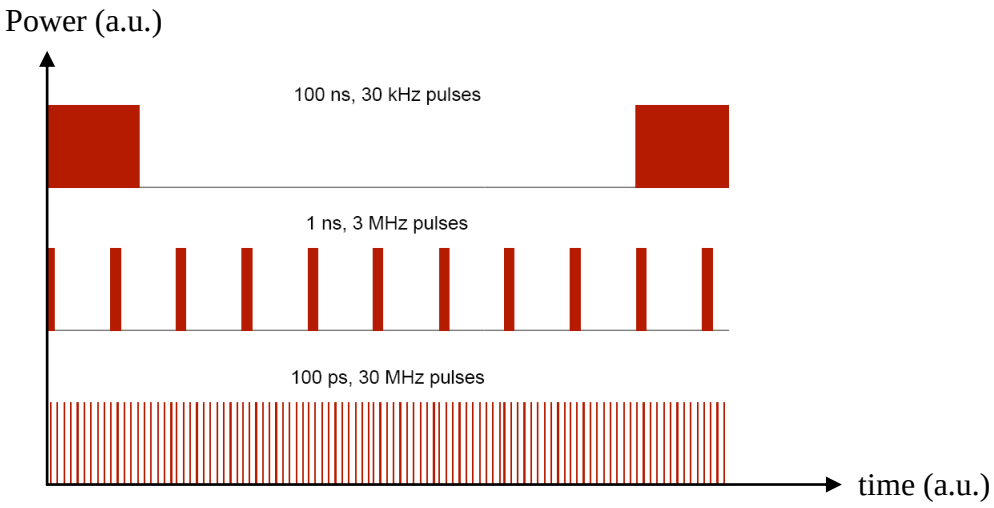

Fig. 7.3.2 Time dependence of $f_t(t)$ for three different seeds. Note that, the peak power of each pulse remains the same for different pulse durations and repetition rates.

In this case, Eq. 7.3.5 becomes

$$u(r,t) = \int_0^t I_p \frac{\alpha}{k} \frac{f_t(t'') r_h e^{-(r-r_h)^2/4\alpha t''}}{4\pi\alpha t''} \int_{-\pi}^{\pi} e^{-r r_h \theta'^2/4\alpha t''} \, d\theta' dt'', \tag{7.3.7}$$

which yields

$$u(r,t) = \int_0^t I_p \frac{\alpha}{\sqrt{\pi} k} \frac{f_t(t'') r_h e^{-(r-r_h)^2/4\alpha t''}}{\sqrt{r r_h}\sqrt{4\alpha t''}} \mathrm{Erf}\left[\frac{\pi\sqrt{r r_h}}{\sqrt{4\alpha t''}}\right] dt'', \tag{7.3.8}$$

where $\mathrm{Erf}[x]$ is the error function. If we calculate the temperature rise at $r = r_h$,

$$u(r_h,t) = \int_0^t I_p \frac{\alpha}{\sqrt{\pi}k} \frac{f_t(t'')}{\sqrt{4\alpha t''}} \mathrm{Erf}\left[\frac{\pi r_h}{\sqrt{4\alpha t''}}\right] dt''. \tag{7.3.9}$$

In numerical simulations, the above integral can be evaluated in two parts; the temperature rise due to the latest pulse with duration t_p can be found by integration as

$$u_1(r_h) = I_p \frac{1}{2\sqrt{\pi}k}\left(\sqrt{4\alpha t_p}\mathrm{Erf}\left[\frac{\pi r_h}{\sqrt{4\alpha t_p}}\right] - \sqrt{\pi} r_h \mathrm{Ei}\left[-\frac{\pi^2 r_h^2}{4\alpha t_p}\right]\right), \tag{7.3.10}$$

where $\mathrm{Ei}[x]$ is the exponential integral function, and the temperature rise due to previous pulses can be calculated as a sum given by

$$u_2(r_h) = \sum_{n=1}^{t/t_r} I_p \frac{\alpha}{\sqrt{\pi}k} \frac{t_p}{\sqrt{4\alpha n t_r}} \mathrm{Erf}\left[\frac{\pi r_h}{\sqrt{4\alpha n t_r}}\right], \tag{7.3.11}$$

where t_r is the repetition period. A convective cooling term should be added to this summation if the time scale is long enough that convection may take place

$$u_2(r_h) = \sum_{n=1}^{t/t_r} I_p \frac{\alpha}{\sqrt{\pi}k} \frac{t_p}{\sqrt{4\alpha n t_r}} \mathrm{Erf}\left[\frac{\pi r_h}{\sqrt{4\alpha n t_r}}\right] e^{-\frac{h n t_r}{c_p \rho d}}. \tag{7.3.12}$$

where h is the convective heat transfer coefficient, which is on the order of 30 W/m^{2}K, and d is the foil thickness. However, we found that this term has negligible effect on the solution for the time scales encountered in this study. By combining the two terms, the temperature after the n^{th} pulse can be found as

$$T(r_h) = u_1(r_h) + u_2(r_h) + T_{amb} \tag{7.3.13}$$

where T_{amb} is the ambient temperature. Since evaporation is assumed to be the main ablation mechanism when the hole depth approaches to its maximum value, we have to calculate the evaporation rate as a function of temperature. For this purpose, we need to find the vapor pressure of the target, which can be calculated from Clausius–Clapeyron relation as

$$P_v = P_{atm} e^{-\frac{\Delta H}{R}\left(\frac{1}{T_e}-\frac{1}{T}\right)}, \tag{7.3.14}$$

where P_{atm} is the atmospheric pressure, R is the gas constant, ΔH is the heat of evaporation and T_e is the evaporation temperature. Lastly, the drilling rate R_d is given in terms of the evaporation rate R_e as

$$R_d = \frac{R_e}{\rho} = \frac{P_v}{\rho}\sqrt{\frac{m}{2\pi k_B T}}, \tag{7.3.15}$$

where m is the atomic mass and k_B is the Boltzmann constant.

We numerically solved this model, which yields the results shown in Fig. 7.2.2 for the corresponding set of parameters. We found that best agreement to experiment is obtained for $\gamma = 1.2$. Given the strong assumptions made here, it is advisable to base one's analysis on the qualitative aspects of these results. In this vein, we observed the following points from the simulations which are in agreement with the experiments: (i) Drilling rate increases with increasing pulse duration and decreasing thermal conductivity. (ii) Required exposure time increases very sharply beyond a certain thickness of material. (iii) The numerical results deviate from the experimental data for large drilling rates, which is an expected behavior because our model is based on evaporative ablation. The parameters (*e.g.* high surface reflectivity) and physical mechanisms (*e.g.* plasma-assisted ablation) are

very different compared to when the hole is shallow. (iv) γ is around unity, which indicates that nearly all of the incident light is absorbed by the target. This is understandable because multiple reflections take place within a deep hole and reflectivity drops for micromachined surfaces.

7.4. Conclusion

In conclusion, we used three fiber lasers with different pulse durations (115 ps, 1 ns, and 100 ns) to drill micron-sized holes in various metal targets (steel, Al, and Cu). In these experiments, we kept the pulse peak power and average power the same by adjusting the repetition rates of the seed lasers. We developed a simple theoretical model in order to explain the experimental observations and obtained good qualitative agreement between the theoretical and experimental results, indicating that the simple model captures essential physics. We found that the longer pulses are better for drilling of foils since they produce higher quality holes with reduced crater formation surrounding them, which may seem contrary to the results reported in Chapter 5. However, this is because of the much longer exposure time required when using shorter pulses. As a result, for drilling applications, we recommend using either long pulses or short pulses with a much larger peak power, while no such restriction exists for micromachining surface structures or texturing. For future work, the theoretical model needs to be improved and can be applied to different nonmetallic materials like semiconductors, particularly silicon. On the experimental side, effort is underway for construction of a fully automated setup to detect the completion of the microdrilling precisely, thus turning of the laser right away and to monitor the plasma formation during the processing.

Chapter 8

Conclusions

Fiber lasers are commonly used, by now, in diverse areas including materials processing, medical, metrology, defense applications, thanks to their inherent advantages over traditional solid state lasers. Their excellent beam quality, power scalability, high efficiency and alignment-free operation are some of those advantages. Consequently, the application areas of fiber lasers are continuously increasing proportional to their maximum output power level, which is increasing at a rate of ~1.7-fold per year for the past decade. For many applications, flexibility and misalignment-free operation is important. In this thesis, we presented our work on high power all-fiber laser designs, which are superior in this respect compared to free-space fiber lasers, after giving a general introduction to the fiber lasers and amplifiers in Chapter 1-2.

In Chapter 3, we demonstrated a 10.6 W (which was later increased to 20 W after further improvements) fiber amplifier, based on strictly in-fiber pump delivery from several multimode diodes via a multimode pump-signal combiner. This was the highest power laser system of its kind. The amplifier was seeded by an all-normal-dispersion (ANDi) fiber laser for the first time and constitutes the first direct confirmation of the feasibility of the

ANDi-type fiber laser for high-power amplification. Extensive numerical simulations explained the observed behavior of the system and closely guided the experimental efforts.

In Chapter 4, we demonstrated that a PM-fiber section inserted into an ANDi laser cavity functions as a Lyot filter and stable mode-locked operation is possible, which was confirmed experimentally and numerically. By this way, we were able to build our first all-fiber Yb-fiber laser. The filter bandwidth and modulation depth were adjustable through the length and splice angle of the PM-fiber section, respectively. We had demonstrated an all-fiber Yb-doped laser cavity without using specialty components such as semiconductor saturable absorbers or chirped fiber Bragg gratings for the first time to our knowledge.

In Chapter 5, we demonstrated a new type of all-fiber Yb laser cavity, which uses a nonlinear optical loop mirror (NOLM) to initiate low-repetition-rate (3.1 MHz) operation with 1-ns-long pulses, eliminating the need for pulse picking. We demonstrated, to our knowledge, the first use of such pulses in micromachining. We also verified using a simple setup that these pulses indeed lack a well-defined chirp and are, therefore, incompressible. The micromachining results indicated that the repeatability and uniformity of the micromachined surfaces are similar for the 1 ns and 0.1 ns lasers and significantly better than those of the 100 ns laser. The amount of ablated material was higher for the 1 ns laser than for the 0.1 ns, but lower than the 100 ns laser.

In Chapter 6, we built of an all-fiber CW laser system capable of delivering 114 W of output power at 1060 nm. The power was both limited by the available pump power and the quality of the splices. The system was one of the highest power all-fiber laser systems of its time. We also developed a simulation software, which models the laser as a modified two-level system. This software is was very useful in optimizing the system parameters.

In Chapter 7, we used three fiber lasers with different pulse durations (115 ps, 1 ns, and 100 ns) to drill micron-sized holes in various metal targets (steel, Al, and Cu). In these experiments, we kept the pulse peak power and average power the same by adjusting the repetition rates of the seed lasers. We developed a simple theoretical model in order to explain the experimental observations and obtained good qualitative agreement between the theoretical and experimental results, indicating that the simple model captures essential physics. We recommended using either long pulses or short pulses with a much larger peak power for drilling applications, while no such restriction exists for micromachining surface structures or texturing.

As a summary, there is no reason to think that the rise of fiber lasers will cease in following few decades. The high power application areas of the fiber lasers will continue to increase by their output powers and the all-fiber designs will be preferred where robustness and misalignment-free operation are of primary importance. In future, the following areas will be critical:

- The continuous increase of output power level requires better nonlinearity and thermal management. Different kind of fiber designs should be developed for this purpose without deteriorating the beam quality.

- Higher environmental stability is needed for the industrial use. This kind of oscillators can be realized by using PM components or active polarization controlling.

- Splice quality is of primary importance so any improvements in this area will be appreciated.

- Amplifier systems at other wavelengths will be important such as Tm fiber lasers operating at eye-safe 2 μm where the atmospheric transmission is also higher.

Bibliography

[1] J. L. Baird, British Patent 285,738 (1928).

[2] C. W. Hansell, U. S. Patent 1,751,584 (1930).

[3] H. Lamm, "Biegsame optische gerate," Z. Instrumenten. 50, 579 (1930).

[4] A. C. S. van Heel, "A new method of transporting optical images without aberrations," Nature 173, 39 (1954).

[5] H. H. Hopkins and N. S. Kapany, "A flexible fiberscope using static scanning," Nature 173, 39 (1954).

[6] B. O'Brian, U. S. Patent 2,825,260 (1958).

[7] B. I. Hirschowitz, U. S. Patent 3,010,357 (1961).

[8] T. Miya, Y. Terunuma, T. Hosaka, and T. Miyashita, "Ultimate low-loss single-mode fibre at 1.55 μm," Electron. Lett. 15, 106 (1979).

[9] http://www.fiberoptics4sale.com/wordpress/optical-fiber-attenuation

[10] R. H. Stolen, E. P. Ippen, and A. R. Tynes, "Raman oscillation in glass optical waveguide," Appl. Phys. Lett. 20, 62 (1972).

[11] E. P. Ippen and R. H. Stolen, "Stimulated Brillouin scattering in optical fibers," Appl. Phys. Lett. 21, 539 (1972).

[12] R. G. Smith, "Optical power handling capacity of low loss optical fibers as determined by stimulated Raman and Brillouin scattering," Appl. Opt. 11, 2489 (1972).

[13] R. H. Stolen and A. Ashkin, "Optical Kerr effect in glass waveguide," Appl. Phys. Lett. 22, 294 (1973).

[14] R. H. Stolen, J. E. Bjorkholm, and A. Ashkin, "Phase-matched three-wave mixing in silica fiber optical waveguides," Appl. Phys. Lett. 24, 308 (1974).

[15] K. O. Hill, D. C. Johnson, B. S. Kawasaki, and R. I. MacDonald, “CW three-wave mixing in single-mode fibers,” J. Appl. Phys. 49, 5098 (1974).

[16] R. H. Stolen, “Phase-matched-stimulated four-photon mixing in silica-fiber waveguides,” IEEE J. Quantum Electron. QE-11, 100 (1975).

[17] R. H. Stolen and C. Lin, “Self-phase-modulation in silica optical fibers,” Phys. Rev. A 17, 1448 (1978).

[18] A. Hasegawa and F. Tappert, “Transmission of stationary nonlinear optical pulses in dispersive dielectric fibers. I. Anomalous dispersion,” Appl. Phys. Lett. 23, 142 (1973).

[19] L. F. Mollenauer, R. H. Stolen, and J. P. Gordon, “Experimental observation of picosecond pulse narrowing and solitons in optical fibers,” Phys. Rev. Lett. 45, 1095 (1980).

[20] I. N. Duling III, “Subpicosecond all-fibre erbium laser,” Electron. Lett. 27, 544-545 (1991).

[21] K. Tamura, C. R. Doerr, H. A. Haus, and E. P. Ippen, “Soliton fiber ring laser stabilization and tuning with a broad intracavity filter,” IEEE Phot. Tech. Lett. 6, 697-699 (1994).

[22] K. Tamura, E. P. Ippen, H. A. Haus, and L. E. Nelson, “77-fs pulse generation from a stretched-pulse mode-locked all-fiber ring laser,” Opt. Lett. 18, 1080-1082 (1993).

[23] F. Ö. Ilday, J. R. Buckley, W. G. Clark, and F. W. Wise, “Self-similar evolution of parabolic pulses in a laser,” Phys. Rev. Lett. 92, 3902-3905 (2004).

[24] J. R. Buckley, F. Ö. Ilday, F. W. Wise, “Femtosecond fiber lasers with pulse energies above 10 nJ,” Opt. Lett. 30, 1888-1890 (2005).

[25] A Chong, J Buckley, W Renninger, F Wise, “All-normal-dispersion femtosecond fiber laser,” Opt. Exp. 14, 10095-10100 (2006).

[26] B. Oktem, C. Ülgüdür and F. Ö. Ilday, "Soliton-similariton fibre laser", Nature Photonics, 4, 307, (2010).

[27] E. Snitzer, H. Po, F. Hakimi, R. Tumminelli, B. C. McCollum, “Double clad offset core Nd fiber laser”, Optical Fiber Sensors Topical Meeting, New Orleans, Louisiana/USA, paper PD 5, (1988).

[28] http://www.ipgphotonics.com/

[29] http://www.rp-photonics.com/encyclopedia.html

[30] http://www.nlight.fi/techoverview_dnd.php

[31] G. P. Agrawal, Nonlinear Fiber Optics (Academic Press, 2007).

[32] R. W. Boyd, Nonlinear Optics (Academic Press, 2003).

[33] P. W. Milonni and J. H. Eberly, Lasers (Wiley Interscience, 1988).

[34] H. A. Haus, E. P. Ippen, and J. G. Fujimoto, “Structures for additive pulse mode locking,” J. Opt. Soc. Am. B 8, 2068-2078 (1991).

[35] Andreas Tünnermann, Thomas Schreiber, and Jens Limpert, "Fiber lasers and amplifiers: an ultrafast performance evolution," Appl. Opt. 49, F71-F78 (2010).

[36] http://www.photonics.com/Article.aspx?AID=34668

[37] http://fgmdb.kakuda.jaxa.jp

[38] J.P.Koplow, D.A.V.Kliner, and L.Goldberg, “Single-mode operation of a coiled multimode fiber amplifier”, Optics Letters, 25, pp.442, (2000).

[39] C.C.Renaud, R.J.Selvas-Aguilar, J.Nilsson, P.W.Turner, and A.B.Grudinin, “Compact high-energy Q-switched cladding-pumped fiber laser with a tuning range over 40nm”, IEEE Photonics Technology Letters, 11(8), pp.976-978, (1999).

[40] H.L.Offerhaus, N.G.Broderick, D.J.Richardson, R.Sammut, J.Caplen, and L.Dong, “High energy single-transverse mode Q-switched fiber laser based on a multimode large-mode area erbium-doped fiber”, Optics Letters, 23 (21), pp.1683-1685, (1998).

[41] C.-H. Liu, G. Chang, N. Litchinitser, A. Galvanauskas, D. Guertin, N. Jabobson, and K. Tankala, “Effectively single-mode chirally-coupled core fiber,” in Advanced

Solid-State Photonics, OSA Technical Digest Series (CD) (Optical Society of America, 2007), paper ME2.

[42] http://www.itflabs.com/

[43] W. M. Steen, J. Mazumder, Laser Material Processing, 4th Ed. (Springer, 2010).

[44] C. K. N. Patel, "Continuous wave laser action on vibrational-rotational transitions of CO_2," Phys. Rev. A 136, 1187 (1964).

[45] J.E. Geusic, H.M. Marcos, and L.G. Van Uitert, "Laser oscillation in Nd-Doped yttrium aluminum, yttrium gallium and gadolinium garnets," Appl. Phys. Lett. 4, 182 (1964).

[46] H. Kroemer, "A proposed class of heterojunction injection lasers," Proc. IEEE, 51, 1782 (1963).

[47] J. J. Ewing, C. A. Brau, "Laser action on the bands of KrF and XeCI," Appl. Phys. Lett. 27, 350 (1975).

[48] P. F. Moulton, "Spectroscopic and laser characteristics of Ti:Al2O3", J. Opt. Soc. Am. B 3 (1), 125 (1986).

[49] J. F. Ready, D. F. Farson, LIA Handbook of Laser Materials Processing, (Laser Institute of America, Magnolia Publishing, Inc., 2001).

[50] K. Sugioka, M. Meunier, A. Pique, Laser Precision Microfabrication, (Springer 2010).

[51] Malcolm Charles Gower, "Industrial applications of laser micromachining," Opt. Express 7, 56-67 (2000).

[52] S. Nolte, C. Momma, H. Jacobs, A. Tünnermann, B. N. Chichkov, B. Wellegehausen, and H. Welling, "Ablation of metals by ultrashort laser pulses," J. Opt. Soc. Am. B 14, 2716-2722 (1997).

[53] R. Schmit, K. Wundt, "Fundamentals of laser drilling," European PCB Convention (1998).

[54] P. K. Mukhopadhyay, K. Ozgoren, I. Budunoglu, and F. Ilday, "All-fiber low-noise high-power femtosecond Yb-fiber amplifier system seeded by an all-normal dispersion fiber oscillator," IEEE J. Sel. Top. Quantum Electron. 15(1), 145–152 (2009).

[55] S. Nolte, "Micromachining," in Ultrafast Lasers, M. E. Fermann, A. Galvanauskas, and G. Sucha (Eds.), New York: Marcel Dekker, (2003), pp. 359–394.

[56] E. G. Gamaly, A. V. Rode, and B. Luther-Davies, "Ultrafast laser ablation and film deposition," in Pulsed Laser Deposition of Thin Films, R. Eason, Ed. Hoboken, NJ: Wiley, (2007), pp. 99–130.

[57] W. Denk, J. H. Strickler, and W. W. Webb, "Two-photon laser scanning fluorescence microscopy," Science, vol. 248, pp. 73–76, (1990).

[58] H. Lubatschowksi and A. Heisterkamp, "Interaction with biological tissue," in Femtosecond Technology for Technical and Medical Applications, F. Dausinger, F. Lichtner, and H. Lubatschowki, Eds. Heidelberg, Germany: Springer-Verlag, (2004), pp. 91–104.

[59] A. Vogel, J. Noack, G. Hutman, and G. Paltauf, "Mechanisms of femtosecond laser nanosurgery of cells and tissues," Appl. Phys. B, vol. 81, pp. 1015–1047, (2005).

[60] M. E. Fermann, V. I. Kruglov, B. C. Thomsen, J. M. Dudley, and J. D. Harvey, "Self-similar propagation and amplification of parabolic pulses in optical fibers," Phys. Rev. Lett., vol. 84, pp. 6010–6013, (2004).

[61] J. Limpert, T. Schreiber, T. Clausnitzer, K. Zollner, H.-J. Fuchs, E.-B. Kley, H. Zellmer, and A. Tünnermann, "High-power femtosecond Yb-doped fiber amplifier," Opt. Express, vol. 10, pp. 628–638, (2002).

[62] D. Strickland and G. Mourou, "Compression of amplified chirped optical pulses," Opt. Commun., vol. 56, pp. 219–221, (1985).

[63] N. G. R. Broderick, H. L. Offerhaus, D. J. Richardson, and R. A. Sammut, “Power scaling in a passively mode-locked large-mode area fiber laser,” IEEE Photon. Technol. Lett., vol. 10, no. 12, pp. 1718–1720, Dec. (1998).

[64] J. Limpert, T. Clausnitzer, A. Liem, T. Schreiber, H. J. Fuchs, H. Zellmer, E. B. Kley, and A. Tünnermann, “High-average-power femtosecond fiber chirped-pulse amplification system,” Opt. Lett., vol. 28, pp. 1984–1986, (2003).

[65] F. Röser, J. Rothhard, B. Ortac, A. Liem, O. Schmidt, T. Schreiber, J. Limpert, and A. Tünnermann, “131 W 220 fs fiber laser system,” Opt. Lett., vol. 30, pp. 2754–2756, (2005).

[66] F. Röser, T. Eidam, J. Rothhardt, O. Schmidt, D. N. Schimpf, J. Limpert, and A. Tünnermann, “Millijoule pulse energy high repetition rate femtosecond fiber chirped-pulse amplification system,” Opt. Lett., vol. 32, pp. 3495–3497, (2007).

[67] T. R. Schibli, I. Hartl, D. C. Yost, M. J. Martin, A. Marcinkevicius, M. E. Fermann, and J. Ye, “Optical frequency comb with submillihertz linewidth and more than 10 W average power,” Nat. Photon., vol. 2, pp. 55–59, (2008).

[68] F. O. Ilday, H. Lim, J. R. Buckley, and F. W. Wise, “Practical all-fiber source of high-power, 120 fs pulses at 1 μm,” Opt. Lett., vol. 28, pp. 1362–1364, (2003).

[69] F. Gonthier, L.Martineau, N.Azami, M. Faucher, F. Seguin, D. Stryckman, and A. Villeneuve, “High power all-fiber components: the missing link for high-power fiber lasers” Proc. SPIE, vol. 5335, pp. 266–276, (2004).

[70] A. Chong, W. Renninger, and F. W. Wise, “All-normal-dispersion femtosecond fiber laser with pulse energy above 20 nJ,” Opt. Lett., vol. 32, pp. 2408–2410, (2007).

[71] J. An, D. Kim, J. W. Dawson, M. J. Messerly, and C. P. Barty, “Gratingless, fiber-based oscillator that generates 25 nJ pulses at 80 MHz, compressible to 150 fs,” Opt. Lett., vol. 32, pp. 2010–2012, (2007).

[72] H. Lim, J. R. Buckley, and F. W. Wise, “Wavelength tunability of femtosecond Yb fiber lasers,” in Proc. Conf. Lasers Electro-Opt. (CLEO 2004), May 16–21, vol. 2, pp. 2–3.

[73] L. Kuznetsova, F. W. Wise, S. Kane, and J. Squier, “Chirped-pulse amplification near the gain-narrowing limit of Yb-doped fiber using a reflection grism compressor,” Appl. Phys. B, vol. 88, no. 4, pp. 515–518, (2007).

[74] A. E. Siegman and S.W. Townsend, “Output beam propagation and beam quality from a multimode stable-cavity laser,” IEEE J. Quantum Electron., vol. 29, no. 4, pp. 1212–1217, Apr. (1993).

[75] F. O. Ilday, J. Chen, A. Winter, F. X. Kartner, F. W. Wise, O. Shkurikhin, and D. Gapontsev, “Low-noise, high-energy, single-mode, femtosecond fiber laser system,” in Proc. Conf. Lasers Electro-Opt. (CLEO 2005), vol. 2, pp. 825–827.

[76] R. P. Scott, C. Langrock, and B. H. Kolner, “High-dynamic-range laser amplitude and phase noise measurement techniques,” IEEE J. Quantum Electron., vol. 7, no. 4, pp. 641–655, Jul./Aug. (2001).

[77] M. Tröbs, P.Wessels, and C. Fallnich, “Power- and frequency-noise characteristics of an Yb-doped fiber amplifier and actuators for stabilization,” Opt. Express, vol. 13, pp. 2224–2235, (2005).

[78] S. Zhou, L. Kuznetsova, A. Chong, and F. W. Wise, “Compensation of nonlinear phase shifts with third-order dispersion in short-pulse fiber amplifiers,” Opt. Express, vol. 13, pp. 4869–4877, (2005).

[79] L. Shah, Z. Liu, I. Hartl, G. Imeshev, G. C. Cho, and M. E. Fermann, “High energy femtosecond Yb cubicon fiber amplifier,” Opt. Express, vol. 13, pp. 4717–4722, (2005).

[80] K. Özgören and F. Ö. Ilday, "All-fiber all-normal dispersion laser with a fiber-based Lyot filter," Opt. Lett. 35, 1296-1298 (2010).

[81] F. W. Wise, A. Chong, and W. H. Renninger, "High-energy femtosecond fiber lasers based on pulse propagation at normal dispersion," Laser Photonics Rev. 2, 58 (2008).

[82] W. H. Renninger, A. Chong, and F. W. Wise, "Dissipative solitons in normal-dispersion fiber lasers," Phys. Rev. A 77, 023814 (2008).

[83] O. Prochnow, A. Ruehl, M. Schultz, D. Wandt, and D. Kracht, "All-fiber similariton laser at 1 μm without dispersion compensation," Opt. Express 15, 6889 (2007).

[84] C. K. Nielsen and S. R. Keiding, "All-fiber mode-locked fiber laser," Opt. Lett. 32, 1474 (2007).

[85] K. Kieu and F. W. Wise, "All-fiber normal-dispersion femtosecond laser," Opt. Express 16, 11453 (2008).

[86] M. Schultz, H. Karow, O. Prochnow, D. Wandt, U. Morgner, and D. Kracht, "All-fiber ytterbium femtosecond laser without dispersion compensation," Opt. Express 16, 19562 (2008).

[87] J. Fekete, A. Cserteg and R. Szipocs, "All-fiber, all-normal dispersion ytterbium ring oscillator," Laser Phys. Lett. 6, 49 (2009).

[88] B. Lyot, "Un monochromateur a grand champ utilisant les interferences en lumiere polarisee," C. R. Acad. Sci. III 197, pp. 1593 (1933).

[89] M. Hofer, M. E. Fermann, F. Harberl, M. H. Ober, and A. J. Schmidt, "Mode locking with cross-phase and self-phase modulation," Opt. Lett. 16, 502 (1991).

[90] G. Shabtay, E. Eidinger, Z. Zalevsky, D. Mendlovic and E. Marom, "Tunable birefringent filters - optimal iterative design," Opt. Express 10, 1534 (2002).

[91] H. Lim, F. Ö. Ilday, and F. W. Wise, "Femtosecond ytterbium fiber laser with photonic crystal fiber for dispersion control," Opt. Express 10, 1497 (2002).

[92] Kivanç Özgören, Bülent Öktem, Sinem Yilmaz, F. Ömer Ilday, and Koray Eken, "83 W, 3.1 MHz, square-shaped, 1 ns-pulsed all-fiber-integrated laser for micromachining," Opt. Express 19, 17647-17652 (2011).

[93] W. O'Neill, and K. Li, "High-quality micromachining of silicon at 1064 nm using a high-brightness MOPA-based 20-W Yb fiber laser," IEEE J. Sel. Top. Quant. 15, 462-470 (2009).

[94] M. Erdogan, B. Öktem, H. Kalaycioglu, S. Yavas, P. Mukhopadhyay, K. Eken, K. Özgören, Y. Aykac, U. H. Tazebay, and F. Ö. Ilday, "Texturing of titanium (Ti6AI4V) medical implant surfaces with MHz-repetition-rate femtosecond and picosecond Yb-doped fiber lasers," Opt. Express 19, 10986 (2011).

[95] M. Murakami, B. Liu, Z. Hu, Z. Liu, Y. Uehara, and Y. Che, "Burst-mode femtosecond pulsed laser deposition for control of thin film morphology and material ablation," Appl. Phys. Expr. 2, 042501 (2009).

[96] H. A. Haus, "Mode-locking of lasers," IEEE J. Sel. Top. Quantum Electron. 6, 1173 (2000).

[97] V. J. Matsas, T. P. Newson, M. N. Zervas, "Self-starting passively mode-locked fibre ring laser exploiting nonlinear polarization switching," Opt. Commun. 92, 61-66 (1992).

[98] M. Horowitz, Y. Barad, and Y. Silberberg, "Noiselike pulses with a broadband spectrum generated from an erbium-doped fiber laser," Opt. Lett. 22, 799-801 (1997).

[99] D. Y. Tang, L. M. Zhao, L. M. Zhao, "Soliton collapse and bunched noise-like pulse generation in a passively mode-locked fiber ring laser," Opt. Express 13, 2289-2294 (2005).

[100] L. M. Zhao, D. Y. Tang, J. Wu, X. Q. Fu, and S. C. Wen, "Noise-like pulse in a gain-guided soliton fiber laser," Opt. Express 15, 2145-2150 (2007).

[101] L. M. Zhao, D. Y. Tang, T. H. Cheng, and C. Lu, "Nanosecond square pulse generation in fiber lasers with normal dispersion," Opt. Comm. 272, 431 (2007).

[102] N. J. Doran and David Wood, "Nonlinear-optical loop mirror," Opt. Lett. 13, 56 (1988).

[103] I. L. Budunoğlu, C. Ülgüdür, B. Oktem, and F. Ö. Ilday, "Intensity noise of mode-locked fiber lasers," Opt. Lett. 34, 2516-2518 (2009).

[104] E. J. R. Kelleher, J. C. Travers, E. P. Ippen, Z. Sun, A. C. Ferrari, S. V. Popov, and J. R. Taylor, "Generation and direct measurement of giant chirp in a passively mode-locked laser," Opt. Lett. 34, 3526-3528 (2009).

[105] Y. Jeong, J. Sahu, D. Payne, and J. Nilsson, "Ytterbium-doped large-core fiber laser with 1.36 kW continuous-wave output power," Opt. Express 12, 6088-6092 (2004).

[106] Yoon-Chan Jeong, Alexander J. Boyland, Jayanta K. Sahu, Seung-Hwan Chung, Johan Nilsson, and David N. Payne, "Multi-kilowatt single-mode ytterbium-doped large-core fiber laser," J. Opt. Soc. Korea 13, 416-422 (2009).

[107] Shupeng Yin, Ping Yan, and Mali Gong, "End-pumped 300 W continuous-wave ytterbium-doped all-fiber laser with master oscillator multi-stage power amplifiers configuration," Opt. Express 16, 17864-17869 (2008).

[108] Baoyin Zhao, Kailang Duan, Wei Zhao, Cheng Li, and Yishan Wang, "Experimental study on high power all-fiber laser," Chin. Opt. Lett. 8, 404-406 (2010).

[109] http://www.nlight.net/

[110] A. Ancona, F. Roser, K. Rademaker, J. Limpert, S. Nolte, and A. Tünnermann, "High speed laser drilling of metals using a high repetition rate, high average power ultrafast fiber CPA system," Opt. Express 16, 8958-8968 (2008).

[111] A. Ancona, S. Doring, C. Jauregui, F. Roser, J. Limpert, S. Nolte, and A. Tünnermann, "Femtosecond and picosecond laser drilling of metals at high repetition rates and average powers," Opt. Lett. 34, 3304-3306 (2009).

[112] Sven Doring, Soren Richter, Stefan Nolte, and Andreas Tünnermann, “In situ imaging of hole shape evolution in ultrashort pulse laser drilling,” Opt. Express 18, 20395-20400 (2010).

[113] Fernando Brandi, Nicolas Burdet, Riccardo Carzino, and Alberto Diaspro, "Very large spot size effect in nanosecond laser drilling efficiency of silicon," Opt. Express 18, 23488-23494 (2010).

[114] J. Konig, S. Nolte, and A. Tünnermann, “Plasma evolution during metal ablation with ultrashort laser pulses,” Opt. Express 13, 10597-10607 (2005).